Error Controlled hp-Adaptive Finite Element Methods for the Time-Dependent Maxwell Equations

PhD Thesis
Martin Lilienthal, 2015

TECHNISCHE
UNIVERSITÄT
DARMSTADT

GRADUATE SCHOOL
computational engineering

Technische Universität Darmstadt, 2015

To my lovely wife Nathalie

Error Controlled *hp*-Adaptive Finite Element Methods for the Time-Dependent Maxwell Equations

Vom Fachbereich Elektrotechnik und Informationstechnik
der Technischen Universität Darmstadt
zur Erlangung des akademischen Grades eines Doktor-Ingenieurs (Dr.-Ing.)
genehmigte Dissertation

von
Martin Lilienthal, M.Sc.
Geboren am 6.8.1982 in Frankfurt am Main

Referent:	Prof. Dr.-Ing. Thomas Weiland
Korreferent:	Prof. Dr. techn. Herbert Egger

Tag der Einreichung:	11.11.2014
Tag der mündlichen Prüfung:	6.3.2015

D17
Darmstadt 2015

Erklärung nach §9 PromO
Ich versichere hiermit, dass ich die vorliegende Dissertation allein und nur unter Verwendung der angegebenen Literatur verfasst habe. Diese Arbeit hat bisher noch nicht zu Prüfungszwecken gedient.

Darmstadt, den 11. November 2014

Contents

Abstract

This thesis deals with the development and analysis of a discretization method and the error controlled adaptation of spatial and temporal discretizations in context of the time-dependent Maxwell equations.

To this end, a *hp* space-time Galerkin discretization for Maxwell's equations, allowing for local adaptation of the polynomial approximation order p as well as the local meshsize h, is developed and analyzed. Furthermore, the developed discretization is extended to problems with waveguide structure, in order to efficiently model waveguide ports.

For the purpose of local adaptation and control of the global discretization error, *a posteriori* error estimates for quantities of interest such as scattering parameters or farfield quantities are derived and employed within an *hp*-adaptive algorithm. While such adjoint based *a posteriori* error estimates are available for many other problems, its application to the present problem has been newly developed in this thesis.

Kurzfassung

Die vorliegende Arbeit beschäftigt sich mit der Entwicklung und Analyse einer Diskretisierungsmethode sowie der adaptiven Kontrolle der räumlichen und zeitlichen Diskretisierungsfehler im Rahmen der zeitabhängigen Maxwellgleichungen.

Dazu wird eine *hp*-Galerkin Diskretisierungsmethode, welche die lokale Adaption des Grades der approximierenden Polynome p sowie der Gitterschrittweite h in Raum und Zeit ermöglicht, entwickelt und analysiert. Weiterhin wird die entwickelte Methode mittels speziell angepasster Basisfunktionen dahingehend erweitert, dass Wellenleiterprobleme effizient und genau gelöst werden können.

Mit dem Ziel der Kontrolle des globalen Diskretisierungsfehlers, werden *a posteriori* Fehlerschätzer für von der Lösung der Maxwellgleichungen abgeleitete Größen wie z.B. Streuparameter oder Fernfelder hergeleitet und innerhalb eines Raum-Zeit *hp*-adaptiven Algorithmus angewendet. Während solche auf der Fehlerdarstellung über das adjungierte Problem basierende Fehlerschätzer bereits für viele andere Gleichungen publiziert wurden, wurde die Anwendung dieser Methode der *a posteriori* Fehlerschätzung auf die zeitabhängigen Maxwellgleichungen im Rahmen der vorliegenden Arbeit entwickelt und implementiert.

1 Introduction

1.1 Motivation

The accurate and efficient solution of Maxwell's equations plays an important role in applications like broadband scattering, antenna design, or the development of particle accelerator components. In many of these applications, one is not interested in the solution primarily itself, but in certain quantities derived from the solution. Typical quantities of interest (QOIs), arising for example in antenna design, are farfield characteristics or scattering parameters. Given the importance of such quantities, it is desirable to know and control the error in such QOIs, which is inevitably introduced, when numerical methods are applied for solving the underlying Maxwell's equations. Furthermore, it is of importance to obtain the QOI with the least possible effort in terms of computational costs.

This leads directly to the topic of goal-oriented error control within adaptive numerical methods (see in particular the survey papers [8, 19]). The goal is to refine the discretization locally, such that at termination of the adaptive process the QOI is approximated within a given error-tolerance. In this context, it is desirable to employ discretization methods, which are not only high-order accurate, but also offer high flexibility in terms of local refinement. Possible choices are finite-difference [67, 69], finite-volume [38], and finite-element methods (FEMs) [18, 27, 52, 53]. Both requirements can be achieved in a natural way for FEMs. Since the solution is approximated locally by polynomials, the discretization can be refined not only by reducing the local mesh size h, but also by locally raising the degree of the approximating polynomials.

While h-refinement allows for algebraic rates of convergence with respect to the number of degrees of freedom (DOFs) in the discretization, p-refinement allows for obtaining exponential rates of convergence in case of smooth solutions. The combination of both types of refinement within an adaptive discretization leads to hp-adaptive finite element methods [4, 13**?**]. For this class of methods, it is possible to obtain exponential rates of convergence with respect to DOF, even if the solution is locally non-smooth. This is the case for many application problems, such as those containing material interfaces, sharp edges, or reentrant corners. Goal-oriented hp-adaptive finite element methods have already been devised for various time-harmonic Maxwell problems [13, 47, 70] and exponential convergence has been demonstrated experimentally for non-trivial test cases. For the time-dependent Maxwell system under consideration, spatially hp-refined finite-element discretizations in combination with low-order finite-difference time-discretizations have been successfully explored in [54, 56, 57]. However the question of error-control has not been addressed so far for the time-dependent Maxwell equations. Since a time-dependent problem is considered, it is important to be able to control errors introduced by the spatial- as well as temporal discretizations. To this end, the following two points are of fundamental importance

- The discretization method should be of high-order accuracy in space and time and allow for local refinement in space and in time.
- The discretization error in the QOI needs to be estimated accurately for the purpose of serving as a stopping criterion. Further, local refinement indicators are needed within an adaptive algorithm.

These points are addressed in this thesis.

1.2 Outline

In chapter 2 of this work, the governing Maxwell equations and some important properties, namely energy conservation and continuity conditions are introduced. Furthermore, the modeling of scattering problems in unbounded domains is described.

Chapter 3 is devoted to the development of a space-time discontinuous Galerkin method, which allows for locally hp-refined discretizations of the space-time domain. It will be shown, that the developed method preserves the important property of energy conservation, inherent to Maxwell's equations. It is also unconditionally stable. Furthermore, under some restrictions, the full *a priori* error analysis is carried out, fully explicit in the discretization parameters h and p, where h denotes the mesh size and p the degree of the approximating polynomials. Furthermore, implementation strategies are presented. They allow for efficient iterative solution of the resulting linear systems of equations. The chapter is concluded with numerical experiments showing for the first time space-time hp-adaptive simulations, where local hp-refinement is also applied with respect to time.

In chapter 4, an extension of the developed space-time discontinuous Galerkin method is presented, which allows for the efficient discretization of waveguide structures by employing waveguide-mode basis functions. The extension is natural in the space-time discontinuous Galerkin framework. It allows, on the one hand, for the efficient and accurate modeling of waveguide ports and on the other hand,

for consideration within *a priori* and *a posteriori* error estimates.
Chapter 5 deals with the accurate approximation of QOIs by means of error controlled *hp*-adaptive simulations. To this end, an *a posteriori* error estimate is derived. It employs the established mathematical framework of adjoint-based error estimation [8], [19]. Furthermore, under some restrictions, the *hp*-*a priori* error analysis for QOIs is carried out and the result confirms improved convergence rates. The analysis extends results, which were established for other types of equations (see eg. [19], [22]). The chapter is concluded with numerical experiments. These include goal-oriented space-time *hp*-adaptive simulations of test problems, showing exponential convergence of the numerically obtained QOIs towards reference solutions in the context of the time-dependent Maxwell equations. Furthermore, it is demonstrated, that the derived *a posteriori* error estimator yields accurate estimates of the actual error.

2 The Physical Setting - Classical Electrodynamics

In this chapter, the governing equations, material laws, and boundary conditions are introduced. Further, Poynting's theorem, a conservation law for the electromagnetic energy, is derived, since a discrete version will play an important role in the stability analysis of the numerical method presented in chapter 3. Finally the scattered field formulation of Maxwell's equations is recalled, as it is employed in numerical examples considered in this thesis.

2.1 Maxwell's Equations

In 1861 J.C. Maxwell axiomatically stated a set of equations which describe the phenomena of electromagnetism in continuous media. Maxwell's equations can be written as the following system of partial differential equations (PDEs)

$$\begin{aligned}
&\frac{\partial \mathbf{D}}{\partial t} - \nabla \times \mathbf{H} + \mathbf{J} = 0, && \text{Ampère's law}\\
&\frac{\partial \mathbf{B}}{\partial t} + \nabla \times \mathbf{E} = 0, && \text{Faraday's law}\\
&\nabla \cdot \mathbf{D} = \rho \quad \nabla \cdot \mathbf{B} = 0, && \text{Coulomb's law and absence of free magnetic poles}
\end{aligned} \tag{2.1}$$

with the electric and magnetic fields **E** and **H**, the electric displacement **D**, and the magnetic flux density **B**. The current density **J** can be decomposed into an external source term $\mathbf{J}_e$ independent of the fields, the conductive current density $\mathbf{J}_\sigma$, and the convective current density $\mathbf{J}_c$ due to free charges as

$$\mathbf{J} = \mathbf{J}_e + \mathbf{J}_\sigma + \mathbf{J}_c. \tag{2.2}$$

The above quantities are measured in the units

Physical quantity		unit
Electric field	$\mathbf{E}$	V/m
Magnetic field	$\mathbf{H}$	A/m
Electric displacement	$\mathbf{D}$	$\mathrm{As/m^2}$
Magnetic flux density	$\mathbf{B}$	$\mathrm{Vs/m^2}$
Current density	$\mathbf{J}$	$\mathrm{A/m^2}$
Charge density	ρ	$\mathrm{C/m^3}$

Finally, we note that we require $\rho = 0$ and $\mathbf{J}_c = 0$ in this work.

2.1.1 Constitutive Equations

The system (2.1) is closed with constitutive laws, which connect the fields $\mathbf{E}$ and $\mathbf{H}$ with the flux quantities $\mathbf{D}, \mathbf{B}$ and $\mathbf{J}$. In this thesis we consider linear, isotropic, non-dispersive, non-permanent-magnetic constitutive laws, which are a good approximation in many cases for high frequency problems:

$$\mathbf{D} = \varepsilon\mathbf{E}, \quad \mathbf{B} = \mu\mathbf{H}, \quad \mathbf{J}_\sigma = \sigma\mathbf{E}. \tag{2.3}$$

In the general case of anisotropic media, the electric permittivity ε, the magnetic permeability μ and the conductivity σ are tensorial, time invariant quantities measured in the units As/Vm, Vs/Am and A/Vm. In the case of isotropic media, the quantities become scalar valued. For the special but important case of vacuum, there holds $\varepsilon_0 = 8.8542 \cdot 10^{-12}\mathrm{As/Vm}$, $\mu_0 = 4\pi \cdot 10^{-7}\mathrm{Vs/Am}$ and $\sigma = 0$.

2.1.2 Initial and Boundary Conditions

Inserting the constitutive laws into the system (2.1) and applying the divergence operator to the first two equations, it can easily be seen, that the last two equations are fulfilled automatically for all times, provided they hold at the initial time. Thus, the system (2.1) is overdetermined. Taking this into account we obtain

$$\begin{aligned}
&\varepsilon\frac{\partial \mathbf{E}}{\partial t} - \nabla \times \mathbf{H} + \mathbf{J} = 0 \quad \text{in } (0,T] \times \Omega \\
&\mu\frac{\partial \mathbf{H}}{\partial t} + \nabla \times \mathbf{E} = 0 \quad \text{in } (0,T] \times \Omega \\
&\mathbf{E}(x,0) = \mathbf{E}_0, \quad \mathbf{H} = \mathbf{H}_0, \quad \nabla \cdot (\varepsilon\mathbf{E}) = 0, \quad \nabla \cdot (\mu\mathbf{H}) = 0 \text{ in } \Omega,\ t = 0 \\
&+ \text{boundary conditions} \quad \text{on } (0,T] \times \partial\Omega.
\end{aligned} \tag{2.4}$$

Interface and Boundary Conditions

For the fields near a material interface S between two materials with material parameters ε_1, μ_1 and ε_2, μ_2 there holds

$$\begin{aligned}(\mathbf{D}_1 - \mathbf{D}_2)\cdot\mathbf{n} = \rho_S, \quad (\mathbf{B}_1 - \mathbf{B}_2)\cdot\mathbf{n} = 0,\\ \mathbf{n}\times(\mathbf{E}_1 - \mathbf{E}_2) = 0, \quad \mathbf{n}\times(\mathbf{H}_1 - \mathbf{H}_2) = \mathbf{J}_S,\end{aligned} \tag{2.5}$$

where ρ_S denotes a surface charge density and $\mathbf{J}_S$ is a surface current density. Thus, the tangential component of the electric field and the normal component of the magnetic flux density is continuous at a material interface. In general, the normal component of the electric displacement is continuous up to the surface charge density and the tangential component of magnetic field is continuous up to the surface current.

For the case of a perfect electrical conductor on one side of the interface, the perfectly conducting boundary (PEC) condition

$$\mathbf{n}\times\mathbf{E} = 0, \quad \mathbf{n}\cdot\mathbf{B} = 0, \tag{2.6}$$

is obtained by taking into account that the fields vanish inside the perfect conductor.

2.1.3 Poynting's Theorem

The conservation law for the electromagnetic energy is given by Poynting's theorem. A discrete version of this theorem will be employed in the following chapter in order to show stability of the discretized Maxwell system.

Taking the inner product of Ampere-Maxwell's and Faraday's law with $\mathbf{E}$ and $\mathbf{H}$ respectively, integrating both equations over a volume V and then adding the result yields

$$\begin{aligned}&\int_V \frac{\partial \mathbf{D}}{\partial t}\cdot\mathbf{E}\,\mathrm{d}x + \int_V \frac{\partial \mathbf{B}}{\partial t}\cdot\mathbf{H}\,\mathrm{d}x - \int_V (\nabla\times\mathbf{H}\cdot\mathbf{E})\,\mathrm{d}x + \int_V (\nabla\times\mathbf{E}\cdot\mathbf{H})\,\mathrm{d}x\\ &= \int_V \frac{\partial \mathbf{D}}{\partial t}\cdot\mathbf{E}\,\mathrm{d}x + \int_V \frac{\partial \mathbf{B}}{\partial t}\cdot\mathbf{H}\,\mathrm{d}x + \int_V \nabla\cdot(\mathbf{E}\times\mathbf{H})\,\mathrm{d}x = -\int_V \mathbf{J}\cdot\mathbf{E}\,\mathrm{d}x.\end{aligned}$$

Thus, denoting the electromagnetic energy density by $w = \frac{1}{2}(\mathbf{D}\cdot\mathbf{E} + \mathbf{B}\cdot\mathbf{H})$ and the energy flux density by $\mathbf{S} = \mathbf{E}\times\mathbf{H}$, we obtain Poynting's theorem

$$\frac{\partial w}{\partial t} + \nabla\cdot\mathbf{S} = -\mathbf{J}\cdot\mathbf{E}. \tag{2.7}$$

If $\mathbf{J} = 0$, the electromagnetic energy is conserved for all times.

2.1.4 Non-Dimensionalization

In this thesis, Maxwell's equations are often used in a non-dimensional form [27], which is obtained by introducing a reference length L and reference magnetic field strength H_0. Denoting $Z_0 = \sqrt{\mu_0/\varepsilon_0}$, the non-dimensional form is given by

$$\widetilde{\mathbf{x}} = \mathbf{x}/L, \quad \widetilde{t} = t/(L/c_0), \quad \widetilde{\mathbf{E}} = \mathbf{E}/(Z_0 H_0) \quad \widetilde{\mathbf{H}} = \mathbf{H}/H_0 \quad \widetilde{\mathbf{J}} = \mathbf{J}L/H_0. \tag{2.8}$$

In order to simplify notation, the dimensional and non-dimensional forms of (2.4) are not explicitly distinguished. If results in dimensional form are presented, they were obtained by scaling the non-dimensionalized quantities according to (2.8).

2.2 Scattering problems

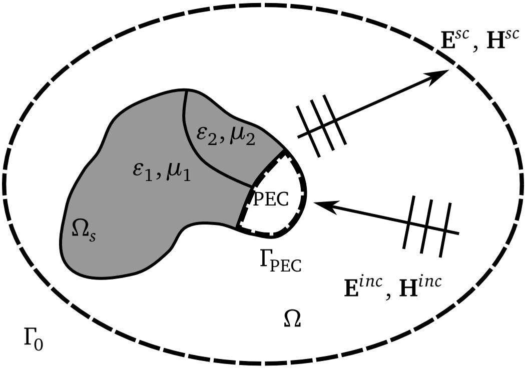

Figure 2.1: Scattering by an object consisting of multiple materials

An important class of electromagnetic problems are scattering problems as depicted in Fig. 2.1. Here, an object, occupying a domain Ω_s possibly being composed of different materials is illuminated by an incoming electromagnetic wave $\mathbf{E}^{inc}$, $\mathbf{H}^{inc}$. Note that PEC regions with boundary Γ_{PEC} are excluded from the computational domain Ω and modeled by a PEC boundary condition on Γ_{PEC}. One usually is interested in the back-scattered fields $\mathbf{E}^{sc}$, $\mathbf{H}^{sc}$, or certain derived quantities depending on the scattered fields.

2.2.1 Modeling of an Unbounded Domain

In order to model an unbounded computational domain, we shall also consider the Silver-Mueller radiation conditions for the scattered fields

$$\lim_{r\to\infty} r\left[\mathbf{H}^{sc} - \sqrt{\varepsilon/\mu}\,\mathbf{x}\times\mathbf{E}^{sc}\right] = 0,$$
$$\lim_{r\to\infty} r\left[\mathbf{E}^{sc} + \sqrt{\mu/\varepsilon}\,\mathbf{x}\times\mathbf{H}^{sc}\right] = 0,$$

where $\mathbf{x} = \mathbf{r}/r, r = |\mathbf{r}|, \mathbf{r} \in \mathbb{R}^3$. The Silver-Mueller radiation conditions can be approximated on a bounded domain with exterior boundary Γ_0 in the form of an impedance boundary condition

$$\begin{aligned}\mathbf{n}\times\mathbf{E}^{sc} + \sqrt{\mu/\varepsilon}\,\mathbf{n}\times(\mathbf{n}\times\mathbf{H}^{sc}) &= 0 \text{ on } \Gamma_0,\\ \mathbf{n}\times\mathbf{H}^{sc} - \sqrt{\varepsilon/\mu}\,\mathbf{n}\times(\mathbf{n}\times\mathbf{E}^{sc}) &= 0 \text{ on } \Gamma_0.\end{aligned} \tag{2.9}$$

However it has to be noted, that the Silver-Mueller boundary condition is an approximation which is exact only for outgoing plane waves propagating in direction of the outer surface normal **n**.

2.2.2 Scattered Field Formulation

Whenever the incoming fields are known explicitly, for example in the form of a plane-wave solution, it is desirable to solve for the scattered field only in order to save computational resources. The linearity of the Maxwell's equations in (2.4) allows to decompose the total fields into scattered and incoming fields as

$$\mathbf{E} = \mathbf{E}^{\text{sc}} + \mathbf{E}^{\text{inc}}, \qquad \mathbf{H} = \mathbf{H}^{\text{sc}} + \mathbf{H}^{\text{inc}}. \tag{2.10}$$

Inserting (2.10) into (2.4) and taking into account that $\mathbf{E}^{inc}$, $\mathbf{H}^{inc}$ are solutions to (2.4) where $\varepsilon = \varepsilon^{\text{inc}}, \mu = \mu^{\text{inc}}, \sigma = \sigma^{\text{inc}}$ denote the material properties of the medium enclosing the scatterer, one obtains a scattered field formulation of the Maxwell system

$$\begin{aligned}
&\varepsilon\frac{\partial\mathbf{E}^{\text{sc}}}{\partial t} - \nabla\times\mathbf{H}^{\text{sc}} = (\varepsilon^{\text{inc}}-\varepsilon)\frac{\partial\mathbf{E}^{\text{inc}}}{\partial t} + (\sigma^{\text{inc}}-\sigma)\mathbf{E}^{\text{inc}} - \mathbf{J}_e && \text{in } (0,T]\times\Omega,\\
&\mu\frac{\partial\mathbf{H}^{\text{sc}}}{\partial t} + \nabla\times\mathbf{E}^{\text{sc}} = (\mu^{\text{inc}}-\mu)\frac{\partial\mathbf{H}^{\text{inc}}}{\partial t} && \text{in } (0,T]\times\Omega,\\
&\mathbf{n}\times\mathbf{E}^{\text{sc}} = -\mathbf{n}\times\mathbf{E}^{\text{inc}} && \text{on } (0,T]\times\Gamma_{\text{PEC}},\\
&\mathbf{n}\times\mathbf{E}^{sc} + \sqrt{\mu/\varepsilon}\,\mathbf{n}\times(\mathbf{n}\times\mathbf{H}^{sc}) = 0 && \text{on } (0,T]\times\Gamma_0,\\
&+\text{ initial conditions.}
\end{aligned} \tag{2.11}$$

Usually the initial conditions for the scattered field are chosen to be zero.

2.2.3 Radar Cross Section and Near to Farfield Transform

An important quantity of interest is the radar cross section (RCS)

$$\sigma(\phi,\theta;\omega) = \lim_{r\to\infty} 4\pi r^2 \frac{|\underline{\mathbf{E}}^{\text{scfar}}(r,\phi,\theta;\omega)|^2}{|\underline{\mathbf{E}}^{\text{inc}}(r,\phi,\theta;\omega)|^2} = 0. \tag{2.12}$$

Here r denotes the distance from the center of the scatterer to the point of observation $\mathbf{x}(\phi,\theta)$, ϕ and θ are the azimuthal and polar angle between the wave vector and $\mathbf{x}$. The scattered far field $\underline{\mathbf{E}}^{\text{scfar}}$ for wave number κ, corresponding to the circular frequency ω, can be evaluated at any closed surface S around the scatterer. It is given by the field integral equation [13, 33]

$$\underline{\mathbf{E}}^{\text{scfar}}(r,\phi,\theta;\omega) = \frac{e^{-i\omega r}}{4\pi r} \int_0^\infty \int_S [\mathbf{x}\times(\mathbf{x}\times(\mathbf{n}\times\mathbf{H})) + \mathbf{x}\times(\mathbf{E}\times\mathbf{n})]\, e^{i\kappa\mathbf{x}\cdot\mathbf{y}+i\omega t}\, \mathrm{d}S(\mathbf{y})\,\mathrm{d}t, \tag{2.13}$$

where the integration with respect to time and the factor $e^{i\omega t}$ arise due to the Fourier transform from time to frequency domain.

3 Space-time Galerkin Discretization of Maxwell's Equations

Popular methods for the numerical solution of the time-dependent Maxwell system (2.4) are the Finite-Difference Time-Domain method (FDTD) [69] and the closely related Finite Integration Technique (FIT) [67]. They often combine Cartesian dual-orthogonal grid pairs and an explicit symplectic time-integration method such as the leap-frog scheme to a computationally extremely efficient algorithm. If the leap-frog scheme is applied for time integration, the resulting algorithm is second order accurate in space and time. Additionally, the discretization preserves important physical properties of the Maxwell system such as the conservation of energy and charge. However, the use of Cartesian grids demands very fine grid resolutions for problems with complicated geometries. The inherent second order accuracy of the method also becomes an issue if very small discretization errors are required. The latter is particularly true for the simulation of electrically large structures, which are dominated by dispersion errors. Also local refinement in space and in time as it is desirable in an adaptive context, is not straightforward.

Conforming finite element methods [52, 53] employing Nedelec's families of finite elements [45, 46] constitute another approach. Conceptually, this allows for arbitrarily high order discretizations in space. Meshes consisting of various shapes of elements as tetrahedra, hexahedra, prisms or pyramids can be employed. This allows for discretizing complicated geometries with possibly curved boundaries in an accurate way. Furthermore, local hp-refinement is possible (see eg.[13]), which makes the method attractive for adaptive simulations. Unfortunately, the continuity of the finite element spaces, makes it necessary to introduce special transition elements when local hp-refinement is desired [13].

The latter is not required for discontinuous Galerkin (DG) methods, which became a popular tool for the numerical solution of Maxwell's equations in the past decade [12, 18, 27]. Here, the approximations are allowed to be discontinuous at the element interfaces and continuity is imposed weakly by the introduction of a numerical flux. This opens up the possibility to employ variable local approximations including hp-refinement ([31], [56]) and special basis functions taylored to the specific problem [36].

The DG method is often applied in space, whereas time is discretized with an explicit time integrator. This leads to a conditionally stable method, where the maximal stable time-step is determined by a Courant Friedrichs Levy (CFL) condition. The CFL condition itself depends on element size and polynomial degree. In order to achieve stability for non-uniform discretizations, the minimum of all element-wise computed CFL time steps has to be applied. Thus, for explicit time-integrators, the temporal resolution is determined by stability instead of accuracy requirements. This issue has been addressed by the introduction of local time-stepping [12, 49, 61], and locally implicit (IMEX) schemes [14, 15], which can lead to good speed-ups on locally refined discretizations. Nevertheless, refinement in time is still introduced for stability reasons rather than accuracy.

An alternative approach are space-time DG methods [64], where space and time are simultaneously discretized with finite elements. This allows for local hp-refinement in space and time in a natural way. The resulting methods are unconditionally stable. Thus, due to their high flexibility, they are a promising candidate for space-time adaptivity. However, the application of the DG approach in time leads to the introduction of non-physical dissipation. The amount of dissipation depends on the respective polynomial degree employed for the time variable. In the case of piecewise constant polynomials in time, the space-time DG method corresponds to a spatial DG discretization combined with an implicit Euler method in time, which is known to be highly dissipative. For higher-order approximation in time, dissipation decreases.

In this work, a continuous Galerkin approach in temporal direction is combined with a DG approach in the spatial directions. This allows for obtaining a non-dissipative method, which allows for local space-time hp refinement and can be proven to be unconditionally stable [40]. If a uniform time-step and a uniform approximation order is choosen for all elements in the spatial mesh, this method corresponds to certain symplectic Gauss-Runge-Kutta methods in time combined with a DG discretization in space. Moreover for linear basis functions in time-direction, the Crank-Nicholson method is obtained. In this chapter the space-time discontinuous Galerkin method from [40] is presented and analyzed with respect to stability and consistency. This will yield, for the special case of no local refinement in time to hp-error estimates in the $\|\cdot\|_{L^\infty(0,T;\mathrm{L}^2(\Omega))}$- and $\|\cdot\|_{L^2(0,T;\mathrm{L}^2(\Omega))}$-norms. Further it is discussed, how the residual can be efficiently evaluated in a matrix free implementation with a complexity of $\mathcal{O}(p^4)$ and $\mathcal{O}(p^5)$ for affine and non-affine elements, respectively. Together with an *a posteriori* error indicator for the iteration error, the arising linear systems can be solved inexactly without compromising the overall accuracy. The chapter is concluded with numerical experiments, demonstrating the feasibility of the presented approach for fully space-time hp-adaptive simulations.

3.1 A Space-Time Discontinuous Galerkin Method

In this section, the notation and the space-time Galerkin method from [40] are introduced. Furthermore, basic consistency results are stated.
We consider the slightly simplified problem

$$\begin{aligned}
&\varepsilon \partial_t \mathbf{E} - \nabla \times \mathbf{H} = \mathbf{J} && \text{in } \Omega \times (0,T] \\
&\mu \partial_t \mathbf{H} + \nabla \times \mathbf{E} = 0 && \text{in } \Omega \times (0,T] \\
&\mathbf{n} \times \mathbf{E} = \mathbf{n} \times \mathbf{g} && \text{on } \partial\Omega \times (0,T] \\
&\mathbf{E} = \mathbf{E}_0, \;\; \mathbf{H} = \mathbf{H}_0 && \text{in } \Omega \times \{0\}.
\end{aligned} \tag{3.1}$$

The extension to Silver-Mueller boundary conditions as well as conducting media is straight-forward.

3.1.1 Function Spaces

We denote vector valued function spaces with bold letters, e.g. $\mathbf{L}^2(D) := [L^2(D)]^3$. We introduce the spaces

$$\begin{aligned}
\mathbf{H}(curl, \Omega) &:= \{\mathbf{v} \in \mathbf{L}^2(\Omega) : \nabla \times \mathbf{v} \in \mathbf{L}^2(\Omega)\}, \\
\mathbf{H}_0(curl, \Omega) &:= \{\mathbf{v} \in \mathbf{L}^2(\Omega) : \nabla \times \mathbf{v} \in \mathbf{L}^2(\Omega), \mathbf{n} \times \mathbf{v} = 0 \text{ on } \partial\Omega\},
\end{aligned}$$

and recall, that for $\mathbf{g} = 0$ Maxwell's equations have a unique solution $\mathbf{u} = \{\mathbf{E}, \mathbf{H}\}$ in

$$\begin{aligned}
\mathbf{V} := &\, C^0([0,T], \mathbf{H}_0(curl, \Omega)) \cap C^1[0,T], \mathbf{L}^2(\Omega)) \\
&\times C^0([0,T], \mathbf{H}(curl, \Omega)) \cap C^1([0,T], \mathbf{L}^2(\Omega)).
\end{aligned} \tag{3.2}$$

For details see e.g. [51].

3.1.2 Partitioning of the Space-Time Domain

We derive the space-time DG method for hexahedral spatial meshes and note that a most of the results can be obtained with minor modifications for tetrahedral meshes, as well. By dividing the time axis in intervals $\mathcal{I}_n = (t_n, t_{n+1}]$, we partition the space-time cylinder $\mathcal{I} \times \Omega$ in time slabs $\mathcal{I}_n \times \Omega$. For each time slab, we partition the spatial domain Ω in non-overlapping hexahedral elements K resulting in a triangulation $\mathcal{T}_n(\Omega)$. Note, that the triangulation $\mathcal{T}_n(\Omega)$ is required to be a refinement of a coarse master-triangulation $\overline{\mathcal{T}}(\Omega)$. Furthermore, the obtained space-time macro-elements $\mathcal{I}_n \times K$ are refined in time direction $\mathcal{I}_n \times K = \bigcup_{k=1}^{N_K} \mathcal{I}_k^K \times K$, such that the time-slab $\mathcal{I}_n \times \Omega$ is partitioned in space-time elements $I_k^K \times K \in \mathcal{S}_n(\mathcal{I}_n \times \Omega)$. The obtained triangulation of the time slab is denoted by $\mathcal{S}_n(\mathcal{I}_n \times \Omega)$, see Fig. 3.1.

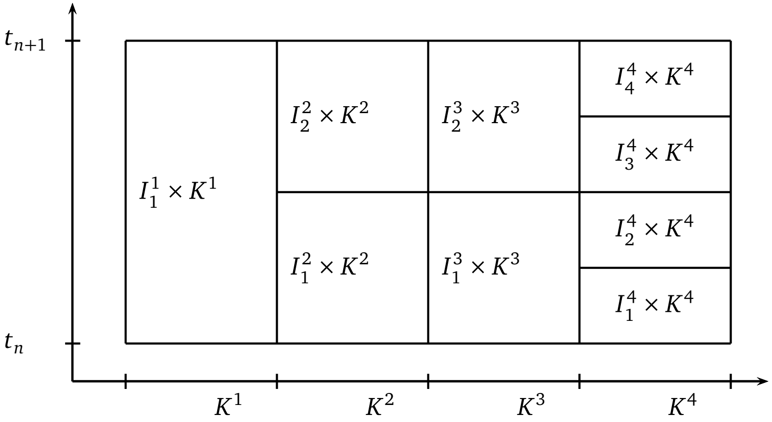

Figure 3.1: Example of a space-time triangulation $\mathcal{S}_n(\mathcal{I}_n \times \Omega)$

3.1.3 Discrete Spaces

By F_K we denote the mapping from the reference element $\widehat{K} = [0,1]^3$ with axes $\widehat{x}, \widehat{y}, \widehat{z}$ to the physical element $K = F_K(\widehat{K})$. Denoting by DF_K the Jacobian matrix of F_K, the fields are transformed using the covariant transformation $\mathbf{v}(x,t) = DF_K^{-T}\widehat{\mathbf{v}}(\widehat{x},t)oF_K^{-1}$, see [12].
Let $P_{p_t}(I)$ denote the space of polynomials of degree p_t on interval I. Further, $Q_{p_x,p_y,p_z}(\widehat{K})$ is the space of tensor product polynomials of degrees p_x, p_y and p_z in the $\widehat{x}, \widehat{y}, \widehat{z}$ directions.
We choose the local trial- and test-spaces as

$$\begin{aligned} V_{h,\widehat{K}}^k &:= P_{p_t}(I_k^K) \otimes \left[Q_{p_x,p_y,p_z}(\widehat{K})\right]^3, \\ W_{h,\widehat{K}}^k &:= P_{p_t-1}(I_k^K) \otimes \left[Q_{p_x,p_y,p_z}(\widehat{K})\right]^3. \end{aligned} \tag{3.3}$$

We require that the polynomial degrees p_t, p_x, p_y, p_z in (3.3) are identical[1] for all space-time elements $I_k^K \times \widehat{K}$ within one macro-element $\mathcal{I}_n \times \widehat{K}$. This leads to tensor

---

[1] For the temporal polynomial degree p_t this assumption is not essential.

product trial- and test spaces consisting of a spatial part $Q_{p_x,p_y,p_z}(\widehat{K})$ and spaces of piecewise polynomials in time, which we denote by $S_K(\mathcal{I}_n)$ and $T_K(\mathcal{I}_n)$.

$$\begin{aligned} V_{h,K} &:= S_K(\mathcal{I}_n) \otimes \left[Q_{p_x,p_y,p_z}(\widehat{K})\right]^3, \quad S_K(\mathcal{I}_n) := \{u(t) \in H^1(\mathcal{I}_n) : u\big|_{I_k^K} \in P_{p_t}(I_k^K)\} \\ V_{h,K} &:= T_K(\mathcal{I}_n) \otimes \left[Q_{p_x,p_y,p_z}(\widehat{K})\right]^3, \quad T_K(\mathcal{I}_n) := \{u(t) \in L^2(\mathcal{I}_n) : u\big|_{I_k^K} \in P_{p_t-1}(I_k^K)\}. \end{aligned} \tag{3.4}$$

Now we can define the global spaces for one time slab

$$V_h(\mathcal{I}_n \times \Omega; \mathbf{p}_n) := \{\mathbf{v}(t,\mathbf{x}) \in H^1(\mathcal{I}_n; L^2(\Omega)) : DF^T\mathbf{v}\big|_K oF \in V_{h,\widehat{K}}\}, \tag{3.5}$$

and

$$W_h(\mathcal{I}_n \times \Omega; \mathbf{p}_n) := \{\mathbf{v}(t,\mathbf{x}) \in L^2(\mathcal{I}_n; \Omega)) : DF^T\mathbf{v}\big|_K oF \in W_{h,\widehat{K}}\}, \tag{3.6}$$

where $\mathbf{p}_n$ denotes a vector containing the polynomial degrees. Note, that trial functions from V_h are continuous while test functions from W_h are discontinuous with respect to time. In the spatial directions test- and trial functions are allowed to be discontinuous. The situation is illustrated in Fig. 3.2 for an example with three space-time elements.

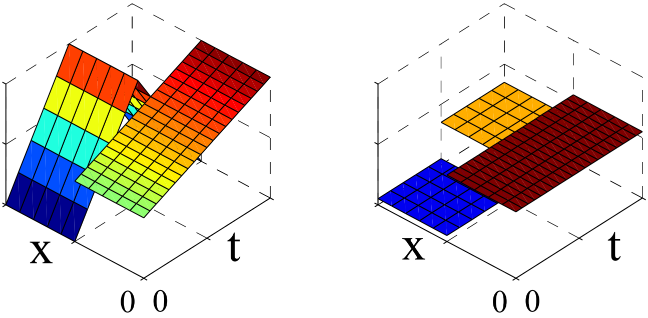

Figure 3.2: Left: a function from the trial space V_h, right: a function from the corresponding test space W_h

Finally, we set $\mathbf{V}_h^n(\mathcal{I}^n \times \Omega) := V_h(\mathcal{I}^n \times \Omega) \times V_h(\mathcal{I}^n \times \Omega)$ and $\mathbf{W}_h^n(\mathcal{I}^n \times \Omega) := W_h(\mathcal{I}^n \times \Omega) \times W_h(\mathcal{I}^n \times \Omega)$.

Assumptions on the discretization

For the *a priori* error analysis we frequently make use of the following assumptions:

Assumption 3.1.1 (Element-wise constant materials). *The electric permittivity* ε *and magnetic permeability* μ *are element-wise constant and* $\varepsilon \geq \underline{\varepsilon} > 0, \mu \geq \underline{\mu} > 0$.

Assumption 3.1.2 (Global *hp*-refinement in time). *Within each time-slab the space-time macro elements* $\mathcal{I}_n \times K$ *are not locally refined with respect to time (uniform time step). Furthermore, the temporal polynomial degree* p_t *is uniform with each time step.*

Assumption 3.1.2 implies that $S_K(\mathcal{I}_n)$ and $T_K(\mathcal{I}_n)$ are uniform for all spatial elements K. Note, that assumption 3.1.2 allows that the global time-step $\Delta t_n = t_{n+1} - t_n$ and the temporal polynomial-degree may be non-uniform for different time-slabs. This corresponds to the choice of different single-rate time-integrators for each time-step.
Furthermore, for simplicity we often make the assumption that the spatial part of the discretization is fixed for all time-slabs:

Assumption 3.1.3 (Fixed spatial discretization and exact representation of the initial data). *The spatial part of the discretization, more precisely the spatial mesh and spatial polynomial degrees are fixed for all time-slabs, i.e.* $\mathcal{T}_n(\Omega) = \mathcal{T}(\Omega)$ *and* $\mathbf{p}_n = \mathbf{p}$. *Furthermore, the initial data can be represented exactly, i.e.* $\mathbf{u}_h^1(0) = \mathbf{u}(0)$.

In section 3.2.5 we comment on the extension of the error analysis to variable discretizations. It will turn out, that in this case additional terms arise due to projection errors.

3.1.4 Faces and Trace Operators

Let $\mathcal{F}$ denote the set of faces in the spatial triangulation $\mathcal{T}(\Omega)$. Furthermore, $\mathcal{F}_0$ is the set of interior faces $f := \partial K^1 \cap \partial K^2 \ : \ K^1,\ K^2 \in \mathcal{T}(\Omega)$ and $\mathcal{F}_b$ is the set of boundary faces $f := \partial K \cap \partial \Omega \ : \ K \in \mathcal{T}(\Omega)$.
We define the average and tangential jump operators as

$$\begin{aligned} \{\mathbf{v}\} &:= (\mathbf{v}^1 + \mathbf{v}^2)/2 \ \text{ on } f \in \mathcal{F}_0, & \{\mathbf{v}\} &:= \mathbf{v} \ \text{ on } f \in \mathcal{F}_b, \\ [\![\mathbf{v}]\!]_T &:= \mathbf{n}^1 \times \mathbf{v}^1 + \mathbf{n}^2 \times \mathbf{v}^2 \ \text{ on } f \in \mathcal{F}_0, & [\![\mathbf{v}]\!]_T &:= \mathbf{n} \times \mathbf{v} \ \text{ on } f \in \mathcal{F}_b, \end{aligned}$$

where $\mathbf{v}^1$ and $\mathbf{v}^2$ are the traces of $\mathbf{v}$ on f taken from within element K^1 and K^2 with outward unit normals $\mathbf{n}^1$ and $\mathbf{n}^2$.

3.1.5 Discrete Variational Problem: Discretizations with Global hp-Refinement in Time

In this section we consider the discretization of a single time-slab $\mathcal{I}_n \times \Omega$. We restrict the presentation to discretizations with global refinement with respect to time, see assumption 3.1.2. The more general case is treated in the next section. Furthermore, for simplicity we require that assumption 3.1.3 holds.

By multiplying (3.1) by smooth test functions $\mathbf{w}_E, \mathbf{w}_H$, integrating on a macro-element $\mathcal{I}_n \times K$ and then integrating by parts the curl-terms we obtain

$$\begin{aligned}
&\int_{\mathcal{I}_n}\int_K \varepsilon\partial_t \mathbf{E}\cdot\mathbf{w}_E \,\mathrm{d}x\,\mathrm{d}t - \int_{\mathcal{I}_n}\int_K \mathbf{H}\cdot\nabla\times\mathbf{w}_E \,\mathrm{d}x\,\mathrm{d}t \\
&-\int_{\mathcal{I}_n}\int_{\partial K} \mathbf{n}\times\mathbf{H}^*\cdot\mathbf{w}_E \,\mathrm{d}S\,\mathrm{d}t = \int_{\mathcal{I}_n}\int_K \mathbf{J}\cdot\mathbf{w}_E \,\mathrm{d}x\,\mathrm{d}t \\
&\int_{\mathcal{I}_n}\int_K \mu\partial_t \mathbf{H}\cdot\mathbf{w}_H \,\mathrm{d}x\,\mathrm{d}t + \int_{\mathcal{I}_n}\int_K \nabla\times\mathbf{E}\cdot\mathbf{w}_H \,\mathrm{d}x\,\mathrm{d}t \\
&+\int_{\mathcal{I}_n}\int_{\partial K} \mathbf{n}\times(\mathbf{E}^*-\mathbf{E})\cdot\mathbf{w}_H \,\mathrm{d}S\,\mathrm{d}t = 0,
\end{aligned} \tag{3.7}$$

where $\mathbf{E}^*$ and $\mathbf{H}^*$ are the numerical fluxes. We choose

$$\begin{aligned}
&\mathbf{E}^* = \{\mathbf{E}_h\} - \alpha_E[\![\mathbf{H}_h]\!]_T \text{ on } \mathcal{F}_i, \quad \mathbf{E}^* = \mathbf{g} \text{ on } \mathcal{F}_b \\
&\mathbf{H}^* = \{\mathbf{H}_h\} + \alpha_H[\![\mathbf{E}_h]\!]_T \text{ on } \mathcal{F}_0, \quad \mathbf{H}^* = \{\mathbf{H}_h\} + \alpha_H[\![\mathbf{E}_h - \mathbf{g}]\!]_T \text{ on } \mathcal{F}_b \\
&\alpha_E = c\{\sqrt{\mu/\varepsilon}\}^{-1}, \quad \alpha_H = c\{\sqrt{\varepsilon/\mu}\}^{-1}, \quad c \geq 0.
\end{aligned} \tag{3.8}$$

By setting $c = \alpha_E = \alpha_H = 0$ we obtain a non-dissipative centered-flux formulation [18] and by choosing $c > 0$ we obtain a dissipative upwind-type formulation [27, 44]. Adding dissipation to the formulation can have advantages when the problem under consideration features strong singularities or when parts of the solution are kept under-resolved, as it is often the case when goal-oriented adaptivity is employed.

By substituting $\mathbf{u} := \{\mathbf{E}, \mathbf{H}\} \in \mathbf{V}$ in (3.7) with the discrete fields $\mathbf{u}_h := \{\mathbf{E}_h, \mathbf{H}_h\} \in \mathbf{V}_h^n$, summing over all $\mathcal{I}_n \times K$, we get the discrete variational formulation

$$\begin{aligned}
&\text{Find } \mathbf{u}_h^n \in \mathbf{V}_h^n \quad \text{such that} \\
&B_h^n(\mathbf{u}_h, \mathbf{w}) := C_h^n(\mathbf{u}_h, \mathbf{w}) + D_h^n(\mathbf{u}_h, \mathbf{w}) = L_h^n(\mathbf{w}) \;\forall\; \mathbf{w} \in \mathbf{W}_h^n \\
&\mathbf{u}_h^n(t_n) = \mathbf{u}_h^{n-1}(t_n)
\end{aligned} \tag{3.9}$$

with the forms

$$
\begin{aligned}
C_h(\mathbf{u}_h,\mathbf{w}) :=& \int_{\mathcal{I}_n}\int_\Omega \varepsilon\partial_t \mathbf{E}_h\cdot\mathbf{w}_E \,\mathrm{d}x\,\mathrm{d}t + \int_{\mathcal{I}_n}\int_\Omega \mu\partial_t \mathbf{H}_h\cdot\mathbf{w}_H \,\mathrm{d}x\,\mathrm{d}t +\\
&- \int_{\mathcal{I}_n}\int_\Omega \mathbf{H}_h\cdot\nabla_h\times\mathbf{w}_E \,\mathrm{d}x\,\mathrm{d}t + \int_{\mathcal{I}_n}\int_\Omega \nabla_h\times\mathbf{E}_h\cdot\mathbf{w}_H \,\mathrm{d}x\,\mathrm{d}t\\
&+ \int_{\mathcal{I}_n}\int_{\mathcal{F}_0\cup\mathcal{F}_b} \{\mathbf{H}_h\}\cdot[\![\mathbf{w}_E]\!]_T \,\mathrm{d}S\,\mathrm{d}t - \int_{\mathcal{I}_n}\int_{\mathcal{F}_0\cup\mathcal{F}_b} [\![\mathbf{E}_h]\!]_T\cdot\{\mathbf{w}_H\} \,\mathrm{d}S\,\mathrm{d}t
\end{aligned}
\tag{3.10}
$$

and

$$
D_h^n(\mathbf{u}_h,\mathbf{w}) := \int_{\mathcal{I}_n}\int_{\mathcal{F}} \alpha_E[\![\mathbf{E}_h]\!]_T\cdot[\![\mathbf{w}_E]\!]_T \,\mathrm{d}S\,\mathrm{d}t + \int_{\mathcal{I}_n}\int_{\mathcal{F}_0} \alpha_H[\![\mathbf{H}_h]\!]_T\cdot[\![\mathbf{w}_H]\!]_T \,\mathrm{d}S\,\mathrm{d}t,
\tag{3.11}
$$

and the linear-forms

$$
\begin{aligned}
&L_h^n(\mathbf{w}) := \ell_E^n(\mathbf{w}_E) + \ell_H^n(\mathbf{w}_H)\\
&\ell_E^n(\mathbf{w}_E) = \int_{\mathcal{I}_n}\int_\Omega \mathbf{J}\cdot\mathbf{w}_E \,\mathrm{d}x\,\mathrm{d}t + \int_{\mathcal{I}_n}\int_{\mathcal{F}_b} \alpha_E\mathbf{g}\cdot[\![\mathbf{w}_E]\!]_T \,\mathrm{d}S\,\mathrm{d}t, \quad \ell_H^n(\mathbf{w}_H) = -\int_{\mathcal{I}_n}\int_{\mathcal{F}_b} \mathbf{n}\times\mathbf{g}\cdot\mathbf{w}_H \,\mathrm{d}S
\end{aligned}
$$

containing volume and boundary source terms.
Inserting the exact solution to (3.1) into (3.9), we obtain by integration by parts

$$
\begin{aligned}
&-\int_{\mathcal{I}_n}\int_\Omega \mathbf{H}_h\cdot\nabla_h\times\mathbf{w}_E \,\mathrm{d}x\,\mathrm{d}t + \int_{\mathcal{I}_n}\int_{\mathcal{F}} \{\mathbf{H}\}\cdot[\![\mathbf{w}_E]\!]_T \,\mathrm{d}S\,\mathrm{d}t = -\int_{\mathcal{I}_n}\int_\Omega \nabla_h\times\mathbf{H}\cdot\mathbf{w}_E \,\mathrm{d}x\,\mathrm{d}t\\
&+\int_{\mathcal{I}_n}\int_{\mathcal{F}_0} [\![\mathbf{H}]\!]_T\cdot\{\mathbf{w}_E\} \,\mathrm{d}S\,\mathrm{d}t.
\end{aligned}
$$

Noting that $[\![\mathbf{E}]\!]_T = [\![\mathbf{H}]\!]_T = 0$, we obtain Galerkin orthogonality and thus consistency of the method (3.9).

Theorem 3.1.1. *Under assumptions 3.1.2 and 3.1.3, there holds*

$$
B_h^n(\mathbf{u}-\mathbf{u}_h,\mathbf{w}) = 0 \ \forall\ \mathbf{w}\in\mathbf{W}_h^n.
\tag{3.12}
$$

3.1.6 Extension to Discretizations with Local hp-Refinement in Time

The stability analysis in section 3.2.1 will show that (3.9) is not $\mathbf{L}^2(\Omega)$-stable, when assumption 3.1.2 does not hold. However, in section 3.2.2 we will show that $\mathbf{L}^2(\Omega)$-stability can be recovered by adding a suitable stabilization form S_h.

We consider an interior space-time face $\mathcal{I}_n \times f, f \in \mathcal{F}_0$, which is shared by two space-time macro-elements $\mathcal{I}_n \times K^i, i = 1,2$. We define $\pi_{\widetilde{T}f} : L^2(\mathcal{I}_n) \to \widetilde{T}(\mathcal{I}_n)$ as the L^2-orthogonal projection operator onto the space $\widetilde{T}(\mathcal{I}_n) := T_{K^1}(\mathcal{I}_n) \cap T_{K^2}(\mathcal{I})$, i.e. the largest common temporal test space. Moreover, we define $\pi_{\widetilde{T}}$ as the projection operator whose restriction to each $\mathcal{I}_n \times f$ is $\pi_{\widetilde{T}f}$.
We complement (3.9) with the stabilization form

$$\begin{aligned}
S_h^n(\mathbf{u}_h, \mathbf{w}) := \frac{1}{2}\Bigg(&\int_{\mathcal{I}_n}\int_{\mathcal{F}_0} \{\mathbf{H}_h\} \cdot [\![\pi_{\widetilde{T}}\mathbf{w}_E - \mathbf{w}_E]\!]_T \,\mathrm{d}S\,\mathrm{d}t \\
+ &\int_{\mathcal{I}_n}\int_{\mathcal{F}_0} [\![\mathbf{H}_h]\!]_T \cdot \{\pi_{\widetilde{T}}\mathbf{w}_E - \mathbf{w}_E\} \,\mathrm{d}S\,\mathrm{d}t\Bigg) \\
- \frac{1}{2}\Bigg(&\int_{\mathcal{I}_n}\int_{\mathcal{F}_0} \{\mathbf{E}_h\} \cdot [\![\pi_{\widetilde{T}}\mathbf{w}_H - \mathbf{w}_H]\!]_T \,\mathrm{d}S\,\mathrm{d}t + \int_{\mathcal{I}_n}\int_{\mathcal{F}_0} [\![\mathbf{E}_h]\!]_T \cdot \{\pi_{\widetilde{T}}\mathbf{w}_H - \mathbf{w}_H\} \,\mathrm{d}S\,\mathrm{d}t\Bigg),
\end{aligned} \tag{3.13}$$

and thus obtain the stabilized discrete problem

$$\begin{aligned}
&\text{Find } \mathbf{u}_h^n \in \mathbf{V}_h^n \\
&C_h^n(\mathbf{u}_h, \mathbf{w}) + D_h^n(\mathbf{u}_h, \pi_{\widetilde{T}}\mathbf{w}) + S_h^n(\mathbf{u}_h, \mathbf{w}) = L_h^n(\mathbf{w}) \;\forall\; \mathbf{w} \in \mathbf{W}_h^n \\
&\mathbf{u}_h^n(t_n) = \mathbf{u}_h^{n-1}(t_n).
\end{aligned} \tag{3.14}$$

Note, that for simplicity we again require assumption 3.1.3 to hold. It should be further noted, that under assumption 3.1.2 there holds $S_h^n(\mathbf{u}_h, \mathbf{w}) = 0$ such that in this case (3.14) reduces to problem (3.9) of the previous section.
Proceeding similarly as in the previous section, instead of the Galerkin orthogonality (3.12) we observe, that we commit a “variational crime”

$$B_h^n(\mathbf{u} - \mathbf{u}_h, \mathbf{w}) = S_h^n(\mathbf{u}, \mathbf{w}) \;\forall\; \mathbf{w} \in \mathbf{W}_h^n. \tag{3.15}$$

However, for the inconsistent term on the right-hand-side of (3.15) there holds by tangential continuity of $\mathbf{E}, \mathbf{H}$

$$
\begin{aligned}
S_h^n(\mathbf{u},\mathbf{w}) = \frac{1}{2}\bigg(&\int_{\mathcal{I}_n}\int_{\mathcal{F}_0} \{\mathbf{H}\}\cdot \llbracket \pi_{\tilde{T}}\mathbf{w}_E - \mathbf{w}_E \rrbracket_T \,\mathrm{d}S\,\mathrm{d}t + \int_{\mathcal{I}_n}\int_{\mathcal{F}_0} \llbracket \mathbf{H} \rrbracket_T \cdot \{\pi_{\tilde{T}}\mathbf{w}_E - \mathbf{w}_E\}\,\mathrm{d}S\,\mathrm{d}t\bigg) \\
-\frac{1}{2}\bigg(&\int_{\mathcal{I}_n}\int_{\mathcal{F}_0} \{\mathbf{E}\}\cdot \llbracket \pi_{\tilde{T}}\mathbf{w}_H - \mathbf{w}_H \rrbracket_T \,\mathrm{d}S\,\mathrm{d}t + \int_{\mathcal{I}_n}\int_{\mathcal{F}_0} \llbracket \mathbf{E} \rrbracket_T \cdot \{\pi_{\tilde{T}}\mathbf{w}_H - \mathbf{w}_H\}\,\mathrm{d}S\,\mathrm{d}t\bigg) \\
= \frac{1}{2}\bigg(&\int_{\mathcal{I}_n}\int_{\mathcal{F}_0} (\pi_{\tilde{T}}\mathbf{H} - \mathbf{H})\cdot \llbracket \mathbf{w}_E \rrbracket_T \,\mathrm{d}S\,\mathrm{d}t - \int_{\mathcal{I}_n}\int_{\mathcal{F}_0} (\pi_{\tilde{T}}\mathbf{E} - \mathbf{E})\cdot \llbracket \mathbf{w}_H \rrbracket_T \,\mathrm{d}S\,\mathrm{d}t\bigg),
\end{aligned}
$$

which can be estimated face-by-face with estimates for the L^2-projection $\pi_{\tilde{T}}$. Thus in the limit $\Delta t \to 0$ we obtain $S_h(\mathbf{u},\mathbf{w}) = 0$. This also holds for sufficiently smooth solutions $\mathbf{u}$ in the limit $p_t \to \infty$.

3.2 *a priori* Error Analysis

In this section, the convergence analysis of the space-time discontinuous Galerkin method is carried out for discretizations with global hp-refinement with respect to time. The analysis extends results for an h-version hybrid discontinuous Galerkin (HDG) discretization for the wave equation [20] and results for semi-discretizations for Maxwell's equations (see. [11, 18]) to the presented hp-version space-time DG method. It yields error-bounds in the $\|\cdot\|_{L^\infty(0,T;\mathbf{L}^2(\Omega))}$- and $\|\cdot\|_{L^2(0,T;\mathbf{L}^2(\Omega))}$-norms. Essentially, the analysis is valid for 1-irregular meshes consisting of affine hexahedra and isotropic spatial polynomial degrees $p = p_x = p_y = p_z$, in order to be able to use standard approximation results. It is noteworthy, that the analysis also applies to tetrahedral meshes. However, the extension to non-affine elements is not straightforward (see for hexahedral elements [48]). Furthermore, the stability analysis in the $L^2(\Omega)$-norm is also given for the general case of discretizations with local refinement in time.

The error analysis can be outlined as follows. First, as usual [10], the error is decomposed in approximation- and discrete errors

$$
\begin{aligned}
\|\mathbf{u}-\mathbf{u}_h\|_{L^2(\mathcal{I};\mathbf{L}^2(\Omega))} = \|\boldsymbol{\eta}+\boldsymbol{\xi}\|_{L^2(\mathcal{I};\mathbf{L}^2(\Omega))} \le \|\boldsymbol{\eta}\|_{L^2(\mathcal{I};\mathbf{L}^2(\Omega))} + \|\boldsymbol{\xi}\|_{L^2(\mathcal{I};\mathbf{L}^2(\Omega))} \qquad (3.16) \\
\boldsymbol{\eta} = \mathbf{u} - I_h\mathbf{u},\ \boldsymbol{\xi} = I_h\mathbf{u} - \mathbf{u}_h,
\end{aligned}
$$

where $I_h : \mathbf{V} \to \mathbf{V}_h$ denotes a suitable space-time interpolation operator, the choice of which is detailed in section 3.2.3.

The first term on the right-hand side of (3.16) is estimated using approximation error estimates. An estimate for the second term is obtained by using (3.12) which yields

$$B_h^n(\boldsymbol{\xi}, \mathbf{w}) = B_h^n(-\boldsymbol{\eta}, \mathbf{w}) \; \forall \; \mathbf{w} \in \mathbf{W}_h^n \; \forall \; n. \tag{3.17}$$

Then, a stability estimate of the form

$$\beta \|\boldsymbol{\xi}\|_{L^2(\mathcal{I}_n;\mathbf{L}^2(\Omega))} \leq \sup_{\mathbf{V}\in\mathbf{W}_h\mathbf{V}\neq 0} \frac{|B_h(\xi, \mathbf{w})|}{\|\mathbf{V}\|_{L^2(\mathcal{I}_n;\mathbf{L}^2(\Omega))}}, \; \beta > 0 \tag{3.18}$$

is shown to hold in section 3.2.1. The right-hand side of (3.18) is then estimated in section 3.2.3. Both results are then combined to obtain the desired bound on the discrete error.

3.2.1 Stability: Discretizations with Global hp-Refinement in Time

For discretizations fulfilling assumptions 3.1.2 and 3.1.3, in this section we provide stability estimates in the $L^2(\Omega)$- and $L^2(\mathcal{I};\mathbf{L}^2(\Omega))$-norms, which were established in [40]. To this end, we apply techniques similar to those from [20], where a h-version HDG-method for the wave equation is analyzed.
The problem under consideration is

$$\begin{aligned} &\text{Find } \mathbf{u}_h^n \in \mathbf{V}_h^n \quad \text{such that} \\ &B_h^n(\mathbf{u}_h, \mathbf{w}) = L_h^n(\mathbf{w}) \; \forall \; \mathbf{w} \; \in \mathbf{W}_h^n \\ &\mathbf{u}_h^n(t_n) = \mathbf{u}_h^{n-1}(t_n). \end{aligned} \tag{3.19}$$

We extent the $L^2(\Omega)$-stability result in the next section to discretizations with local refinement in time, i.e. the case when 3.1.2 does not hold. The extension to variable spatial discretizations, when assumption 3.1.3 does not hold, is treated in section 3.2.5.

Stability: $L^2(\Omega)$-Norm

We establish stability of the method by demonstrating that a discrete version of Poynting's theorem (2.7) holds. More precisely, we show that the discrete electromagnetic energy

$$\mathcal{W}_h(t) = \frac{1}{2} \int_\Omega (\varepsilon \mathbf{E}_h \cdot \mathbf{E}_h + \mu \mathbf{H}_h \cdot \mathbf{H}_h) \, \mathrm{d}x, \tag{3.20}$$

is constant up to a contribution of the source-terms and the dissipative stabilization term. Moreover, for the choice of central fluxes ($\alpha_E = \alpha_H = 0$) and $\mathbf{g} = 0, \mathbf{J} = 0$, we obtain conservation of the discrete electromagnetic energy $\mathcal{W}_h(t_n)$.

Theorem 3.2.1. *Under assumptions 3.1.1 and 3.1.2, there holds*

$$
\begin{aligned}
\mathcal{W}_h(t_{n+1}) - \mathcal{W}_h(t_n) = & \int_{\mathcal{I}_n}\int_{\Omega} \mathbf{J}\cdot\pi_{\scriptscriptstyle T}\mathbf{E}_h \,\mathrm{d}x\,\mathrm{d}t - \int_{\mathcal{I}_n}\int_{\mathcal{F}_b} \mathbf{n}\times\mathbf{g}\cdot\pi_{\scriptscriptstyle T}\mathbf{H}_h \,\mathrm{d}S\,\mathrm{d}t \\
& - \int_{\mathcal{I}_n}\int_{\mathcal{F}_0} \alpha_E [\![\pi_{\scriptscriptstyle T}\mathbf{E}_h]\!]_T\cdot[\![\pi_{\scriptscriptstyle T}\mathbf{E}_h]\!]_T \,\mathrm{d}S\,\mathrm{d}t - \int_{\mathcal{I}_n}\int_{\mathcal{F}_b} \alpha_E [\![\pi_{\scriptscriptstyle T}\mathbf{E}_h - \mathbf{g}]\!]_T\cdot[\![\pi_{\scriptscriptstyle T}\mathbf{E}_h]\!]_T \,\mathrm{d}S\,\mathrm{d}t \\
& - \int_{\mathcal{I}_n}\int_{\mathcal{F}_0} \alpha_H [\![\pi_{\scriptscriptstyle T}\mathbf{H}_h]\!]_T\cdot[\![\pi_{\scriptscriptstyle T}\mathbf{H}_h]\!]_T \,\mathrm{d}S\,\mathrm{d}t
\end{aligned}
\tag{3.21}
$$

Proof. By $\pi_T : V_h \rightarrow W_h$, we denote the L^2-orthogonal projection operator from the trial-space V_h onto the test-space W_h. Since the spatial parts of V_h and W_h are identical, the projection π_T reduces to a projection with respect to time only.
By setting $\mathbf{w}_E = \pi_{\scriptscriptstyle T}\mathbf{E}_h, \mathbf{w}_H = \pi_{\scriptscriptstyle T}\mathbf{H}_h$ in (3.9) we obtain

$$
\begin{aligned}
& \int_{\mathcal{I}_n}\int_{\Omega} \varepsilon\partial_t\mathbf{E}_h\cdot\pi_{\scriptscriptstyle T}\mathbf{E}_h \,\mathrm{d}x\,\mathrm{d}t + \int_{\mathcal{I}_n}\int_{\Omega} \mu\partial_t\mathbf{H}_h\cdot\pi_{\scriptscriptstyle T}\mathbf{H}_h \,\mathrm{d}x\,\mathrm{d}t \\
& - \int_{\mathcal{I}_n}\int_{\Omega} \mathbf{H}_h\cdot\nabla_h\times\pi_{\scriptscriptstyle T}\mathbf{E}_h \,\mathrm{d}x\,\mathrm{d}t + \int_{\mathcal{I}_n}\int_{\Omega} \nabla_h\times\mathbf{E}_h\cdot\pi_{\scriptscriptstyle T}\mathbf{H}_h \,\mathrm{d}x\,\mathrm{d}t \\
& + \int_{\mathcal{I}_n}\int_{\mathcal{F}_0\cup\mathcal{F}_b} \{\mathbf{H}_h\}\cdot[\![\pi_{\scriptscriptstyle T}\mathbf{E}_h]\!]_T \,\mathrm{d}S\,\mathrm{d}t - \int_{\mathcal{I}_n}\int_{\mathcal{F}_0\cup\mathcal{F}_b} [\![\mathbf{E}_h]\!]_T\cdot\{\pi_{\scriptscriptstyle T}\mathbf{H}_h\} \,\mathrm{d}S\,\mathrm{d}t \\
& + \int_{\mathcal{I}_n}\int_{\mathcal{F}} \alpha_E[\![\mathbf{E}_h]\!]_T\cdot[\![\pi_{\scriptscriptstyle T}\mathbf{E}_h]\!]_T \,\mathrm{d}S\,\mathrm{d}t + \int_{\mathcal{I}_n}\int_{\mathcal{F}_0} \alpha_H[\![\mathbf{H}_h]\!]_T\cdot[\![\pi_{\scriptscriptstyle T}\mathbf{H}_h]\!]_T \,\mathrm{d}S\,\mathrm{d}t \\
& = \int_{\mathcal{I}_n}\int_{\Omega} \mathbf{J}\cdot\pi_{\scriptscriptstyle T}\mathbf{E}_h \,\mathrm{d}x\,\mathrm{d}t - \int_{\mathcal{I}_n}\int_{\mathcal{F}_b} \mathbf{n}\times\mathbf{g}\cdot\pi_{\scriptscriptstyle T}\mathbf{H}_h \,\mathrm{d}S\,\mathrm{d}t + \int_{\mathcal{I}_n}\int_{\mathcal{F}_b} [\![\mathbf{g}]\!]_T\cdot[\![\pi_{\scriptscriptstyle T}\mathbf{E}_h]\!]_T \,\mathrm{d}S\,\mathrm{d}t
\end{aligned}
\tag{3.22}
$$

Noting that $\partial_t\mathbf{E}_h \in W_h$, and integrating by parts, the first term in (3.22) becomes

$$
\begin{aligned}
\int_{\mathcal{I}_n}\int_{\Omega} \varepsilon\partial_t\mathbf{E}_h\cdot\pi_{\scriptscriptstyle T}\mathbf{E}_h \,\mathrm{d}x\,\mathrm{d}t &= \int_{\mathcal{I}_n}\int_{\Omega} \varepsilon\partial_t\mathbf{E}_h\cdot\mathbf{E}_h \,\mathrm{d}x\,\mathrm{d}t \\
&= \frac{1}{2}\int_{\Omega} \varepsilon\mathbf{E}_h(t_{k+1})\cdot\mathbf{E}_h(t_{k+1}) \,\mathrm{d}x - \frac{1}{2}\int_{\Omega} \varepsilon\mathbf{E}_h(t_k)\cdot\mathbf{E}_h(t_k) \,\mathrm{d}x.
\end{aligned}
$$

Proceeding similarely with the second term in (3.22),

$$\int_{\mathcal{I}_n}\int_\Omega \varepsilon\partial_t \mathbf{E}_h\cdot\pi_T\mathbf{E}_h\,\mathrm{d}x\,\mathrm{d}t+\int_{\mathcal{I}_n}\int_\Omega \mu\partial_t \mathbf{H}_h\cdot\pi_T\mathbf{H}_h\,\mathrm{d}x\,\mathrm{d}t=\mathcal{W}_h(t_{n+1})-\mathcal{W}_h(t_n). \tag{3.23}$$

Noting that π_T is an orthogonal projection and thus self-adjoint, we get for the third term

$$-\int_{\mathcal{I}_n}\int_\Omega \mathbf{H}_h\cdot\nabla_h\times\pi_T\mathbf{E}_h\,\mathrm{d}x\,\mathrm{d}t=-\int_{\mathcal{I}_n}\int_\Omega \pi_T\mathbf{H}_h\cdot\nabla_h\times\mathbf{E}_h\,\mathrm{d}x\,\mathrm{d}t,$$

such that the sum of the third and fourth terms is zero.
For an interior face $f=\partial K^1\cap\partial K^2\in\mathcal{F}_0$, we expand the mesh-dependent terms as

$$\begin{aligned}
&+\int_{\mathcal{I}_n}\int_f \{\mathbf{H}_h\}\cdot[\![\pi_T\mathbf{E}_h]\!]_T\,\mathrm{d}S\,\mathrm{d}t-\int_{\mathcal{I}_n}\int_f [\![\mathbf{E}_h]\!]_T\cdot\{\pi_T\mathbf{H}_h\}\,\mathrm{d}S\,\mathrm{d}t\\
&=\frac{1}{2}\int_{\mathcal{I}_n}\int_f \mathbf{H}_h^1\cdot\mathbf{n}^1\times\pi^1\mathbf{E}^1\,\mathrm{d}S\,\mathrm{d}t+\frac{1}{2}\int_{\mathcal{I}_n}\int_f \mathbf{H}_h^2\cdot\mathbf{n}^1\times\pi^1\mathbf{E}_h^1\,\mathrm{d}S\,\mathrm{d}t\\
&+\frac{1}{2}\int_{\mathcal{I}_n}\int_f \mathbf{H}_h^1\cdot\mathbf{n}^2\times\pi^2\mathbf{E}^2\,\mathrm{d}S\,\mathrm{d}t+\frac{1}{2}\int_{\mathcal{I}_n}\int_f \mathbf{H}_h^2\cdot\mathbf{n}^2\times\pi^2\mathbf{E}^2\,\mathrm{d}S\,\mathrm{d}t\\
&-\frac{1}{2}\int_{\mathcal{I}_n}\int_f \pi^1\mathbf{H}^1\cdot\mathbf{n}^1\times\mathbf{E}_h^1\,\mathrm{d}S\,\mathrm{d}t-\frac{1}{2}\int_{\mathcal{I}_n}\int_f \pi^1\mathbf{H}^1\cdot\mathbf{n}^2\times\mathbf{E}_h^2\,\mathrm{d}S\,\mathrm{d}t\\
&-\frac{1}{2}\int_{\mathcal{I}_n}\int_f \pi^2\mathbf{H}^2\cdot\mathbf{n}^1\times\mathbf{E}_h^1\,\mathrm{d}S\,\mathrm{d}t-\frac{1}{2}\int_{\mathcal{I}_n}\int_f \pi^2\mathbf{H}^2\cdot\mathbf{n}^2\times\mathbf{E}_h^2\,\mathrm{d}S\,\mathrm{d}t \qquad (3.24)\\
&=T_1+T_2+T_3+T_4+T_5+T_6+T_7+T_8.
\end{aligned}$$

Here, π^1 and π^2 are the restrictions of the projector π_T to the local test spaces W_{h,K^1} and W_{h,K^2} from (3.4). For the non-coupling terms in (3.24), e.g. T_1 and T_5, we obtain by the symmetry of π^1

$$T_1=\frac{1}{2}\int_{\mathcal{I}_n}\int_f \mathbf{H}_h^1\cdot\mathbf{n}^1\times\pi^1\mathbf{E}^1\,\mathrm{d}S\,\mathrm{d}t=\frac{1}{2}\int_{\mathcal{I}_n}\int_f \pi^1\mathbf{H}^1\cdot\mathbf{n}^1\times\mathbf{E}_h^1\,\mathrm{d}S\,\mathrm{d}t=-T_5,$$

and thus $T_1+T_5=0$. By the same argument we get $T_4+T_8=0$. Considering the terms with neighbor-coupling in (3.24), we obtain e.g.

$$\begin{aligned}
T_2=\frac{1}{2}\int_{\mathcal{I}_n}\int_f \mathbf{H}_h^2\cdot\mathbf{n}^1\times\pi^1\mathbf{E}^1\,\mathrm{d}S\,\mathrm{d}t&=\frac{1}{2}\int_{\mathcal{I}_n}\int_f \pi^1\mathbf{H}_h^2\cdot\mathbf{n}^1\times\mathbf{E}_h^1\,\mathrm{d}S\,\mathrm{d}t\\
&=\frac{1}{2}\int_{\mathcal{I}_n}\int_f \pi^2\mathbf{H}_h^2\cdot\mathbf{n}^1\times\mathbf{E}_h^1\,\mathrm{d}S\,\mathrm{d}t=-T_7,
\end{aligned}$$

where we have used $\pi^1\mathbf{H}_h^2 = \pi^2\mathbf{H}_h^2$. Note, that this only holds by assumption 3.1.2, which assures that the temporal parts $T_{K^1}(\mathcal{I}_n)$ and $T_{K^2}(\mathcal{I}_n)$ of the local test spaces W_{h,K^1} and W_{h,K^2} are identical. Thus, we obtain $T_2 + T_7 = 0$ and analogously $T_3 + T_6 = 0$.
Finally, we remark that mesh-dependent boundary terms have the same structure as the non-coupling terms in (3.24) and obtain the desired result. ☐

Stability: $L^2(\mathcal{I}; L^2(\Omega))$-Norm

Now, we demonstrate stability in the $L^2(\mathcal{I};\mathbf{L}^2(\Omega))$-norm. To this end, we need some recurrence relations for the Legendre-polynomials $L_i(\xi)$, see [1].

$$\begin{aligned}(i+1)L_{i+1}(\xi) &= (2i+1)\xi L_i(\xi) - i\text{Ł}_{i-1}(\xi)\\ L_i'(\xi) &= 2L_{i-1}(\xi)/\|L_{i-1}\|^2_{L^2([-1,1])} + 2L_{i-3}(\xi)/\|L_{i-3}\|^2_{L^2([-1,1])} + \dots\\ \xi L_{i+1}' &= (i+1)L_{i+1}(\xi) + iL_{i-1}(\xi) + (i-1)L_{i-1}(\xi) + (i-2)L_{i-3}(\xi)\dots\end{aligned} \tag{3.25}$$

Lemma 3.2.1. *Under assumption 3.1.1 there holds*

$$\begin{aligned}\frac{1}{2\Delta t}\|\varepsilon^{\frac{1}{2}}\mathbf{E}_h\|^2_{L^2(\mathcal{I}_n;\mathbf{L}^2(\Omega))} + \frac{1}{2\Delta t}\|\mu^{\frac{1}{2}}\mathbf{H}_h\|^2_{L^2(\mathcal{I}_n;\mathbf{L}^2(\Omega))} &\le \int_{\mathcal{I}_n}\int_\Omega \varepsilon\partial_t\mathbf{E}_h\cdot\pi_T(\tau(t)\pi_T\mathbf{E}_h)\,\mathrm{d}x\,\mathrm{d}t\\ &+ \int_{\mathcal{I}_n}\int_\Omega \mu\partial_t\mathbf{H}_h\cdot\pi_T(\tau(t)\pi_T\mathbf{H}_h)\,\mathrm{d}x\,\mathrm{d}t + \mathcal{W}_h(t_k),\quad \tau(t) = \frac{(t_{k+1}-t)}{\Delta t}\end{aligned}$$

Proof. Noting that π_T is an orthogonal projection and $\partial_t\mathbf{E}_h \in W_h$, integration by parts with respect to time yields, see also [68],

$$\int_{\mathcal{I}_n}\int_K \varepsilon\partial_t\mathbf{E}_h\cdot\pi_T(\tau(t)\mathbf{E}_h)\,\mathrm{d}x\,\mathrm{d}t = \frac{1}{2\Delta t}\|\varepsilon^{\frac{1}{2}}\mathbf{E}_h\|^2_{L^2(\mathcal{I}_n;\mathbf{L}^2(K))} - \frac{1}{2}\|\varepsilon^{\frac{1}{2}}\mathbf{E}_h(t_k)\|^2_{\mathbf{L}^2(K)}.$$

Further, we rewrite

$$\begin{aligned}\int_{\mathcal{I}_n}\int_K \varepsilon\partial_t\mathbf{E}_h\cdot\pi_T(\tau(t)\mathbf{E}_h)\,\mathrm{d}x\,\mathrm{d}t &= \int_{\mathcal{I}_n}\int_K \varepsilon\partial_t\mathbf{E}_h\cdot\tau(t)(\mathbf{E}_h - \pi_T\mathbf{E}_h)\,\mathrm{d}x\,\mathrm{d}t\\ &+ \int_{\mathcal{I}_n}\int_K \varepsilon\partial_t\mathbf{E}_h\cdot\tau(t)\pi_T\mathbf{E}_h\,\mathrm{d}x\,\mathrm{d}t.\end{aligned} \tag{3.26}$$

Now we demonstrate, that there holds

$$\int_{\mathcal{I}_n}\int_K \varepsilon\partial_t \mathbf{E}_h\cdot\tau(t)(\mathbf{E}_h-\pi_{\mathcal{T}}\mathbf{E}_h)\,\mathrm{d}x\,\mathrm{d}t\le 0.$$

Using the space-time tensor product structure of the local finite element spaces, we rewrite the discrete solution and the projection error as

$$\begin{aligned}\mathbf{E}_h &= \sum_{i=0}^{p_t}\sum_{k=1}^{N_s} L_i(\xi)\varphi_k(x,y,z)e_{ik}\\ \mathbf{E}_h-\pi_{\mathcal{T}}\mathbf{E}_h &= \sum_{k=1}^{N_s} L_{p_t}(\xi)\varphi_k(x,y,z)e_{p_t\,k}\end{aligned}\tag{3.27}$$

with $\xi = 2(t-t_k)/\Delta t - 1$, $N_s = 3(p_x+1)(p_y+1)(p_z+1)$ and the expansion coefficients e_{ik}.

By employing again the projection property, inserting (3.27) and then applying the second recurrence relation from (3.25), we get

$$\begin{aligned}&\int_{I_n^K}\int_K \varepsilon\partial_t \mathbf{E}_h\cdot\tau(t)(\mathbf{E}_h-\pi_{\mathcal{T}}\mathbf{E}_h)\,\mathrm{d}x\,\mathrm{d}t = -\frac{\varepsilon}{\Delta t}\int_{I_n^K}\int_K \partial_t \mathbf{E}_h\cdot t(\mathbf{E}_h-\pi_{\mathcal{T}}\mathbf{E}_h)\,\mathrm{d}x\,\mathrm{d}t\\ &= -\frac{\varepsilon}{\Delta t}\sum_{i=1}^{p_t}\sum_{j=1}^{N_s}\sum_{l=1}^{N_s}\int\limits_{-1}^{1}(t_k+\Delta t(1+\xi)/2)L_i'(\xi)L_{p_t}(\xi)\,\mathrm{d}\xi\\ &\times\int_K \varphi_j(x,y,z)\cdot\varphi_l(x,y,z)\,\mathrm{d}x e_{ij}e_{p_t\,l}\\ &= -\frac{\varepsilon}{\Delta t}\sum_{i=1}^{p_t}\int\limits_{-1}^{1}\frac{\Delta t}{2}\xi L_i'(\xi)L_{p_t+1}(\xi)\,\mathrm{d}\xi\sum_{j=1}^{N_s}\sum_{l=1}^{N_s}\int_K \varphi_j(x,y,z)\cdot\varphi_l(x,y,z)\,\mathrm{d}x e_{ij}e_{p_t\,l}.\end{aligned}$$

Now, we can apply the third recurrence relation from (3.25) and then use the orthogonality of the Legendre polynomials to get

$$\begin{aligned}&\int_{I_n^K}\int_K \varepsilon\partial_t \mathbf{E}_h\cdot\tau(t)(\mathbf{E}_h-\pi_{\mathcal{T}}\mathbf{E}_h)\,\mathrm{d}x\,\mathrm{d}t\\ &= -(\varepsilon/2)\int\limits_{-1}^{1} L_{p_t}(\xi)^2\,\mathrm{d}\xi\sum_{j=1}^{N_s}\sum_{l=1}^{N_s}\int_K \varphi_j(x,y,z)\cdot\varphi_l(x,y,z)\,\mathrm{d}x\, e_{p_t+1\,j}e_{p_t+1\,l}\le 0.\end{aligned}$$

□

Employing lemma 3.2.1 and similar arguments as in the proof of theorem 3.2.1, we can show that the following stability estimates hold for each time-slab $\mathcal{I}_n \times \Omega$. The second estimate (3.29) follows from (3.28) and implies unique solvability of the discrete problem.

Theorem 3.2.2. *Under assumptions 3.1.1 and 3.1.2 there holds*

$$\begin{aligned} &\|\varepsilon^{\frac{1}{2}}\mathbf{E}_h\|^2_{L^2(\mathcal{I}_n;\mathbf{L}^2(\Omega))} + \|\mu^{\frac{1}{2}}\mathbf{H}_h\|^2_{L^2(\mathcal{I}_n;\mathbf{L}^2(\Omega))} \\ +&\|(\alpha_E\tau)^{\frac{1}{2}}[\![\pi_T\mathbf{E}_h]\!]_T\|^2_{L_2(\mathcal{I}_n;\mathbf{L}^2(\mathcal{F}))} + \|(\alpha_H\tau)^{\frac{1}{2}}[\![\pi_T\mathbf{H}_h]\!]_T\|^2_{L_2(\mathcal{I}_n;\mathbf{L}^2(\mathcal{F}_0))} \\ &\leq 2\Delta t B_h^n(\mathbf{u}_h, \pi_T(\tau\pi_T\mathbf{u}_h)) + 2\Delta t\mathcal{W}_h(t_n) \end{aligned} \tag{3.28}$$

and for $\mathcal{W}_h(t_n) = 0$ *there holds*

$$\beta\|\mathbf{u}_h\|_{L^2(\mathcal{I}_n;\mathbf{L}^2(\Omega))} \leq \sup_{\mathbf{w}\in\mathbf{W}_h\mathbf{w}\neq 0} \frac{|B_h(\mathbf{u}_h,\mathbf{w})|}{\|\mathbf{V}\|_{L^2(\mathcal{I}_n;\mathbf{L}^2(\Omega))}}\ \beta = \frac{1}{2\Delta t}. \tag{3.29}$$

Proof. Choosing $\widetilde{\mathbf{w}} = \pi_T(\tau(t)\pi_T\mathbf{u}_h)$ yields

$$\begin{aligned} B_h^n(\mathbf{u}_h,\widetilde{\mathbf{w}}) &= \int_{\mathcal{I}_n}\int_\Omega \varepsilon\partial_t\mathbf{E}_h\cdot\pi_T(\tau(t)\pi_T\mathbf{E}_h)\,\mathrm{d}x\,\mathrm{d}t + \int_{\mathcal{I}_n}\int_\Omega \mu\partial_t\mathbf{H}_h\cdot\pi_T(\tau(t)\pi_T\mathbf{H}_h)\,\mathrm{d}x\,\mathrm{d}t \\ &+ \int_{\mathcal{I}_n}\int_{\mathcal{F}} \alpha_E[\![\mathbf{E}_h]\!]_T\cdot[\![\pi_T(\tau(t)\pi_T\mathbf{E}_h)]\!]_T\,\mathrm{d}S\,\mathrm{d}t + \int_{\mathcal{I}_n}\int_{\mathcal{F}_0} \alpha_H[\![\mathbf{H}_h]\!]_T\cdot[\![\pi_T(\tau(t)\pi_T\mathbf{H}_h)]\!]_T\,\mathrm{d}S\,\mathrm{d}t \end{aligned}$$

where we have followed the line of arguments of the proof of Theorem 3.2.1. Applying lemma 3.2.1 yields (3.28). The second estimate follows for $\mathcal{W}_h(t_n) = 0$ with $\|\pi_T\| \leq 1$ and $1 \geq \tau(t) \geq 0$ on $\mathcal{I}_n$. ☐

Now, we prove the continuous dependence of the solution on the initial-data and the source-terms. We denote the dual norm on the test space by

$$\|\ell\|_{W_h'} := \sup_{\mathbf{w}\in W_h,\mathbf{w}\neq 0} \frac{|\ell(\mathbf{w})|}{\|\mathbf{w}\|_{L^2(\mathcal{I}_n;\mathbf{L}^2(\Omega))}}.$$

Lemma 3.2.2. *Under assumptions 3.1.1 and 3.1.2 there holds*

$$\begin{aligned} &\|\varepsilon^{\frac{1}{2}}\mathbf{E}_h\|^2_{L^2(\mathcal{I}_n;\mathbf{L}^2(\Omega))} + \|\mu^{\frac{1}{2}}\mathbf{H}_h\|^2_{L^2(\mathcal{I}_n;\mathbf{L}^2(\Omega))} \\ +&\|(\alpha_E\tau)^{\frac{1}{2}}[\![\pi_T\mathbf{E}_h]\!]_T\|^2_{L_2(\mathcal{I}_n;\mathbf{L}^2(\mathcal{F}))} + \|(\alpha_H\tau)^{\frac{1}{2}}[\![\pi_T\mathbf{H}_h]\!]_T\|^2_{L_2(\mathcal{I}_n;\mathbf{L}^2(\mathcal{F}_0))} \\ &\leq 4\Delta t^2\left(\underline{\varepsilon}^{-1}\|\ell_E\|^2_{W_h'} + \underline{\mu}^{-1}\|\ell_H\|^2_{W_h'}\right) + 4\Delta t\mathcal{W}_h(t_n) \end{aligned} \tag{3.30}$$

Proof. Using (3.28) with (3.9), applying the Cauchy-Schwarz inequality and the arithmetic-geometric-mean inequality yields

$$
\begin{aligned}
&\frac{1}{2\Delta t}\left(\|\varepsilon^{\frac{1}{2}}\mathbf{E}_h\|^2_{L^2(\mathcal{I}_n;\mathbf{L}^2(\Omega))} + \|\varepsilon^{\frac{1}{2}}\mathbf{H}_h\|^2_{L^2(\mathcal{I}_n;\mathbf{L}^2(\Omega))}\right)\\
&\leq \ell_E(\pi_T(\tau(t)\pi_T\mathbf{E}_h)) + \ell_H(\pi_T(\tau(t)\pi_T\mathbf{H}_h)) + \mathcal{W}_h(t_k)\\
&\leq \|\ell_E\|_{W_h'}\|\pi_T(\tau(t)\pi_T\mathbf{E}_h)\|_{L^2(\mathcal{I}_n;\mathbf{L}^2(\Omega))} + \|\ell_H\|_{W_h'}\|\pi_T(\tau(t)\pi_T\mathbf{H}_h)\|_{L^2(\mathcal{I}_n;\mathbf{L}^2(\Omega))} + \mathcal{W}_h(t_k)\\
&\leq \Delta t\left(\underline{\varepsilon}^{-1}\|\ell_E\|^2_{W_h'} + \underline{\mu}^{-1}\|\ell_H\|^2_{W_h'}\right) + \mathcal{W}_h(t_k)\\
&+ \frac{\varepsilon}{4\Delta t}\|\pi_T(\tau(t)\pi_T\mathbf{E}_h)\|^2_{L^2(\mathcal{I}_n;\mathbf{L}^2(\Omega))} + \frac{\mu}{4\Delta t}\|\pi_T(\tau(t)\pi_T\mathbf{H}_h)\|^2_{L^2(\mathcal{I}_n;\mathbf{L}^2(\Omega))}\\
&\leq \Delta t\left(\underline{\varepsilon}^{-1}\|\ell_E\|^2_{W_h'} + \underline{\mu}^{-1}\|\ell_H\|^2_{W_h'}\right) + \mathcal{W}_h(t_k)\\
&+ \frac{1}{4\Delta t}\left(\|\varepsilon\pi_T(\tau(t)\pi_T\mathbf{E}_h)\|^2_{L^2(\mathcal{I}_n;\mathbf{L}^2(\Omega))} + \|\mu\pi_T(\tau(t)\pi_T\mathbf{H}_h)\|^2_{L^2(\mathcal{I}_n;\mathbf{L}^2(\Omega))}\right).
\end{aligned}
$$

Using, $\|\pi_T\| \leq 1$ and $1 \geq \tau(t) \geq 0$ on $\mathcal{I}_n$, yields the result. ☐

We are now ready to obtain a global stability bound, by combining the local bounds from theorem 3.2.1 and lemma 3.2.2. A particularly useful property of the obtained bound are the explicitly known constants. This allows for obtaining a guaranteed bound on the iteration error in section 3.3, such that the linear systems arising from the implicit discretization can be solved inexactly without compromising the overall accuracy of the solution.

Theorem 3.2.3. *Under assumptions 3.1.1 and 3.1.2 there holds*

$$
\mathcal{W}_h(t_n) \leq 2\mathcal{W}_h(t_1) + 2\sum_{n=1}^{N}\left(\left(\frac{2t_n}{\underline{\varepsilon}} + \frac{\Delta t^2}{2t_n\underline{\varepsilon}}\right)\|\ell_E^n\|^2_{W_h'} + \left(\frac{2t_n}{\underline{\mu}} + \frac{\Delta t^2}{2t_n\underline{\mu}}\right)\|\ell_H^n\|^2_{W_h'}\right) \tag{3.31}
$$

Proof. The proof follows along the lines of [20] Corollary 1.
We set $n_{max} = \arg\max_n \mathcal{W}_h(t_n)$. We obtain using Theorem 3.2.1 and the Cauchy-Schwarz inequality, the arithmetic geometric mean inequality and (3.30).

$$
\begin{aligned}
&\max_n \mathcal{W}_h(t_n) \leq \mathcal{W}_h(t_1) + \sum_{n=1}^{n_{max}}\left(\|\ell_E\|_{W_h'}\|\mathbf{E}_h\|_{L^2(\mathcal{I}_n;\mathbf{L}^2(\Omega))} + \|\ell_H\|_{W_h'}\|\mathbf{H}_h\|_{L^2(\mathcal{I}_n;\mathbf{L}^2(\Omega))}\right)\\
&\leq \mathcal{W}_h(t_1) + \sum_{n=1}^{n_{max}}\left(\frac{\delta}{\underline{\varepsilon}}\|\ell_E\|^2_{W_h'} + \frac{\delta}{\underline{\mu}}\|\ell_H\|^2_{W_h'} + \frac{\varepsilon}{4\delta}\|\mathbf{E}_h\|^2_{L^2(\mathcal{I}_n;\mathbf{L}^2(\Omega))} + \frac{\mu}{4\delta}\|\mathbf{H}_h\|^2_{L^2(\mathcal{I}_n;\mathbf{L}^2(\Omega))}\right)\\
&\leq \mathcal{W}_h(t_1) + \sum_{n=1}^{n_{max}}\left(\left(\frac{\delta}{\underline{\varepsilon}} + \frac{\Delta t^2}{\underline{\varepsilon}\delta}\right)\|\ell_E\|^2_{W_h'} + \left(\frac{\delta}{\underline{\mu}} + \frac{\Delta t^2}{\underline{\mu}\delta}\right)\|\ell_H\|^2_{W_h'} + \frac{\Delta t}{\delta}\mathcal{W}_h(t_n)\right).
\end{aligned}
$$

We choose $\delta = 2t_{n_{max}}$ and obtain

$$\sum_{n=1}^{n_{max}} \frac{\Delta t}{2t_{n_{max}}} \mathcal{W}_h(t_n) \leq \frac{1}{2} \max_k \mathcal{W}_h(t_n).$$

Now, we use the obtained estimate for $\mathcal{W}_h(t_n)$ in (3.30) and get the result. ☐

3.2.2 Stability: Discretizations with Local hp-Refinement in Time

In this section, we present the $\mathbf{L}^2(\Omega)$-stability result from [40] for discretizations with local hp-refinement in time, which do not fulfill assumption 3.1.2. To this end, we consider the stabilized problem (3.14) with the additional stabilization form S_h. It will become clear, that the additional term restores anti-symmetry in the coupling flux-terms.

Stability: $L^2(\Omega)$-Norm

For discretizations with local hp-refinement in time theorem 3.2.1 becomes:

Theorem 3.2.4. *Under assumption 3.1.1 there holds*

$$\begin{aligned}
\mathcal{W}_h(t_{n+1}) - \mathcal{W}_h(t_n) &= \int_{\mathcal{I}_n} \int_{\Omega} \mathbf{J} \cdot \pi_T \mathbf{E}_h \, \mathrm{d}x \, \mathrm{d}t - \int_{\mathcal{I}_n} \int_{\mathcal{F}_b} \mathbf{n} \times \mathbf{g} \cdot \pi_T \mathbf{H}_h \, \mathrm{d}S \, \mathrm{d}t \\
&- \int_{\mathcal{I}_n} \int_{\mathcal{F}_0} \alpha_E [\![\boldsymbol{\pi}_{\tilde{T}} \mathbf{E}_h]\!]_T \cdot [\![\boldsymbol{\pi}_{\tilde{T}} \mathbf{E}_h]\!]_T \, \mathrm{d}S \, \mathrm{d}t - \int_{\mathcal{I}_n} \int_{\mathcal{F}_b} \alpha_E [\![\mathbf{E}_h - \mathbf{g}]\!]_T \cdot [\![\mathbf{E}_h]\!]_T \, \mathrm{d}S \, \mathrm{d}t \\
&- \int_{\mathcal{I}_n} \int_{\mathcal{F}_0} \alpha_H [\![\boldsymbol{\pi}_{\tilde{T}} \mathbf{H}_h]\!]_T \cdot [\![\boldsymbol{\pi}_{\tilde{T}} \mathbf{H}_h]\!]_T \, \mathrm{d}S \, \mathrm{d}t. \qquad (3.32)
\end{aligned}$$

Proof. Since the volume- and boundary-terms can be treated exactly as in the proof of theorem 3.2.1, we only consider the mesh-dependent terms associated with interior faces $f \in \mathcal{F}_0$.

We set $\mathbf{w}_E = \pi_T \mathbf{E}_h, \mathbf{w}_H = \pi_T \mathbf{H}_h$ in (3.14) and obtain

$$
\begin{aligned}
&\int_{\mathcal{I}_n}\int_{\Omega} \varepsilon \partial_t \mathbf{E}_h \cdot \pi_T \mathbf{E}_h \,\mathrm{d}x\,\mathrm{d}t + \int_{\mathcal{I}_n}\int_{\Omega} \mu \partial_t \mathbf{H}_h \cdot \pi_T \mathbf{H}_h \,\mathrm{d}x\,\mathrm{d}t \\
&- \int_{\mathcal{I}_n}\int_{\Omega} \mathbf{H}_h \cdot \nabla_h \times \pi_T \mathbf{E}_h \,\mathrm{d}x\,\mathrm{d}t + \int_{\mathcal{I}_n}\int_{\Omega} \nabla_h \times \mathbf{E}_h \cdot \pi_T \mathbf{H}_h \,\mathrm{d}x\,\mathrm{d}t \\
&+ \int_{\mathcal{I}_n}\int_{\mathcal{F}_0 \cup \mathcal{F}_b} \{\mathbf{H}_h\} \cdot [\![\pi_T \mathbf{E}_h]\!]_T \,\mathrm{d}S\,\mathrm{d}t - \int_{\mathcal{I}_n}\int_{\mathcal{F}_0 \cup \mathcal{F}_b} [\![\mathbf{E}_h]\!]_T \cdot \{\pi_T \mathbf{H}_h\} \,\mathrm{d}S\,\mathrm{d}t \\
&+ \frac{1}{2}\left(\int_{\mathcal{I}_n}\int_{\mathcal{F}_0} \{\mathbf{H}_h\} \cdot [\![\boldsymbol{\pi}_{\tilde{T}} \pi_T \mathbf{E}_h - \pi_T \mathbf{E}_h]\!]_T \,\mathrm{d}S\,\mathrm{d}t + \int_{\mathcal{I}_n}\int_{\mathcal{F}_0} [\![\mathbf{H}_h]\!]_T \cdot \{\boldsymbol{\pi}_{\tilde{T}} \pi_T \mathbf{E}_h - \pi_T \mathbf{E}_h\} \,\mathrm{d}S\,\mathrm{d}t \right) \\
&- \frac{1}{2}\left(\int_{\mathcal{I}_n}\int_{\mathcal{F}_0} \{\mathbf{E}_h\} \cdot [\![\boldsymbol{\pi}_{\tilde{T}} \pi_T \mathbf{H}_h - \pi_T \mathbf{H}_h]\!]_T \,\mathrm{d}S\,\mathrm{d}t + \int_{\mathcal{I}_n}\int_{\mathcal{F}_0} [\![\mathbf{E}_h]\!]_T \cdot \{\boldsymbol{\pi}_{\tilde{T}} \pi_T \mathbf{H}_h - \pi_T \mathbf{H}_h\} \,\mathrm{d}S\,\mathrm{d}t \right) \\
&+ \int_{\mathcal{I}_n}\int_{\mathcal{F}_0} \alpha_E [\![\mathbf{E}_h]\!]_T \cdot [\![\boldsymbol{\pi}_{\tilde{T}} \pi_T \mathbf{E}_h]\!]_T \,\mathrm{d}S\,\mathrm{d}t + \int_{\mathcal{I}_n}\int_{\mathcal{F}_b} \alpha_E [\![\mathbf{E}_h]\!]_T \cdot [\![\pi_T \mathbf{E}_h]\!]_T \,\mathrm{d}S\,\mathrm{d}t \\
&+ \int_{\mathcal{I}_n}\int_{\mathcal{F}_0} \alpha_H [\![\mathbf{H}_h]\!]_T \cdot [\![\boldsymbol{\pi}_{\tilde{T}} \pi_T \mathbf{H}_h]\!]_T \,\mathrm{d}S\,\mathrm{d}t \\
&= \int_{\mathcal{I}_n}\int_{\Omega} \mathbf{J} \cdot \pi_T \mathbf{E}_h \,\mathrm{d}x\,\mathrm{d}t - \int_{\mathcal{I}_n}\int_{\mathcal{F}_b} [\![\mathbf{g}]\!]_T \cdot \pi_T \mathbf{H}_h \,\mathrm{d}S\,\mathrm{d}t + \int_{\mathcal{I}_n}\int_{\mathcal{F}_b} [\![\mathbf{g}]\!]_T \cdot [\![\pi_T \mathbf{E}_h]\!]_T \,\mathrm{d}S\,\mathrm{d}t
\end{aligned}
\tag{3.33}
$$

For an interior face we can rewrite the mesh dependent terms as

$$
\begin{aligned}
&\int_{\mathcal{I}_n}\int_f \{\mathbf{H}_h\}\cdot[\![\pi_{\mathcal{T}}\mathbf{E}_h]\!]_T \,\mathrm{d}S\,\mathrm{d}t - \int_{\mathcal{I}_n}\int_f [\![\mathbf{E}_h]\!]_T\cdot\{\pi_{\mathcal{T}}\mathbf{H}_h\}\,\mathrm{d}S\,\mathrm{d}t\\
&+\frac{1}{2}\left(\left(\int_{\mathcal{I}_n}\int_f \{\mathbf{H}_h\}\cdot[\![\boldsymbol{\pi}_{\tilde{\mathcal{T}}f}\pi_{\mathcal{T}}\mathbf{E}_h-\pi_{\mathcal{T}}\mathbf{E}_h]\!]_T\,\mathrm{d}S\,\mathrm{d}t+\int_{\mathcal{I}_n}\int_f [\![\mathbf{H}_h]\!]_T\cdot\{\boldsymbol{\pi}_{\tilde{\mathcal{T}}f}\pi_{\mathcal{T}}\mathbf{E}_h-\pi_{\mathcal{T}}\mathbf{E}_h\}\,\mathrm{d}S\,\mathrm{d}t\right)\right.\\
&-\frac{1}{2}\left(\left(\int_{\mathcal{I}_n}\int_f \{\mathbf{E}_h\}\cdot[\![\boldsymbol{\pi}_{\tilde{\mathcal{T}}f}\pi_{\mathcal{T}}\mathbf{H}_h-\pi_{\mathcal{T}}\mathbf{H}_h]\!]_T\,\mathrm{d}S\,\mathrm{d}t+\int_{\mathcal{I}_n}\int_f [\![\mathbf{E}_h]\!]_T\cdot\{\boldsymbol{\pi}_{\tilde{\mathcal{T}}f}\pi_{\mathcal{T}}\mathbf{H}_h-\pi_{\mathcal{T}}\mathbf{H}_h\}\,\mathrm{d}S\,\mathrm{d}t\right)\right.\\
&=\frac{1}{2}\int_{\mathcal{I}_n}\int_f \mathbf{H}_h^1\cdot\mathbf{n}^1\times\pi^1\mathbf{E}_h^1\,\mathrm{d}S\,\mathrm{d}t+\frac{1}{2}\int_{\mathcal{I}_n}\int_f \mathbf{H}_h^2\cdot\mathbf{n}^1\times\boldsymbol{\pi}_{\tilde{\mathcal{T}}f}\pi^1\mathbf{E}_h^1\,\mathrm{d}S\,\mathrm{d}t\\
&+\frac{1}{2}\int_{\mathcal{I}_n}\int_f \mathbf{H}_h^1\cdot\mathbf{n}^2\times\boldsymbol{\pi}_{\tilde{\mathcal{T}}f}\pi^2\mathbf{E}_h^2\,\mathrm{d}S\,\mathrm{d}t+\frac{1}{2}\int_{\mathcal{I}_n}\int_f \mathbf{H}_h^2\cdot\mathbf{n}^2\times\pi^2\mathbf{E}_h^2\,\mathrm{d}S\,\mathrm{d}t\\
&-\frac{1}{2}\int_{\mathcal{I}_n}\int_f \pi^1\mathbf{H}_h^1\cdot\mathbf{n}^1\times\mathbf{E}_h^1\,\mathrm{d}S\,\mathrm{d}t-\frac{1}{2}\int_{\mathcal{I}_n}\int_f \boldsymbol{\pi}_{\tilde{\mathcal{T}}f}\pi^1\mathbf{H}_h^1\cdot\mathbf{n}^2\times\mathbf{E}_h^2\,\mathrm{d}S\,\mathrm{d}t\\
&-\frac{1}{2}\int_{\mathcal{I}_n}\int_f \boldsymbol{\pi}_{\tilde{\mathcal{T}}f}\pi^2\mathbf{H}_h^2\cdot\mathbf{n}^1\times\mathbf{E}_h^1\,\mathrm{d}S\,\mathrm{d}t-\frac{1}{2}\int_{\mathcal{I}_n}\int_f \pi^2\mathbf{H}_h^2\cdot\mathbf{n}^2\times\mathbf{E}_h^2\,\mathrm{d}S\,\mathrm{d}t \qquad (3.34)\\
&=T_1+T_2+T_3+T_4+T_5+T_6+T_7+T_8,
\end{aligned}
$$

where π^1 and π^2 are defined as in (3.24). We observe, that only the coupling terms in (3.34) are modified by the stabilization term, compared to (3.24). Thus, we obtain for the non-coupling terms $T_1+T_5=0$ and $T_4+T_8=0$, as in (3.24). There holds

$$
T_2=\frac{1}{2}\int_{\mathcal{I}_n}\int_f \mathbf{H}_h^2\cdot\mathbf{n}^1\times\boldsymbol{\pi}_{\tilde{\mathcal{T}}f}\pi^1\mathbf{E}_h^1\,\mathrm{d}S\,\mathrm{d}t=\frac{1}{2}\int_{\mathcal{I}_n}\int_f \boldsymbol{\pi}_{\tilde{\mathcal{T}}f}\mathbf{H}_h^2\cdot\mathbf{n}^1\times\mathbf{E}_h^1\,\mathrm{d}S\,\mathrm{d}t
$$

and $\pi^1\boldsymbol{\pi}_{\tilde{\mathcal{T}}f}\mathbf{H}_h^2=\boldsymbol{\pi}_{\tilde{\mathcal{T}}f}\mathbf{H}_h^2$, noting that the temporal part of $\boldsymbol{\pi}_{\tilde{\mathcal{T}}f}\mathbf{H}_h^2$ is in $T_{K^1}(\mathcal{I}_n)$. Once more, the symmetry of $\boldsymbol{\pi}_{\tilde{\mathcal{T}}f}$ and π^2 yields

$$
T_7=-\frac{1}{2}\int_{\mathcal{I}_n}\int_f \boldsymbol{\pi}_{\tilde{\mathcal{T}}f}\pi_{\mathcal{T}}\mathbf{H}_h^2\cdot\mathbf{n}^1\times\mathbf{E}_h^1\,\mathrm{d}S\,\mathrm{d}t=-\frac{1}{2}\int_{\mathcal{I}_n}\int_f \boldsymbol{\pi}_{\tilde{\mathcal{T}}f}\mathbf{H}_h^2\cdot\mathbf{n}^1\times\mathbf{E}_h^1\,\mathrm{d}S\,\mathrm{d}t,
$$

such that we obtain $T_2+T_7=0$ and analogously $T_3+T_6=0$. ☐

3.2.3 Bounds on the Discrete error

Before we conduct the analysis, we recall some standard hp-approximation results. Further, we will assume that the spatial mesh-sizes and polynomial degrees are of bounded local variation. This means that for two neighboring elements K^1 and K^2 there holds

$$\gamma^{-1} \leq h_{K^1}/h_{K^2} \leq \gamma, \quad \delta^{-1} \leq p_{s,K^1}/p_{s,K^2} \leq \delta. \tag{3.35}$$

Note, that in this section we denote for better readability $q := p_t$.

hp-Approximation Results

Regarding approximation in the space, we will make use of the following result from [3]:

Lemma 3.2.3. *For* $\mathbf{u} \in \mathbf{H}^k(K)$, $\sigma = \min(p+1, k)$, $0 \leq m \leq k$ *there exists an approximation* $\Pi_m \mathbf{u} \in \mathbf{S}_p(K), p \geq 1$ *and a constant* C*, independent of the discretization parameters but depending of the shape-regularity of* K*, with*

$$\|\mathbf{u} - \Pi_m \mathbf{u}\|_{\mathbf{H}^m(K)} \leq C \frac{h_K^{\sigma-m}}{p_K^{k-m}} \|\mathbf{u}\|_{\mathbf{H}^k(K)}. \tag{3.36}$$

In particular, we can choose $\Pi_0 \mathbf{u} = \Pi_{0,K} \mathbf{u}$, where $\Pi_{0,K}$ denotes the L^2-projection onto $\mathbf{S}_p(K)$. Due to its optimality we have

$$\|\mathbf{u} - \Pi_{0,K} \mathbf{u}\|_{\mathbf{L}^2(K)} \leq C \frac{h_K^{\sigma}}{p_K^{k}} \|\mathbf{u}\|_{\mathbf{H}^k(K)}. \tag{3.37}$$

Furthermore, in order to estimate the mesh-dependent terms of the form, we need to bound the $\mathbf{L}^2$-norm of the trace of the approximation error. To this end we will make use of the following estimate (see for affine hexahedra [30] and for affine tetrahedra [43]). It holds for $\mathbf{u} \in \mathbf{H}^k(K), k > 1/2$:

$$\|\mathbf{u} - \Pi_{0,K} \mathbf{u}\|_{\mathbf{L}^2(\partial K)} \leq C \frac{h_K^{\sigma-1/2}}{p_K^{k-1/2}} \|\mathbf{u}\|_{\mathbf{H}^k(K)}. \tag{3.38}$$

We will also make use of the inverse trace-inequality (see e.g. [58])

$$\|\mathbf{u}\|_{\mathbf{L}^2(\partial K)} \leq C \frac{p}{h_K^{1/2}} \|\mathbf{u}\|_{\mathbf{L}^2(K)} \tag{3.39}$$

Furthermore, for approximation in time we will use an hp-version H^1-conforming interpolant (see [58], Theorems 3.14, 3.17). A similar interpolant has been used in [20].

Lemma 3.2.4. *For $u \in H^l(\mathcal{I}_n)$, $\tau = \min(q_n + 1, l), l \geq 1$ there exists an approximation $\pi_1 u \in P_q(\mathcal{I}_n), p \geq 1$ and a constant C independent of $\Delta t_n, q_n$ with*

$$\begin{aligned}
&\pi_1 u(t_n) = u(t_n), \pi_1 u(t_{n+1}) = u(t_{n+1}) \\
&\int_{\mathcal{I}_n} \partial_t (u - \pi_1 u)\, v \,\mathrm{d}t = 0 \;\forall\; v \;\in P_{q-1}(\mathcal{I}_n) \\
&\|u - \pi_1 u\|_{L^2(\mathcal{I}_n)} \leq C \frac{\Delta t^\tau}{q_n^l} \|u\|_{H^l(\mathcal{I}_n)} \\
&\|\partial_t u - \partial_t \pi_1 u\|_{L^2(\mathcal{I}_n)} \leq C \frac{\Delta t^{\tau-1}}{q^{l-1}} \|u\|_{H^l(\mathcal{I}_n)}
\end{aligned} \tag{3.40}$$

Now we can proceed with the analysis. We begin with making a choice for the interpolation operator I_h. Note, that a “good” choice of I_h is important for the analysis, since it allows to employ several orthogonalities in the estimates. In contrast, a suboptimal choice of the interpolation operator can lead to overly pessimistic error estimates.

Local Bounds on the Discrete Error

Denoting by Π_0 the global L^2-projection with respect to space and by π_1 the projection from Lemma 3.2.4, we exploit the tensor-product structure of $\mathbf{V}_h^n, \mathbf{W}_h^n$ with regard to space and time and choose $I_h = \Pi_0 \pi_1$.
We split the error in approximation and discrete errors

$$\mathbf{u} - \mathbf{u}_h = \boldsymbol{\eta} + \boldsymbol{\xi} \quad \boldsymbol{\eta} = (\boldsymbol{\eta}_E, \boldsymbol{\eta}_H)^T = \mathbf{u} - \Pi_0 \pi_1 \mathbf{u}, \; \boldsymbol{\xi} = (\boldsymbol{\xi}_E, \boldsymbol{\xi}_H)^T = \Pi_0 \pi_1 \mathbf{u} - \mathbf{u}_h.$$

Thus, we obtain from (3.12) as

$$B_h^n(\boldsymbol{\xi}, \mathbf{w}) = B_h^n(-\boldsymbol{\eta}, \mathbf{w}) \;\forall\; \mathbf{w} \in \mathbf{W}_h^k. \tag{3.41}$$

Further, we split the approximation error in its temporal and spatial parts

$$\boldsymbol{\eta} = \mathbf{u} - \pi_1 \mathbf{u} + \pi_1 \mathbf{u} - \Pi_0 \pi_1 \mathbf{u} =: \boldsymbol{\eta}_t + \boldsymbol{\eta}_s \tag{3.42}$$

The following theorem 3.2.5 provides estimates of the right-hand side of (3.41). The first estimate will be used in the case of the weak formulation with dissipative stabilization, since in this case, the jump terms arising in the estimate can be absorbed by those on the left hand side in (3.30). This technique was discovered by Warburton for semidiscrete upwind-flux DG in [66] and also applied in [11]. For the centered flux($\alpha_E = \alpha_H = 0$), the jump terms are not present in the stability estimate (3.30), thus, in this case, we need to treat the jump terms using the inverse inequality (3.39), which yields the second estimate in theorem 3.2.5.

Theorem 3.2.5. *Let assumptions 3.1.1, 3.1.2 and 3.1.3 hold. For* $\mathbf{E},\mathbf{H} \in H^l(\mathcal{I}_n;\mathbf{H}^k(\Omega))$*,* $k > 1/2$*,* $l \geq 1$ *with* $\nabla\times\mathbf{E}, \nabla\times\mathbf{H} \in H^l(\mathcal{I}_n,\mathbf{L}^2(\Omega)$*,* $l \geq 1$*, there holds with* C *and* C_K *independent of* $\Delta t_n, h_K, q_n, p_K$ *and* C_K *depending in general on the maximal number of faces per element, shape-regularity and for* (3.43) *on the stabilization parameters* α_E, α_H

$$
\begin{aligned}
|B_h^n(\boldsymbol{\eta},\mathbf{w})| \leq\ & c_H\|\mathbf{w}_E\|^2_{L^2(\mathcal{I}_n,\mathbf{L}^2(\Omega))} + c_E\|\mathbf{w}_H\|^2_{L^2(\mathcal{I}_n,\mathbf{L}^2(\Omega))}\\
&+c_{f,H}\|\llbracket\mathbf{w}_E\rrbracket_T\|^2_{L^2(\mathcal{I}_n,\mathbf{L}^2(\mathcal{F}))} + c_{f,E}\|\llbracket\mathbf{w}_H\rrbracket_T\|^2_{L^2(\mathcal{I}_n,\mathbf{L}^2(\mathcal{F}_0))}\\
+C\frac{\Delta t_n^{2\tau}}{q_n^{2l}}&\left(c_E^{-1}\|\nabla\times\mathbf{E}\|^2_{H^l(\mathcal{I}_n;\mathbf{L}^2(\Omega))} + c_H^{-1}\|\nabla\times\mathbf{H}\|^2_{H^l(\mathcal{I}_n;\mathbf{L}^2(\Omega))}\right)\\
\sum_K C_K\frac{h_K^{2\sigma_K-1}}{p_K^{2k_K-1}}&\left(c_{f,E}^{-1}\|\mathbf{E}\|^2_{L^2(\mathcal{I}_n;\mathbf{H}^{k_K}(K))} + c_{f,H}^{-1}\|\mathbf{H}\|^2_{L^2(\mathcal{I}_n;\mathbf{H}^{k_K}(K))}\right).
\end{aligned}
\tag{3.43}
$$

For the centered flux formulation ($\alpha_E = \alpha_H = 0$*) there holds*

$$
\begin{aligned}
|B_h^n(\boldsymbol{\eta},\mathbf{w})| \leq\ & c_H\|\mathbf{w}_E\|^2_{L^2(\mathcal{I}_n,\mathbf{L}^2(\Omega))} + c_E\|\mathbf{w}_H\|^2_{L^2(\mathcal{I}_n,\mathbf{L}^2(\Omega))}\\
+C\frac{\Delta t_n^{2\tau}}{q_n^{2l}}&\left(c_E^{-1}\|\nabla\times\mathbf{E}\|^2_{H^l(\mathcal{I}_n;\mathbf{L}^2(\Omega))} + c_H^{-1}\|\nabla\times\mathbf{H}\|^2_{H^l(\mathcal{I}_n;\mathbf{L}^2(\Omega))}\right)\\
\sum_K C_K\frac{h_K^{2\sigma_K-2}}{p_K^{2k_K-3}}&\left(c_E^{-1}\|\mathbf{E}\|^2_{L^2(\mathcal{I}_n;\mathbf{H}^{k_K}(K))} + c_H^{-1}\|\mathbf{H}\|^2_{L^2(\mathcal{I}_n;\mathbf{H}^{k_K}(K))}\right).
\end{aligned}
\tag{3.44}
$$

$$
\tag{3.45}
$$

Proof. We begin with showing that (3.43) holds. Please note that, for brevity, we present only the estimates related to the electric equation, the magnetic equation can be treated analogously.

Recalling the decomposition $B_h^n(\boldsymbol{\eta},\mathbf{w}) = B_h^n(\boldsymbol{\eta}_t,\mathbf{w}) + B_h^n(\boldsymbol{\eta}_s,\mathbf{w})$, we begin with estimating $|B_h^n(\boldsymbol{\eta}_t,\mathbf{w})|$:

Starting with the terms containing the time-derivatives we have, using the properties of π_1 from Lemma 3.2.4,

$$
\int_{\mathcal{I}_n}\int_\Omega \varepsilon(\partial_t\pi_1\mathbf{E} - \partial_t\mathbf{E})\cdot\mathbf{w}_E\,\mathrm{d}x\,\mathrm{d}t = 0,
$$

since the temporal part of $\mathbf{w}$ belongs to $P_{q-1}(\mathcal{I}_n)$.

The terms involving the curls of the temporal error can be estimated as

$$
\left|\int_{\mathcal{I}_n}\int_\Omega \nabla\times(\pi_1\mathbf{E}-\mathbf{E})\cdot\mathbf{w}\,\mathrm{d}x\,\mathrm{d}t\right| \leq C\frac{\Delta t_n^\tau}{q_n^l}\|\nabla\times\mathbf{E}\|_{H^l(\mathcal{I}_n;\mathbf{L}^2(\Omega))}\|\mathbf{w}_H\|_{L^2(\mathcal{I}_n;\mathbf{L}^2(\Omega))},
\tag{3.46}
$$

where we have used the Cauchy-Schwarz inequality and Lemma 3.2.4.
Remark: All other terms associated with $B_h(\pi_1\mathbf{u}-\mathbf{u},\mathbf{w})$ are mesh-dependent and involve tangential jumps of the interpolation errors. Since the temporal interpolation errors are tangentially continuous, all these terms vanish.
Now, we turn to the estimation of the spatial part $B_h(\boldsymbol{\eta}_s,\mathbf{w})$:
Again we start with the time derivative terms. Considering the term involving the electric field we have, using $\mathbf{w}_E \in W_h^n$ and the orthogonality of the spatial L^2-projection Π_0

$$\int_{\mathcal{I}_n}\int_{\Omega} \varepsilon(\partial_t \Pi_0 \pi_1 \mathbf{E} - \partial_t \pi_1 \mathbf{E}) \cdot \mathbf{w}_E \,\mathrm{d}x\,\mathrm{d}t = 0$$

The same holds for the curl-term involving $\mathbf{H}$

$$\int_{\mathcal{I}_n}\int_{\Omega} (\Pi_0 \pi_1 \mathbf{H} - \pi_1 \mathbf{H}) \cdot \nabla_h \times \mathbf{w}_E \,\mathrm{d}x\,\mathrm{d}t = 0,$$

and after an element-wise integration by parts for the curl-term involving $\mathbf{E}$.
What remains is to estimate the mesh-dependent terms. We have,

$$\left|\int_{\mathcal{I}_n}\int_{\mathcal{F}} \{\Pi_0 \pi_1 \mathbf{H} - \pi_1 \mathbf{H}\} \cdot [\![\mathbf{w}_E]\!]_T \,\mathrm{d}S\,\mathrm{d}t\right|$$

$$\leq \left(\sum_{f\in\mathcal{F}} \|\{\Pi_0 \pi_1 \mathbf{H} - \pi_1 \mathbf{H}\}\|^2_{L^2(\mathcal{I}_n;\mathbf{L}^2(f))}\right)^{1/2} \|[\![\mathbf{w}_E]\!]_T\|_{L^2(\mathcal{I}_n;\mathbf{L}^2(\mathcal{F}))}. \tag{3.47}$$

(3.48)

With $f = \partial K^1 \cap \partial K^2$, there holds

$$\begin{aligned}
&\sum_{f\in\mathcal{F}} \|\{\Pi_0 \pi_1 \mathbf{H} - \pi_1 \mathbf{H}\}\|^2_{L^2(\mathcal{I}_n;\mathbf{L}^2(f))} \\
&\leq \sum_{f\in\mathcal{F}} C\left(\|\Pi_{0,K^1} \pi_1 \mathbf{H} - \pi_1 \mathbf{H}\|^2_{L^2(\mathcal{I}_n;\mathbf{L}^2(f))} + \|\Pi_{0,K^2} \pi_1 \mathbf{H} - \pi_1 \mathbf{H}\|^2_{L^2(\mathcal{I}_n;\mathbf{L}^2(f))}\right) \\
&\leq \sum_{K} C\|\Pi_{0,K} \pi_1 \mathbf{H} - \pi_1 \mathbf{H}\|^2_{L^2(\mathcal{I}_n;\mathbf{L}^2(\partial K))} \leq \sum_{K} C\frac{h_K^{2\sigma_K-1}}{p_K^{2k_K-1}} \|\mathbf{H}\|^2_{L^2(\mathcal{I}_n;\mathbf{H}^{k_K}(K))},
\end{aligned}$$

where we have applied (3.38) in the last step.
Note that the constant also depends on the number of faces (i.e. neighboring

elements) of K (maximum of 24 and 16 faces for a hexahedron or tetrahedron respectively). Similarly, we have

$$\left|\int_{\mathcal{I}_n}\int_{\mathcal{F}} \alpha_E [\![\Pi_0\pi_1\mathbf{E}-\pi_1\mathbf{E}]\!]_T \cdot [\![\mathbf{w}_E]\!]_T \,\mathrm{d}S\,\mathrm{d}t\right|$$

$$\leq \left(\sum_K C\frac{h_K^{2\sigma_K-1}}{p_K^{2k_K-1}}\|\mathbf{E}\|^2_{L^2(\mathcal{I}_n;\mathbf{H}^{k_K}(K))}\right)^{1/2} \|[\![\mathbf{w}_E]\!]_T\|_{L^2(\mathcal{I}_n;\mathbf{L}^2(\mathcal{F}_0))}. \tag{3.49}$$

Thus, after applying Cauchy's inequality, we have proven (3.43).
We turn now to (3.44). The only difference lies in estimating the mesh dependent terms: Denoting with $NB(K)$ the set of all neighbors of element K we have

$$\left|\int_{\mathcal{I}_n}\int_{\mathcal{F}} \{\Pi_0\pi_1\mathbf{H}-\pi_1\mathbf{H}\} \cdot [\![\mathbf{w}_E]\!]_T \,\mathrm{d}S\,\mathrm{d}t\right|$$

$$\leq \sum_K C_K\|\Pi_0\pi_1\mathbf{H}-\pi_1\mathbf{H}\|_{L^2(\mathcal{I}_n;\mathbf{L}^2(\partial K))}\|\mathbf{n}\times\mathbf{w}_E\|_{L^2(\mathcal{I}_n;\mathbf{L}^2(\partial K))}$$

$$+\sum_{K'\in NB(K)} C\|\Pi_{0,K'}\pi_1\mathbf{H}-\pi_1\mathbf{H}\|_{L^2(\mathcal{I}_n;\mathbf{L}^2(\partial K\cap\partial K'))}\|\mathbf{n}\times\mathbf{w}_E\|_{L^2(\mathcal{I}_n;\mathbf{L}^2(\partial K))}.$$

Estimating the traces of the projection errors on the faces with (3.38), $\|\mathbf{n}\times\mathbf{w}_E\|_{L^2(\mathcal{I}_n;\mathbf{L}^2(\partial K))}$ with the inverse trace-inequality (3.39) and using that the mesh-sizes and polynomial degrees are of bounded local variation (3.35), we obtain

$$\left|\int_{\mathcal{I}_n}\int_{\mathcal{F}} \{\Pi_0\pi_1\mathbf{H}-\pi_1\mathbf{H}\} \cdot [\![\mathbf{w}_E]\!]_T \,\mathrm{d}S\,\mathrm{d}t\right|$$

$$\leq \sum_K C\frac{h^{\sigma_K-1}}{p_K^{k_K-3/2}}\|\mathbf{H}\|_{L^2(\mathcal{I}_n;\mathbf{H}^{k_{K'}}(K))}\|\mathbf{w}_E\|_{L^2(\mathcal{I}_n;\mathbf{L}^2(K))}$$

$$+\sum_{K'\in NB(K)} C\frac{h^{\sigma_{K'}-1}}{p_{K'}^{k_{K'}-3/2}}\|\mathbf{H}\|_{L^2(\mathcal{I}_n;\mathbf{H}^{k_{K'}}(K')]^3)}\|\mathbf{w}_E\|_{L^2(\mathcal{I}_n;\mathbf{L}^2(K))}.$$

Applying the Cauchy's inequality with $c_H > 0$ leads to

$$\left|\int_{\mathcal{I}_n}\int_{\mathcal{F}} \{\Pi_0\pi_1\mathbf{H}-\pi_1\mathbf{H}\} \cdot [\![\mathbf{w}_E]\!]_T \,\mathrm{d}S\,\mathrm{d}t\right|$$

$$\leq c_H^{-1}\sum_K C_K\frac{h^{2s_K-2}}{p_K^{2k_K-3}}\|\mathbf{H}\|^2_{L^2(\mathcal{I}_n;\mathbf{H}^{k_K}(K)]^3)} + c_H\|\mathbf{w}_E\|^2_{L^2(\mathcal{I}_n;\mathbf{L}^2(K))}. \tag{3.50}$$

The constants are independent of h, p and α, but depend on the shape-regularity of the mesh, the maximal number of neighbors per element and the constants γ, δ from (3.35). Applying Cauchy's inequality also to the estimate (3.46), we arrive at (3.44). $\square$

Together with Lemma 3.2.2 we can give the following bounds for the local discrete errors $\xi_E = \Pi_0 \pi_1 \mathbf{E} - \mathbf{E}_h$, $\xi_H = \Pi_0 \pi_1 \mathbf{H} - \mathbf{H}_h$.

Lemma 3.2.5. *Under the assumptions of theorem 3.2.5, there holds in case of the centered flux*

$$
\begin{aligned}
&\|\varepsilon^{\frac{1}{2}} \xi_E\|^2_{L^2(\mathcal{I}_n;\mathbf{L}^2(\Omega))} + \|\mu^{\frac{1}{2}} \xi_H\|^2_{L^2(\mathcal{I}_n;\mathbf{L}^2(\Omega))} \\
\leq\, & C \Delta t_n^2 \frac{\Delta t_n^{2\tau}}{q_n^{2l}} \left(\underline{\varepsilon}^{-1} \|\nabla \times \mathbf{H}\|^2_{H^l(\mathcal{I}_n;\mathbf{L}^2(\Omega))} + \underline{\mu}^{-1} \|\nabla \times \mathbf{E}\|^2_{H^l(\mathcal{I}_n;\mathbf{L}^2(\Omega))} \right) \\
& + \Delta t_n^2 \sum_K C_K \frac{h_K^{2\sigma-2}}{p_K^{2k-3}} \left(\underline{\varepsilon}^{-1} \|\mathbf{E}\|^2_{L^2(\mathcal{I}_n;\mathbf{H}^k(K))} + \underline{\mu}^{-1} \|\mathbf{H}\|^2_{L^2(\mathcal{I}_n;\mathbf{H}^k(K))} \right) \\
& + \Delta t_n C \left(\|\varepsilon^{\frac{1}{2}} \xi_E(t_n)\|^2_{\mathbf{L}^2(\Omega)} + \|\mu^{\frac{1}{2}} \xi_E(t_n)\|^2_{\mathbf{L}^2(\Omega)} \right).
\end{aligned} \tag{3.51}
$$

For the dissipative flux with $\alpha_E \geq \underline{\alpha}_E > 0$, $\alpha_H \geq \underline{\alpha}_H > 0$, there holds

$$
\begin{aligned}
&\|\varepsilon \xi_E\|^2_{L^2(\mathcal{I}_n;\mathbf{L}^2(\Omega))} + \|\mu \xi_H\|^2_{L^2(\mathcal{I}_n;\mathbf{L}^2(\Omega))} \\
\leq\, & \Delta t_n^2 C \frac{\Delta t_n^{2\tau}}{q_n^{2l}} \left(\underline{\varepsilon}^{-1} \|\nabla \times \mathbf{H}\|^2_{H^l(\mathcal{I}_n;\mathbf{L}^2(\Omega))} + \underline{\mu}^{-1} \|\nabla \times \mathbf{E}\|^2_{H^l(\mathcal{I}_n;\mathbf{L}^2(\Omega))} \right) \\
& + \Delta t_n \sum_K C_K \frac{h_K^{2\sigma-1}}{p_K^{2k-1}} \left(\underline{\alpha}_H^{-1} \|\mathbf{E}\|^2_{L^2(\mathcal{I}_n;\mathbf{H}^k(K))} + \underline{\alpha}_E^{-1} \|\mathbf{H}\|^2_{L^2(\mathcal{I}_n;\mathbf{H}^k(K))} \right) \\
& + \Delta t_n C \left(\|\varepsilon \xi_E(t_n)\|^2_{\mathbf{L}^2(\Omega)} + \|\mu \xi_E(t_n)\|^2_{\mathbf{L}^2(\Omega)} \right).
\end{aligned} \tag{3.52}
$$

Proof. Using lemma 3.2.2 with (3.41) we have

$$
\begin{aligned}
&\frac{1}{2\Delta t_n} \|\varepsilon^{\frac{1}{2}} \xi_E\|^2_{L^2(\mathcal{I}_n;\mathbf{L}^2(\Omega))} + \frac{1}{2\Delta t_n} \|\mu^{\frac{1}{2}} \xi_H\|^2_{L^2(\mathcal{I}_n;\mathbf{L}^2(\Omega))} \\
& + \|(\alpha_E \tau)^{\frac{1}{2}} [\![\pi_T \xi_E]\!]_T\|^2_{L^2(\mathcal{I}_n;\mathbf{L}^2(\mathcal{F}))} + \|(\alpha_H \tau)^{\frac{1}{2}} [\![\pi_T \xi_H]\!]_T\|^2_{L^2(\mathcal{I}_n;\mathbf{L}^2(\mathcal{F}))} \\
\leq\, & B_h^n(-\boldsymbol{\eta}, \pi_T \tau \pi_T \xi) + \frac{1}{2} \|\varepsilon^{\frac{1}{2}} \xi_E(t_n)\|^2_{\mathbf{L}^2(\Omega)} + \frac{1}{2} \|\mu^{\frac{1}{2}} \xi_H(t_n)\|^2_{\mathbf{L}^2(\Omega)}
\end{aligned} \tag{3.53}
$$

In case of the centered flux formulation estimate (3.44) from theorem 3.2.5 leads to

$$\begin{aligned}
&\|\varepsilon^{\frac{1}{2}}\xi_E\|^2_{L^2(\mathcal{I}_n;\mathbf{L}^2(\Omega))} + \|\mu^{\frac{1}{2}}\xi_H\|^2_{L^2(\mathcal{I}_n;\mathbf{L}^2(\Omega))} \\
\leq C\Delta t_n \frac{\Delta t_n^{2\tau}}{q_n^{2l}} &\left(c_H^{-1}\|\nabla\times\mathbf{H}\|^2_{H^l(\mathcal{I}_n;\mathbf{L}^2(\Omega))} + c_E^{-1}\|\nabla\times\mathbf{E}\|^2_{H^l(\mathcal{I}_n;\mathbf{L}^2(\Omega))}\right) \\
\Delta t_n \sum_K C_K \frac{h_K^{2\sigma-2}}{p_K^{2k-3}} &\left(c_E^{-1}\|\mathbf{E}\|^2_{L^2(\mathcal{I}_n;\mathbf{H}^k(K))} + c_H^{-1}\|\mathbf{H}\|^2_{L^2(\mathcal{I}_n;\mathbf{H}^k(K))}\right) \\
&+\|\varepsilon^{\frac{1}{2}}\xi_E(t_n)\|^2_{\mathbf{L}^2(\Omega)} + \|\mu^{\frac{1}{2}}\xi_H(t_n)\|^2_{\mathbf{L}^2(\Omega)} \\
+c_H 2\Delta t_n\|\pi_T\tau\pi_T\xi_E\|^2_{L^2(\mathcal{I}_n;\mathbf{L}^2(\Omega))} &+ c_E 2\Delta t_n\|\pi_T\tau\pi_T\xi_H\|^2_{L^2(\mathcal{I}_n;\mathbf{L}^2(\Omega))}
\end{aligned}$$

Since $\|\pi_T\| \leq 1$ and $1 \geq \tau(t) \geq 0$ on $\mathcal{I}$, together with the choice $c_H = c\underline{\varepsilon}/\Delta t_n, c_E = c\underline{\mu}/\Delta t_n$ with $c > 0$ and small enough, we obtain the result for the centered flux case.

The result for the dissipative flux formulation is obtained analogously using (3.43) from theorem 3.2.5 with (3.53) and $c_{f,H} = c\underline{\alpha}_E, c_{f,E} = c\underline{\alpha}_H$ with $c > 0$ and small enough. ☐

Global Bounds on the Discrete Error

Global bounds on the discrete errors in the $\mathbf{L}^2(\Omega)$- and $L^2(\mathcal{I},\mathbf{L}^2(\Omega))$-norms can be obtained, proceeding similarly as in the proof of theorem 3.2.3. In particular we have

Lemma 3.2.6. *Under the assumptions of theorem 3.2.5, there holds for the centered formulation*

$$\begin{aligned}
&\max_{n\leq N}\left(\|\varepsilon^{\frac{1}{2}}\xi_E(t_n)\|^2_{\mathbf{L}^2(\Omega)} + \|\mu^{\frac{1}{2}}\xi_H(t_n)\|^2_{\mathbf{L}^2(\Omega)}\right) \\
\leq T\sum_{n=1}^{N} C\frac{\Delta t_n^{2\tau}}{q_n^{2l}} &\left(\underline{\varepsilon}^{-1}\|\nabla\times\mathbf{H}\|^2_{H^l(\mathcal{I}_n;\mathbf{L}^2(\Omega))} + \underline{\mu}^{-1}\|\nabla\times\mathbf{E}\|^2_{H^l(\mathcal{I}_n;\mathbf{L}^2(\Omega))}\right) \\
+T\sum_{n=1}^{N}\sum_K C_K\frac{h_K^{2\sigma-2}}{p_K^{2k-3}} &\left(\underline{\mu}^{-1}\|\mathbf{E}\|^2_{L^2(\mathcal{I}_n;\mathbf{H}^k(K))} + \underline{\varepsilon}^{-1}\|\mathbf{H}\|^2_{L^2(\mathcal{I}_n;\mathbf{H}^k(K))}\right),
\end{aligned} \tag{3.54}$$

$$\begin{aligned}
&\|\varepsilon^{\frac{1}{2}}\xi_E\|^2_{L^2(\mathcal{I}_n;\mathbf{L}^2(\Omega))} + \|\mu^{\frac{1}{2}}\xi_H\|^2_{L^2(\mathcal{I}_n;\mathbf{L}^2(\Omega))} \\
&\le T^2 \sum_{n=1}^{N} C \frac{\Delta t_n^{2\tau}}{q_n^{2l}} \left(\underline{\varepsilon}^{-1} \|\nabla \times \mathbf{H}\|^2_{H^l(\mathcal{I}_n;\mathbf{L}^2(\Omega))} + \underline{\mu}^{-1} \|\nabla \times \mathbf{E}\|^2_{H^l(\mathcal{I}_n;\mathbf{L}^2(\Omega))} \right) \\
&\quad + T^2 \sum_{n=1}^{N} \sum_{K} C_K \frac{h_K^{2\sigma-2}}{p_K^{2k-3}} \left(\underline{\mu}^{-1} \|\mathbf{E}\|^2_{L^2(\mathcal{I}_n;\mathbf{H}^k(K))} + \underline{\varepsilon}^{-1} \|\mathbf{H}\|^2_{L^2(\mathcal{I}_n;\mathbf{H}^k(K))} \right).
\end{aligned} \tag{3.55}$$

For the dissipative formulation there holds

$$\begin{aligned}
&\max_{n\le N} \left(\|\varepsilon^{\frac{1}{2}}\xi_E(t_n)\|^2_{\mathbf{L}^2(\Omega)} + \|\mu^{\frac{1}{2}}\xi_H(t_n)\|^2_{\mathbf{L}^2(\Omega)} \right) \\
&\le T \sum_{n=1}^{N} C \frac{\Delta t_n^{2\tau}}{q_n^{2l}} \left(\underline{\varepsilon}^{-1} \|\nabla \times \mathbf{H}\|^2_{H^l(\mathcal{I}_n;\mathbf{L}^2(\Omega))} + \underline{\mu}^{-1} \|\nabla \times \mathbf{E}\|^2_{H^l(\mathcal{I}_n;\mathbf{L}^2(\Omega))} \right) \\
&\quad + T \sum_{n=1}^{N} \sum_{K} C_K \frac{h_K^{2\sigma-1}}{p_K^{2k-1}} \left(\underline{\alpha}_H^{-1} \|\mathbf{E}\|^2_{L^2(\mathcal{I}_n;\mathbf{H}^k(K))} + \underline{\alpha}_E^{-1} \|\mathbf{H}\|^2_{L^2(\mathcal{I}_n;\mathbf{H}^k(K))} \right),
\end{aligned} \tag{3.56}$$

$$\begin{aligned}
&\|\varepsilon^{\frac{1}{2}}\xi_E\|^2_{L^2(\mathcal{I}_n;\mathbf{L}^2(\Omega))} + \|\mu^{\frac{1}{2}}\xi_H\|^2_{L^2(\mathcal{I}_n;\mathbf{L}^2(\Omega))} \\
&\le T^2 \sum_{n=1}^{N} C \frac{\Delta t_n^{2\tau}}{q_n^{2l}} \left(\underline{\varepsilon}^{-1} \|\nabla \times \mathbf{H}\|^2_{H^l(\mathcal{I}_n;\mathbf{L}^2(\Omega))} + \underline{\mu}^{-1} \|\nabla \times \mathbf{E}\|^2_{H^l(\mathcal{I}_n;\mathbf{L}^2(\Omega))} \right) \\
&\quad + T^2 \sum_{n=1}^{N} \sum_{K} C_K \frac{h_K^{2\sigma-1}}{p_K^{2k-1}} \left(\underline{\alpha}_H^{-1} \|\mathbf{E}\|^2_{L^2(\mathcal{I}_n;\mathbf{H}^k(K))} + \underline{\alpha}_E^{-1} \|\mathbf{H}\|^2_{L^2(\mathcal{I}_n;\mathbf{H}^k(K))} \right).
\end{aligned} \tag{3.57}$$

3.2.4 Convergence

In order to prove the desired convergence theorem it remains to employ theorem 3.2.3 and 3.2.4 to bound the approximation errors $\|\varepsilon\boldsymbol{\eta}_E\|^2_{\mathbf{L}^2(\Omega)} + \|\mu\boldsymbol{\eta}_H\|^2_{\mathbf{L}^2(\Omega)}$ and $\|\varepsilon\boldsymbol{\eta}_E\|^2_{L^2(\mathcal{I};\mathbf{L}^2(\Omega))} + \|\mu\boldsymbol{\eta}_H\|^2_{L^2(\mathcal{I};\mathbf{L}^2(\Omega))}$. Using lemma 3.2.6 we obtain

Theorem 3.2.6. *Under the assumptions of theorem 3.2.5 there holds for the centered formulation*

$$
\begin{aligned}
&\max_{n\le N}\Big(\|\varepsilon^{\frac12}\left(\mathbf{E}(t_n)-\mathbf{E}_h(t_n)\right)\|^2_{\mathbf{L}^2(\Omega)}+\|\mu^{\frac12}\left(\mathbf{H}(t_n)-\mathbf{H}_h(t_n)\right)\|^2_{\mathbf{L}^2(\Omega)}\Big)\\
&\le T\sum_{n=1}^{N} C\frac{\Delta t_n^{2\tau}}{q_n^{2l}}\left(\underline{\varepsilon}^{-1}\|\nabla\times\mathbf{H}\|^2_{H^l(\mathcal{I}_n;\mathbf{L}^2(\Omega))}+\underline{\mu}^{-1}\|\nabla\times\mathbf{E}\|^2_{H^l(\mathcal{I}_n;\mathbf{L}^2(\Omega))}\right)\\
&\quad+T\sum_{n=1}^{N}\sum_{K} C_K\frac{h_K^{2\sigma-2}}{p_K^{2k-3}}\left(\underline{\mu}^{-1}\|\mathbf{E}\|^2_{L^2(\mathcal{I}_n;\mathbf{H}^k(K))}+\underline{\varepsilon}^{-1}\|\mathbf{H}\|^2_{L^2(\mathcal{I}_n;\mathbf{H}^k(K))}\right)\\
&\quad+\max_{n\le N}\sum_{K} C_K\frac{h_K^{2\sigma_K}}{p_K^{2k_K}}\left(\|\varepsilon^{\frac12}\mathbf{E}(t_n)\|^2_{\mathbf{H}^k(K)}+\|\mu^{\frac12}\mathbf{H}(t_n)\|^2_{\mathbf{H}^k(K)}\right),
\end{aligned}
\tag{3.58}
$$

$$
\begin{aligned}
&\|\varepsilon^{\frac12}\left(\mathbf{E}(t_n)-\mathbf{E}_h(t_n)\right)\|^2_{L^2(\mathcal{I}_n;\mathbf{L}^2(\Omega))}+\|\mu^{\frac12}\left(\mathbf{H}(t_n)-\mathbf{H}_h(t_n)\right)\|^2_{L^2(\mathcal{I}_n;\mathbf{L}^2(\Omega))}\\
&\le T^2\sum_{n=1}^{N} C\frac{\Delta t_n^{2\tau}}{q_n^{2l}}\left(\underline{\varepsilon}^{-1}\|\nabla\times\mathbf{H}\|^2_{H^l(\mathcal{I}_n;\mathbf{L}^2(\Omega))}+\underline{\mu}^{-1}\|\nabla\times\mathbf{E}\|^2_{H^l(\mathcal{I}_n;\mathbf{L}^2(\Omega))}\right)\\
&+(T^2+1)\sum_{n=1}^{N}\sum_{K} C_K\frac{h_K^{2\sigma-2}}{p_K^{2k-3}}\left(\underline{\mu}^{-1}\|\mathbf{E}\|^2_{L^2(\mathcal{I}_n;\mathbf{H}^k(K))}+\underline{\varepsilon}^{-1}\|\mathbf{H}\|^2_{L^2(\mathcal{I}_n;\mathbf{H}^k(K))}\right).
\end{aligned}
\tag{3.59}
$$

And for the dissipative formulation

$$
\begin{aligned}
&\max_{n\le N}\Big(\|\varepsilon^{\frac12}\left(\mathbf{E}(t_n)-\mathbf{E}_h(t_n)\right)\|^2_{\mathbf{L}^2(\Omega)}+\|\mu^{\frac12}\left(\mathbf{H}(t_n)-\mathbf{H}_h(t_n)\right)\|^2_{\mathbf{L}^2(\Omega)}\Big)\\
&\le T\sum_{n=1}^{N} C\frac{\Delta t_n^{2\tau}}{q_n^{2l}}\left(\underline{\varepsilon}^{-1}\|\nabla\times\mathbf{H}\|^2_{H^l(\mathcal{I}_n;\mathbf{L}^2(\Omega))}+\underline{\mu}^{-1}\|\nabla\times\mathbf{E}\|^2_{H^l(\mathcal{I}_n;\mathbf{L}^2(\Omega))}\right)\\
&\quad+T\sum_{n=1}^{N}\sum_{K} C_K\frac{h_K^{2\sigma-1}}{p_K^{2k-1}}\left(\underline{\alpha}_H^{-1}\|\mathbf{E}\|^2_{L^2(\mathcal{I}_n;\mathbf{H}^k(K))}+\underline{\alpha}_E^{-1}\|\mathbf{H}\|^2_{L^2(\mathcal{I}_n;\mathbf{H}^k(K))}\right)\\
&\quad+\max_{n\le N}\sum_{K} C_K\frac{h_K^{2\sigma_K}}{p_K^{2k_K}}\left(\|\varepsilon^{\frac12}\mathbf{E}(t_n)\|^2_{\mathbf{H}^k(K)}+\|\mu^{\frac12}\mathbf{H}(t_n)\|^2_{\mathbf{H}^k(K)}\right),
\end{aligned}
\tag{3.60}
$$

$$
\begin{aligned}
&\|\varepsilon^{\frac12}\left(\mathbf{E}(t_n)-\mathbf{E}_h(t_n)\right)\|^2_{L^2(\mathcal{I}_n;\mathbf{L}^2(\Omega))}+\|\mu^{\frac12}\left(\mathbf{H}(t_n)-\mathbf{H}_h(t_n)\right)\|^2_{L^2(\mathcal{I}_n;\mathbf{L}^2(\Omega))}\\
&\le T^2\sum_{n=1}^{N} C\frac{\Delta t_n^{2\tau}}{q_n^{2l}}\left(\underline{\varepsilon}^{-1}\|\nabla\times\mathbf{H}\|^2_{H^l(\mathcal{I}_n;\mathbf{L}^2(\Omega))}+\underline{\mu}^{-1}\|\nabla\times\mathbf{E}\|^2_{H^l(\mathcal{I}_n;\mathbf{L}^2(\Omega))}\right)\\
&\quad+T^2\sum_{n=1}^{N}\sum_{K} C_K\frac{h_K^{2\sigma-1}}{p_K^{2k-1}}\left(\underline{\alpha}_H^{-1}\|\mathbf{E}\|^2_{L^2(\mathcal{I}_n;\mathbf{H}^k(K))}+\underline{\alpha}_E^{-1}\|\mathbf{H}\|^2_{L^2(\mathcal{I}_n;\mathbf{H}^k(K))}\right).
\end{aligned}
\tag{3.61}
$$

For the special case of uniform spatial polynomial degrees and quasi-uniform meshes, the part of the error associated with the spatial part of the discretization is of order $h^{p_s}/p_s^{k-3/2}$ for the non-dissipative centered flux formulation and $h^{p_s+1/2}/p_s^{k-1/2}$ for the dissipative formulation, provided the solution is sufficiently smooth. The temporal part of the error is in both cases of order $\Delta t^{p_t+1}/p_t^l$. The maximal error at the time nodes, measured in the $\|\cdot\|_{\mathbf{L}^2(\Omega)}$-norm grows with $\sqrt{T}$, the error measured in the $\|\cdot\|_{L^2(\mathcal{I}_n;\mathbf{L}^2(\Omega))}$ grows with T.

3.2.5 Extension to Variable Discretizations

For the *a priori* error analysis we have so far only considered the case, when assumption 3.1.3 holds, i.e. the discretization is kept constant for all time slabs and the error due to the approximation of the initial data is zero. However, in the context of adaptivity, the discretization might be adapted dynamically for each time-slab [55, 56], in order to resolve travelling wave-fronts in an efficient way. To this end, we allow for each time slab possibly different trial- and test spaces $\mathbf{V}_h^n$ and $\mathbf{W}_h^n$, where the superscript n denotes the time-slab. The solution is transferred by the L^2-projection from the end of one time-slab to the next one. This leads to the problem

$$\begin{aligned} &\text{Find } \mathbf{u}_h^n \in \mathbf{V}_h^n \\ &B_h^n(\mathbf{u}_h^n, \mathbf{w}) = L^n(\mathbf{w}) \ \forall \ \mathbf{w} \in \mathbf{W}_h^n \\ &\mathbf{u}_h^n(t_n) = \Pi_0^n \mathbf{u}_h^{n-1}(t_n) \end{aligned} \tag{3.62}$$

for each time-slab. Note, that now the solution is not time-continuous at the time-nodes t_n, unless the spatial part of $\mathbf{V}_h^n$ contains the one of $\mathbf{V}_h^{n-1}$.
Since $\|\Pi_0\| \leq 1$, we have for $t = t_n$

$$\begin{aligned} &\int_\Omega \varepsilon \Pi_0^n \mathbf{E}_h^{n-1} \cdot \Pi_0^n \mathbf{E}_h^{n-1} \, \mathrm{d}x + \int_\Omega \mu \Pi_0^n \mathbf{H}_h^{n-1} \cdot \Pi_0^n \mathbf{H}_h^{n-1} \, \mathrm{d}x \\ &\qquad \leq \int_\Omega \varepsilon \mathbf{E}_h^{n-1} \cdot \mathbf{E}_h^{n-1} \, \mathrm{d}x + \int_\Omega \mu \mathbf{H}_h^{n-1} \cdot \mathbf{H}_h^{n-1} \, \mathrm{d}x, \end{aligned}$$

thus, dynamically changing discretizations do not affect the stability of the method, instead they render the scheme dissipative, where the amount of dissipation is determined by the projection errors between time-slabs. Noting, that the consistency analysis yields additional terms,

$$
\begin{aligned}
&\sum_{n=1}^{N} \int_{\Omega} \left(\boldsymbol{\eta}^n(t_n) - \boldsymbol{\eta}^{n-1}(t_n)\right) \cdot \boldsymbol{\xi}(\mathbf{t_n})\,\mathrm{d}x \\
\leq &\sum_{n=1}^{N} \left[\|\boldsymbol{\eta}^n(t_n)\|_{\mathrm{L}^2(\Omega)} + \|\boldsymbol{\eta}^{n-1}(t_n)\|_{\mathrm{L}^2(\Omega)}\right] \|\boldsymbol{\xi}(t_n)\|_{\mathrm{L}^2(\Omega)}
\end{aligned}
$$

which can be bounded using theorem 3.2.3 elementwise, analogously to the error due to the approximation of the initial data.

3.3 Iterative Solution and Computational Complexity

In this section we present strategies, published in [40], for efficiently solving the linear systems due to (3.9).

In particular for three-dimensional problems, the linear system of equations governed by (3.9) is often very large. In this case, the direct solution may become unfeasible due to the computational complexity and high memory demands of sparse direct solvers. Furthermore, for adaptive simulations the discretization may change from time slab to time slab, such that the linear systems have to be reassembled. Therefore, we solve the linear systems iteratively and implement the evaluation of the residual

$$
R_h^n(\mathbf{w}) = B_h^n(\mathbf{u}_h, \mathbf{w}) - L_h^n(\mathbf{w}) \tag{3.63}
$$

directly without storing element matrices. Additionally, under the assumptions of theorem 3.2.3 we derive a guaranteed bound for the error due to inexact iterative solution. The error bound can be employed to balance discretization and iteration errors, which leads to a significant reduction of iterations. Thus, the resulting method shares many computational advantages of explicit methods.

3.3.1 Basis Functions for Trial- and Test-Space

We denote by $L_i(\xi)\, i = 0, ..., p$ the orthonormal Legendre polynomials on $[0,1]$ and by $l_i(t)$, the integrated Legendre polynomials on $[0,1]$:

$$
l_0(\xi) = 1 - \xi, \qquad l_1(\xi) = \xi, \qquad l_i(\xi) = \int_0^{\xi} L_{i-1}(s)ds \;\; i = 2, ..., p. \tag{3.64}
$$

For the local trial space $V^k_{h,\hat{K}}$, we choose the tensor product basis

$$\hat{\mathbf{v}}_{cijkl} = l_i(\frac{t-t_k}{|I^K_k|})\boldsymbol{\varphi}_{cjkl}(\hat{x},\hat{y},\hat{z}) \tag{3.65}$$

$$\boldsymbol{\varphi}_{cjkl}(\hat{x},\hat{y},\hat{z}) = L_j(\hat{x})L_k(\hat{y})L_l(\hat{z})\,\mathbf{e}_c$$

$$i = 0,\dots,p_t,\;\; j = 0,\dots,p_x,\;\; k = 0,\dots,p_y,\;\; l = 0,\dots,p_z. \tag{3.66}$$

Thus, the discrete solution can be expanded as $\mathbf{E}_h\Big|_{I^K_k\times K} = DF^{-T}\hat{\mathbf{v}}_{cijkl}e_{cijkl}$, with the coefficients e_{cijkl}.

The basis for the local test-spaces $W^k_{h,\hat{K}}$ consists entirely of Legendre polynomials

$$\hat{\mathbf{w}}_{cijkl} = L_i(\frac{t-t_k}{|I^K_k|})\boldsymbol{\varphi}_{cjkl}(\hat{x},\hat{y},\hat{z}) \tag{3.67}$$

$$\boldsymbol{\varphi}_{cjkl}(\hat{x},\hat{y},\hat{z}) = L_j(\hat{x})L_k(\hat{y})L_l(\hat{z})\,\mathbf{e}_c$$

$$i = 0,\dots,p_t-1, j = 0,\dots,p_x, k = 0,\dots,p_y, l = 0,\dots,p_z. \tag{3.68}$$

3.3.2 Efficient Evaluation of the Space-Time Residual

In this section we discuss the complexity of evaluating the space-time residual (3.63). For affine elements and element-wise constant materials we obtain an optimal complexity of $\mathcal{O}(p^4)$ for each space-time element and for non-affine elements we get a complexity of $\mathcal{O}(p^5)$. For simplicity, we assume isotropic polynomial degrees $p_t = p_x = p_y = p_z = p$ within each space-time element. Furthermore, we employ index notation and summation convention.

Time-Derivative Residual

Using the tensor product structure of the basis, the space-time integral can be rewritten as

$$R^m_E(\mathbf{v}) = \int_{I^K_n}\int_K \varepsilon\partial_t\mathbf{E}_h\cdot\mathbf{v}\,\mathrm{d}x\,\mathrm{d}t = \int_{I^K_n}\int_K \varepsilon\partial_t DF^{-T}\hat{\mathbf{v}}_{cijkl}\cdot DF^{-T}\hat{\mathbf{v}}_{dmnpq}\,\mathrm{d}x\,\mathrm{d}t\,e_{dmnpq}$$

$$= \int_{I^K_k} L_i(\xi)\partial_t l_m(\xi)d\xi\,\mathcal{M}_{cjkl,dnpq}\,e_{dmnpq},$$

$$\mathcal{M}^{\varepsilon}_{cjkl,dnpq} = \int_{\hat{K}} \varepsilon DF^{-T}\boldsymbol{\varphi}_{cjkl}(\hat{x},\hat{y},\hat{z})DF^{-T}\boldsymbol{\varphi}_{dnpq}(\hat{x},\hat{y},\hat{z})|J|d\hat{x}d\hat{y}d\hat{z}.$$

There holds $\int_0^1 L_i(\xi)\partial_t l_m(\xi)d\xi = \delta_{im}$ for $i > 1, m > 1$ by definition (3.64) and the orthogonality of the Legendre polynomials. Thus, the time derivative term can be evaluated by applying a spatial mass matrix $\mathcal{M}_{cjkl,dnpq}$ $\mathcal{O}(p)$ times. One application of $\mathcal{M}_{cjkl,dnpq}$ has a complexity of $\mathcal{O}(p^3)$ operations for affine elements with constant material parameters and a complexity of $\mathcal{O}(p^4)$ operations for non-affine elements, when fast-summation techniques are employed (see [13, 42]). Thus, we obtain a total complexity of $\mathcal{O}(p^4)$ and $\mathcal{O}(p^5)$ operations respectively.

Curl Residual

$$R_H^c(\mathbf{v}) = \int_{I_n^K} \int_K \nabla \times \mathbf{E}_h \cdot \mathbf{v} \, \mathrm{d}x \, \mathrm{d}t \quad R^{curl}_{dmnpq} = \int\limits_{I_k^K} L_i(\xi) l_m(\xi) d\xi \, \mathcal{C}^{vol}_{cjkl,dnpq} \, e_{dmnpq}$$

$$\mathcal{C}^{vol}_{cjkl,dnpq} = \int_{\hat{K}} \varphi_{cjkl}(\hat{x},\hat{y},\hat{z}) \cdot \nabla \times \varphi_{dnpq}(\hat{x},\hat{y},\hat{z}) d\hat{x} d\hat{y} d\hat{z}$$

For $m > 2$ we have $l_m(\xi) = (L_{m+1}(\xi) - L_{m-1}(\xi))/\sqrt{(}2m+1)$, such that the discrete curl operator $\mathcal{C}^{vol}_{cjkl,dnpq}$ is applied $\mathcal{O}(p)$ times. Each application of the discrete curl can be done with $\mathcal{O}(p^3)$ operations using recurrence relations of the Legendre polynomials [35]. This leads to a total complexity of $\mathcal{O}(p^4)$ operations.

Flux Terms

In the following we discuss how the flux terms can be evaluated with a complexity of $\mathcal{O}(p^4)$ operations. We consider the evaluation of a coupling flux term, which has to be evaluated at the interface $f_t \times f_s, f_t = I^1 \cap I^2, f_s = \partial K^1 \cap \partial K^2$ of two space-time elements $I^1 \times K^1$, $I^2 \times K^2$. We emphasize, that the interface can be nonconforming in space and also in time.
There holds $K^i = F_i([0,1]^3), I^i = \tau_i([0,1])$ and we employ a co-variant transform for the fields, such that we have

$$R_H^f(\mathbf{v}) = \int_{f_t} \int_{f_s} \mathbf{E}_h^2 \cdot (\mathbf{n}^1 \times \boldsymbol{\pi}_{\tilde{T}f} \mathbf{v}^1) \, \mathrm{d}S \, \mathrm{d}t =$$
$$\int_{\tau_1{}^{-1}(f_t)} \int_{F_1{}^{-1}(f_s)} DF_1{}^T DF_2{}^{-T} \circ \psi_1^2 \hat{\mathbf{E}}_h^2 \circ \psi_1^2 \cdot (\hat{\mathbf{n}}^1 \times \boldsymbol{\pi}_{\tilde{T}f} \hat{\mathbf{v}}^1) \, \mathrm{d}\hat{x} \, \mathrm{d}\hat{y} \, \mathrm{d}\hat{t}. \tag{3.69}$$

In (3.69) we denote by $\psi_1^2 : {\tau_1}^{-1}(I^1) \times {F_1}^{-1}(f_s) \to {\tau_2}^{-1}(I^2) \times {F_2}^{-1}(f_s)$ the mapping from the reference coordinates of $I^1 \times K^1$ to those of $I^2 \times K^2$. The mappings ψ_1^2 and $DF_1^T DF_2^{-T}$ are constant for each face, see for the spatial part [12]. Both mappings are in general affine and the matrix is a scaled permutation matrix. The scaling in turn is different from the identity matrix in the case of non-conforming interfaces. For simplicity, in the following we assume that no coordinate permutations occur, i.e. we can write ψ_1^2 as $(\hat{x}^2, \hat{y}^2, \hat{z}^2, \hat{t}^2) = (s_x \hat{x}^1 + b_x, s_y \hat{y}^1 + b_y, s_z \hat{z}^1 + b_t, s_t \hat{t}^1 + b_t)$. There holds for a face with normal $\hat{\mathbf{n}}^1 = \mathbf{e}_3$ in reference coordinates

$$\hat{\mathbf{E}}_h^2 = l_i(\hat{t}) L_j(\hat{x}) L_k(\hat{y}) L_l(-1) e_{cijkl} \mathbf{e}_c = l_i(\hat{t}) L_j(\hat{x}) L_k(\hat{y}) e^F_{cjkl} \mathbf{e}_c. \tag{3.70}$$

We can compute the coefficients $e^F_{cijk} = L_l(-1) e_{cijkl}$ with an operation count of $\mathcal{O}(p^4)$. Using $I_{\hat{t}} = \tau_1^{-1}(f_t)$ and $I_{\hat{x}} \times I_{\hat{y}} = F_1^{-1}(f_s)$, employing the tensor product structure of the basis functions $\hat{\mathbf{v}}_{cijkl}$ and $\hat{\mathbf{w}}_{dmnop}$ we can factor (3.69) as

$$\begin{aligned} R^{flux}_{dmnop} &= L_p(1) [\boldsymbol{\pi}_{\tilde{T}f}]_{mq} \int_{I_{\hat{t}}} l_i(s_t \hat{t}^1 + b_t) L_q(\hat{t}^1) \, \mathrm{d}\hat{t}^1 \int_{I_{\hat{x}}} L_j(s_x \hat{x}^1 + b_x) L_n(\hat{x}^1) \, \mathrm{d}\hat{x}^1 \\ &\times \int_{I_{\hat{y}}} L_k(s_y \hat{y}^1 + b_y) L_o(\hat{y}^1) \, \mathrm{d}\hat{y}^1 (\hat{\mathbf{n}}^1 \times \mathbf{e}_d) \cdot \mathbf{e}_c e^F_{cijk}. \end{aligned}$$

Using sum-factorization (see [13, 42]), we can evaluate R^{flux}_{dmnop} as follows

$$\begin{aligned} Aux1_{doij} &= \int_{I_{\hat{y}}} L_k(s_y \hat{y}^1 + b_y) L_o(\hat{y}^1) \, \mathrm{d}\hat{y}^1 (\hat{\mathbf{n}}^1 \times \mathbf{e}_d) \cdot \mathbf{e}_c e^F_{cijk} \\ Aux2_{dnoi} &= \int_{I_{\hat{x}}} L_j(s_x \hat{x}^1 + b_x) L_n(\hat{x}^1) \, \mathrm{d}\hat{x}^1 Aux1_{doij} \\ Aux3_{dmno} &= [\boldsymbol{\pi}_{\tilde{T}f}]_{mq} \int_{I_{\hat{t}}} l_i(s_t \hat{t}^1 + b_t) L_q(\hat{t}^1) \, \mathrm{d}\hat{t}^1 Aux2_{dnoi} \\ R^{flux}_{dmnop} &= L_p(1) Aux3_{dmno}. \end{aligned} \tag{3.71}$$

Each summation in (3.71) has a complexity of $\mathcal{O}(p^4)$, when the interface is non-conforming in the corresponding direction. For interfaces which are conforming in a certain direction, the corresponding summation can be skipped due to the orthogonality properties of the trial and test basis functions. Thus, in total we can compute the flux-residual with a complexity of $\mathcal{O}(p^4)$ operations.

3.3.3 Inexact Iterative Solution - Guaranteed Iteration Error Bound

In order to save computational costs, we solve the problem (3.9) inexactly and employ an error estimate for the iteration error.

The iteration error $\mathbf{u}_h - \mathbf{u}_h^m$ at iteration m fulfills

$$B_h^n(\mathbf{u}_h^m - \mathbf{u}_h, \mathbf{w}) = R_h^{m,n}(\mathbf{w}).$$

We can now employ theorem 3.2.3 to get a bound on the error at time t_N

$$\begin{aligned}\|\varepsilon^{\frac{1}{2}}\mathbf{e}^m(t_N)\|^2_{\mathbf{L}^2(\Omega)} + \|\mu^{\frac{1}{2}}\mathbf{h}^m(t_N)\|^2_{\mathbf{L}^2(\Omega)} \leq 4\sum_{n=1}^{N}\Bigg(&(\frac{2t_N}{\underline{\varepsilon}} + \frac{\Delta t^2}{2t_N\underline{\varepsilon}})\|R^{m,n}_{h,E}\|^2_{W_h'} \\ &+(\frac{2t_N}{\underline{\mu}} + \frac{\Delta t^2}{2t_N\underline{\mu}})\|R^{m,n}_{h,H}\|^2_{W_h'}\Bigg) =: \mathcal{E}^2_{it},\end{aligned} \tag{3.72}$$

with $\mathbf{e}^m = \mathbf{E}_h^m - \mathbf{E}_h$ and $\mathbf{h}^m = \mathbf{H}_h^m - \mathbf{H}_h$. We evaluate the dual norm of the residual on the right hand side of (3.72) exactly by computing the Riesz-representor. This corresponds to the application of an L^2-projection and can be done in parallel for all elements due to the discontinuous test space.

Finally, we note that the iteration error bound (3.72) is free of unknown constants and therefore guaranteed.

3.3.4 Remarks on the Iterative Solution Procedure

The linear systems governed by (3.14) are non-symmetric in general. For their solution we employ a preconditioned GMRES solver with restarting after n_r iterations, which leads to a memory consumption of essentially $n_r \times N$, where N is the number of degrees of freedom. In most cases, we choose $n_r = 10$.

For preconditioning we employ the time-derivative terms in (3.14)

$$P(\mathbf{u}_h, \mathbf{w}) := \int_{\mathcal{I}_n}\int_{\Omega} \varepsilon\partial_t \mathbf{E}_h \cdot \mathbf{w}_E \,\mathrm{d}x\,\mathrm{d}t + \int_{\mathcal{I}_n}\int_{\Omega} \mu\partial_t \mathbf{H}_h \cdot \mathbf{w}_H \,\mathrm{d}x\,\mathrm{d}t. \tag{3.73}$$

The preconditioner (3.73) is at most block-diagonal with block size $3(p_x+1)(p_y+1)(p_z+1)$. Moreover, in the important special case of affine elements a diagonal preconditioner is obtained. Thus, recalling the complexity analysis in the previous sections, one preconditioned GMRES iteration leads to computational costs per spatial element K similar to N_K time-steps of an explicit Runge-Kutta scheme with p_t stages.

Finally, it should be emphasized that the preconditioner (3.73) is efficient only for sufficiently small Δt because the terms in (3.14) which are neglected in (3.73) scale with Δt.

p	steps	N_{it}	$\widetilde{N}_{it}$	$N_{it}/\widetilde{N}_{it}$	$e(T)$	$\widetilde{e}(T)$	I_{eff}
1	189	7.9	4.0	2.0	2.04×10^{-1}	2.04×10^{-1}	1.7
2	315	24.0	6.1	4.0	3.65×10^{-3}	3.90×10^{-3}	3.1
3	220	25.0	6.0	4.2	5.57×10^{-3}	5.31×10^{-3}	6.8
4	283	20.0	7.8	2.6	2.30×10^{-4}	2.26×10^{-4}	12.6
5	213	22.0	8.6	2.5	1.91×10^{-4}	1.83×10^{-4}	5.7
6	252	18.0	8.8	2.0	4.84×10^{-5}	4.83×10^{-5}	5.7

Table 3.1: Number of time-steps, average number of GMRES-iterations N_{it} per time-step for exact and $\widetilde{N}_{it}$ for inexact solution of the linear systems, speedup $N_{it}/\widetilde{N}_{it}$, errors $e(T) = \|\mathbf{u}(T) - \mathbf{u}_h(T)\|_{\mathrm{L}^2(\Omega)}$ and $\widetilde{e}(T) = \|\mathbf{u}(T) - \widetilde{\mathbf{u}}_h(T)\|_{\mathrm{L}^2(\Omega)}$ for exact and ineaxct solution and efficiency index for the iteration error bound (3.72) $I_{eff} = \mathcal{E}_{it}/\|\mathbf{e}_h^n(T) - \mathbf{e}_h(T)\|_{\mathrm{L}^2(\Omega)}$

Example

For illustrating the computational costs of the iterative solution process, we simulate a T_{mm}-mode in a resonator and report the number of iterations and errors for exact and inexact iterative solution in table 3.1.

The computational domain is defined as $\Omega := [0,1]^3$ and discretized with 8×8×8 hexahedral elements. We choose uniform polynomial degrees $p = p_t = p_x = p_y = p_z$. The time step is choosen as $\Delta t = h/(2p+1)$, which is the maximal stable time step for a SSP low-storage Runge-Kutta method of order $p+1$ [60]. We set the wavenumber m to 1 for $p = 1,2$, to 2 for $p = 3,4$ and to 3 for $p = 5,6$. In table 3.1 the number of iterations required for solving the linear systems within a tolerance of 10^{-14} is about $N_{it} = 20 - 30$ per time-step. Compared to an explicit method, where the computational costs are roughly equal to one iteration, the costs are prohibitively high. However, the number of iterations $\widetilde{N}_{it} = 4 - 9$ for inexact solution is reduced by a factor of 2-4.2 and the associated iteration errors are consistently overestimated by factors of 2-12, such that the total accurracy is not compromised by the inexact iterative solution process.

3.4 Numerical Experiments

In this section we present the numerical experiments from [40]. The first part of this section is devoted to basic convergence tests on non-adaptive discretizations.

In the second part, we carry out numerical experiments on fully space-time hp-adaptive discretizations.

3.4.1 Convergence Tests on Non-Adaptive Discretizations

TM Mode hp-Discretization

We choose the computational domain as $\Omega = [0,1] \times [0,1] \times [0,1/5]$ and set the initial data, boundary conditions and source such that we approximate a TM_{11}-mode. Further, we set $\varepsilon = \mu = 1$. The exact solution for the electric field is,

$$\mathbf{E} = \sin(\pi x)\sin(\pi y)\cos(\omega t)\mathbf{e}_z, \tag{3.74}$$

with angular frequency $\omega = \pi\sqrt{m^2+n^2}$. For the discretization visualized in Fig. 3.3, we show in Fig. 3.4 (left) the time traces of the $\mathbf{L}^2(\Omega)$-error for 200 periods for $p_{min} = 1,2,3,4$. In Fig. 3.4 (right) we depict the exponentially converging error measured in the $\|\cdot\|_{L^2(\mathcal{I}_n;\mathbf{L}^2(\Omega))}$-norm.

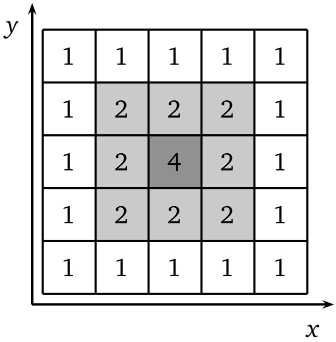

1	1	1	1	1
1	2	2	2	1
1	2	4	2	1
1	2	2	2	1
1	1	1	1	1

Figure 3.3: The discretization in the $x-y$-plane. The numbers inside the elements of the spatial mesh are equal to the number of local time steps. We choose the polynomial degrees isotropically $p_t = p_x = p_y = p_z = p$ increasing from p_{min} at the boundary to $p_{min}+2$ the center of the discretization, corresponding to the shading.

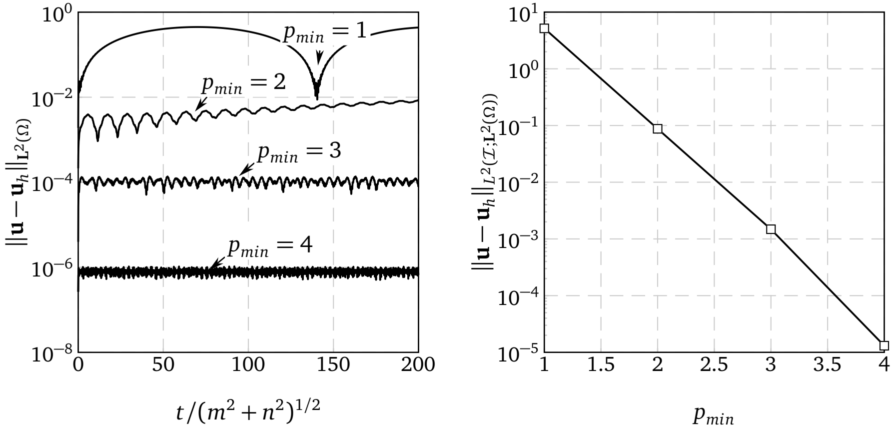

Figure 3.4: Left: Time traces of the error measured in the $\|\cdot\|_{\mathbf{L}^2(\Omega)}$-norm. Right: Error measured in the $\|\cdot\|_{L^2(\mathcal{I};\mathbf{L}^2(\Omega))}$-norm. Both for $p_{min}=1,2,3,4$ and the setup from Fig. 3.3

Local h-Refinement in Time

In this section we discuss the convergence of the temporal part of the error, when local h-refinement in time is present in the discretization. To this end we choose initial conditions, boundary conditions and sources such that we approximate the exact solution [65]

$$\begin{aligned}\mathbf{E} &= e^t x(x-1)z(1-z)\mathbf{e}_y,\\ \mathbf{H} &= e^t x(x-1)(1-2z)\mathbf{e}_x - e^t(2x-1)z(1-z)\mathbf{e}_z\end{aligned}$$

in the space-time domain $\mathcal{I}\times\Omega$ with $\mathcal{I}=[0,5], \Omega=[0,1]^3$ and $\varepsilon=\mu=1$. We decompose the space-time domain in time slabs $\Delta t\times\Omega$. We depict the spatial mesh and the temporal refinement level in Fig. 3.5. Since we are interested in the temporal part of the error, we choose the polynomial degrees in the spatial directions as $p_x=p_z=2$ and $p_y=0$. Thus, the temporal part of the error should be dominating. In Fig. 3.6 (left), we show the error in the $\|\cdot\|_{L^2(\mathcal{I};\mathbf{L}^2(\Omega))}$-norm under Δt-refinement for $p_t=1,2,3,4,5$ and obtain convergence orders of p_t+1. In Fig. 3.6 (right), we depict the convergence of the quantity $\max\limits_k \|\mathbf{u}(t_k)-\mathbf{u}_h(t_k)\|_{\mathbf{L}^2(\Omega)}$

for the same setup and obtain orders of $2p_t$. For continuous-Galerkin (cG) time stepping schemes, this nodal superconvergence behavior is reported in [2, 68].

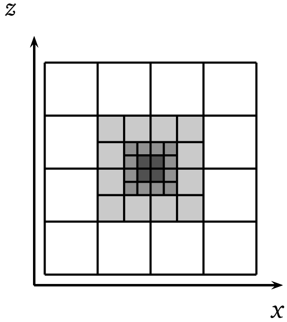

Figure 3.5: Spatial mesh with temporal refinement level. The temporal refinement level increases according to the shading from 0 at the boundary to 3 at the center of the spatial domain.

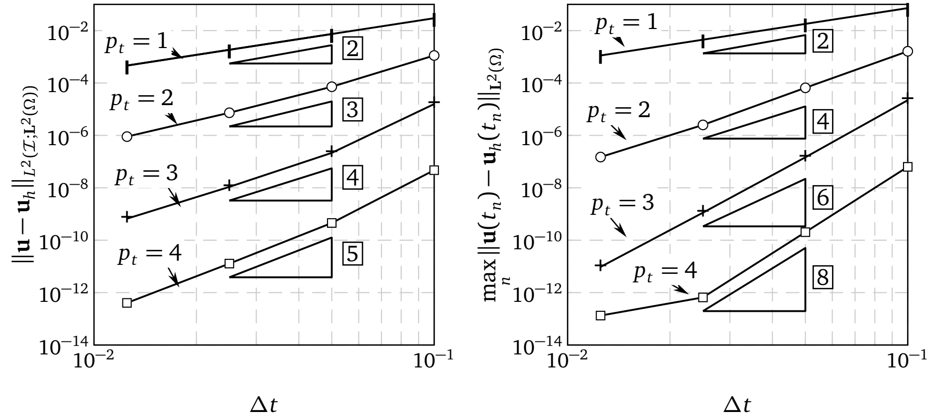

Figure 3.6: Left: error $\|\mathbf{u}-\mathbf{u}_h\|_{L^2(\mathcal{I};\mathbf{L}^2(\Omega))}$, right: error $\max_k \|\mathbf{u}(t_k)-\mathbf{u}_h(t_k)\|_{\mathbf{L}^2(\Omega)}$ for the local h-refinement with respect to time depicted in Fig.3.5

Broadband Pulse in a Coaxial Waveguide

We consider the propagation of a broadband pulse in a coaxial waveguide with $\varepsilon = \mu = 1$. Denoting with r, φ and z the radial, azimuthal and axial coordinates of a cylindrical coordinate system, the computational domain is given, by $4 \leq r \leq 10$, $-\pi \leq \varphi \leq \pi$ and $-50 \leq z \leq 50$. The boundary condition at the lower end of the waveguide ($z = -50$) is chosen as $\mathbf{n} \times \mathbf{E}_h = \mathbf{n} \times \mathbf{E}$. At the upper end ($z = 50$) we apply a Silver-Mueller boundary condition and on the remaining part of the boundary we apply the PEC condition $\mathbf{n} \times \mathbf{E}_h = 0$. The exact solution for the problem is

$$\mathbf{E} = \frac{1}{r} e^{-(\pi(f_2 - f_1)(z-t)/2)^2} \sin(\pi(f_1 + f_2)(z - t))\mathbf{e}_r, \tag{3.75}$$

$$\mathbf{H} = \frac{1}{r} e^{-(\pi(f_2 - f_1)(z-t)/2)^2} \sin(\pi(f_1 + f_2)(z - t))\mathbf{e}_\varphi, \tag{3.76}$$

where $\mathbf{e}_r$, $\mathbf{e}_\varphi$ and $\mathbf{e}_z$ denote the corresponding unit vectors. We set $f_c = (f_1 + f_2)/2$ in (3.75) to $f_c = 3/20$. Thus, the wavelength λ is about 1/16-th of the length of the coaxial waveguide. We decompose the spatial domain in 1600 hexahedra which leads to an edge length of approximately $\lambda/3$. We set $\Delta t = 1/4$ and $T = 80$. The temporal evolution of the error measured in the $\|\cdot\|_{\mathrm{L}^2(\Omega)}$-norm is depicted in Fig. 3.7. The error shows an odd even pattern, the origin of which is likely to be related to the choice of a central flux. A similar behavior is reported in [28].

Bi-Static RCS, Metallic Sphere - Global p-Refinement

We illuminate a PEC-sphere with radius $a = 1$ by a $\mathbf{e}_x$-polarized time-harmonic plane wave $\mathbf{E}_{inc} = \sin(\mathbf{e}_z \cdot \mathbf{x} - \omega t)\mathbf{e}_x$ propagating in $\mathbf{e}_z$-direction. The angular frequency is $\omega = 2\pi$. We employ the scattered field formulation (2.11) and choose Ω as a spherical shell with outer radius $R = 5$. Further, we choose $\varepsilon = \mu = 1$. We decompose the spatial domain Ω into 576 hexahedral elements such that the elements have an edge-length of approximately $\lambda/2$ at the surface of the scatterer and an edge length of about λ at the absorbing boundary. We set the polynomial degrees uniformly to $p = p_t = p_x = p_y = p_z = p_{\mathrm{geo}}$. Here, p_{geo} denotes the polynomial degree of the mapping F from the reference to the physical element. We evaluate the bi-static RCS (2.12) and evaluate the far field integral (2.13) using Gauss quadrature of sufficiently high order on a closed surface S which is one wavelength away from the surface of the scatterer. In Fig. 3.8 we depict the RCS obtained for $p = 2, \dots, 6$ together with a Mie-series solution (red line) for reference.

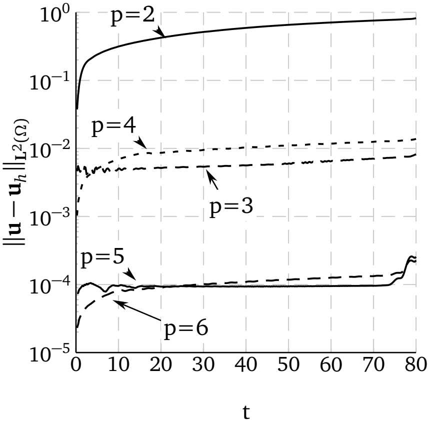

Figure 3.7: Time traces of the error measured in the $\|\cdot\|_{L^2(\Omega)}$-norm for $p = 2, 3, 4, 5, 6$.

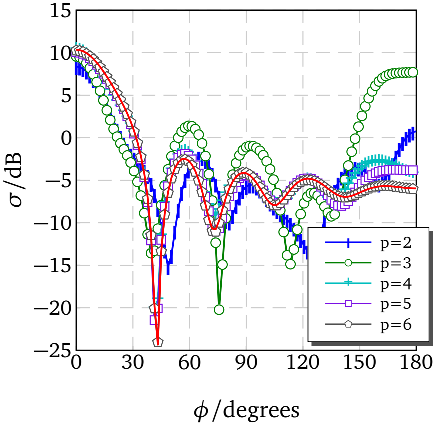

Figure 3.8: Bi-static RCS, of a PEC sphere with $ka = 2\pi$, numerical solutions for a 576-element mesh with polynomial degrees $p = 2, \ldots, 6$ and the analytical Mie-series solution (red line)

3.4.2 Space-Time hp-Adaptive Examples

In this section we demonstrate that the developed method can be employed within a fully automatic space-time hp-adaptive algorithm. To this end, we first present an adaptive algorithm based on the concept of reference solutions [13, 59]. The material in this section is published in [40].

- Choose a global time step Δt. This leads to a partitioning of the space-time domain in equally sized time slabs.

- Given a time slab $\Delta t \times \Omega$, choose an initial mesh $\mathcal{S}_0$ and polynomial degree distribution $\mathbf{p}_0$.

- Choose a coarse discretization $(\mathcal{S}_H, \mathbf{p}_H) = (\mathcal{S}_0, \mathbf{p}_0)$ with finite element space $\mathbf{V}_H^n$. Construct a refined discretization $(\mathcal{S}_h, \mathbf{p}_h)$ by isotropically refining all space time elements and increasing all polynomial degrees by one. We denote the refined finite element space, which contains the coarse space, with $\mathbf{V}_h^n$.
  Now, we iteratively perform

  1. SOLVE: Solve the problem (3.9) using the coarse and fine discretizations $\mathbf{V}_H^n$ and $\mathbf{V}_h^n$, respectively.
  2. ESTIMATE: Evaluate the error indicators $\mathcal{E}^2(\mathcal{I}_n \times K) = \|\mathbf{u}_h - \mathbf{u}_H\|^2_{L^2(\mathcal{I}_n;\mathbf{L}^2(K))}$. If $\|\mathbf{u}_h - \mathbf{u}_H\|_{L^2(\mathcal{I}_n;\mathbf{L}^2(\Omega))} \leq TOL$ stop and proceed to the next time slab. Otherwise continue with MARK.
  3. MARK: Using the indicators $\mathcal{E}(\mathcal{I}_n \times K)$, mark space-time macro elements $\mathcal{I}_n \times K$ for refinement/derefinement. We employ a fixed fraction marking strategy [16].
  4. REFINE: Given a marked $\mathcal{I}_n \times K$, we create a set of refinement candidates $V^{\text{cand}}_{H,\mathcal{I}_n \times K}(\mathcal{I}_n \times \hat{K}, \mathbf{p}_K)$. The set of candidates, contains all combinations of the following modifications

     - increase/decrease the polynomial degrees p_x, p_y, p_z, p_t
     - isotropically h-refine/derefine in the spatial directions
     - increase/decrease the temporal refinement level

     If the refinement leads to new space-time elements, we reduce the number of candidates by choosing the same polynomial degrees for all newly created elements.

Now, we select the “best" candidate according to

$$V_{H,\mathcal{I}_n \times K} = \underset{V_H^{\text{cand}} S.T. \mathcal{E} - \mathcal{E}^{\text{cand}} > 0}{\arg\min} \frac{\mathcal{E}^{\text{cand}} - \mathcal{E}}{\#DOF(V_H^{\text{cand}})},$$

$$\mathcal{E}^{\text{cand}} = \|\mathbf{u}_h - \Pi_{V_h}^{V_H^{\text{cand}}} \mathbf{u}_h\|_{L^2(\mathcal{I}_n;\mathbf{L}^2(\Omega))}.$$

Thus, we obtain a new global coarse finite element space $\mathbf{V}_H^n$, create a new refined space $\mathbf{V}_h^n$ and go to SOLVE.

- At this point, the coarse- and fine-grid solutions are computed for the time slab $\mathcal{I}_n \times \Omega$ and we continue with the next time slab.

Remark1: For the coarse and fine-grid solutions at time-slab n we choose as initial-data the L^2-projection of the fine-grid solution from time-slab $n-1$.
Remark2: The number of linear solver iterations for the fine-grid solve can be significantly reduced, if the coarse grid solution is employed as an initial guess.

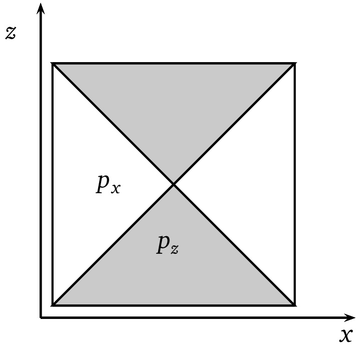

Figure 3.9: Tensor product visualization for polynomials with degrees p_x,p_z

Broadband Pulse in a Coaxial Waveguide

We again simulate the coaxial waveguide from section 3.4.1, but this time with the space-time hp-adaptive algorithm. The initial spatial mesh employed for each time slab contains only 200 elements and the polynomial degrees are set uniformly to $p_t = 1, p_x = p_y = p_z = 0$. We set the degree of the element transformation at curved boundaries to $p_{\text{geo}} = 4$ and in the interior of the computational domain to $p_{\text{geo}} = 1$. Moreover, we set $T = 80$ and choose the global time step as $\Delta t = 1/2$. We depict the electric field magnitude $|\mathbf{E}_h|$, the spatial polynomial degree distribution and the temporal polynomial degree distribution of the final coarse-grid discretization of time slab 73 in Fig. 3.10. We observe, that refinement is concentrated in the area of the pulse and that the hp-algorithm chooses mostly p refinement with higher spatial polynomial degrees in axial direction than in radial direction. This reflects the nature of the exact solution, which is smooth and features a greater variation in axial direction than in the radial and circumferential directions. Further, we note that the temporal refinement level was never raised. The relative fine grid error measured in the $\|\cdot\|_{L^2(\mathcal{I};\mathbf{L}^2(\Omega))}$ is $9.6 \cdot 10^{-3}$.

Scattering from a Dielectric Sphere

A dielectric sphere with radius $a = 1$ is illuminated by a plane-wave with Gaussian shape

$$\mathbf{E}_{inc} = e^{-(\mathbf{e}_x \cdot \mathbf{x} - t - 4)^2} \mathbf{e}_z, \quad \mathbf{H}_{inc} = \mathbf{e}_x \times \mathbf{E}_{inc}.$$

We choose the relative electric permittivity and magnetic permeability of the scatterer as $\varepsilon = 4$ and $\mu = 1$, respectively. Further, in fee space we set $\varepsilon = \mu = 1$. The scatterer is embedded in a sphere of radius $R = 5$ and we compute the scattered fields using the scattered field formulation (2.11). We set $T = 80$ and the global time step as $\Delta t = 1/10$. The initial mesh for each time slab consists of only 72 elements and the initial polynomial degrees are chosen uniformly as $p_t = 1, p_x = p_y = p_z = 0$. For an accurate representation of the curved surfaces we set $p_{\text{geo}} = 4$ at the surface of the dielectric sphere and at the absorbing boundary. In Fig. 3.11 we show the electric field magnitude and the discretizations obtained with the hp-adaptive algorithm for time slabs 33, 65 and 124. Inspecting the spatial discretization, we observe that moderate polynomial degrees and a rather fine mesh are chosen at the material interface. Here, the fields have only limited regularity. Away from the interface, where the solution is smooth, the algorithm chooses high polynomial degrees and a larger mesh size. With respect to time, local h-refinement is dominating. Since the temporal polynomial degree p_t was essentially never modified, we do not show the corresponding polynomial degree distributions. We show the obtained bi-static RCS for $ka = 1$, where k denotes the wavenumber, together with a Mie-solution for reference in Fig. 3.12. The rela-

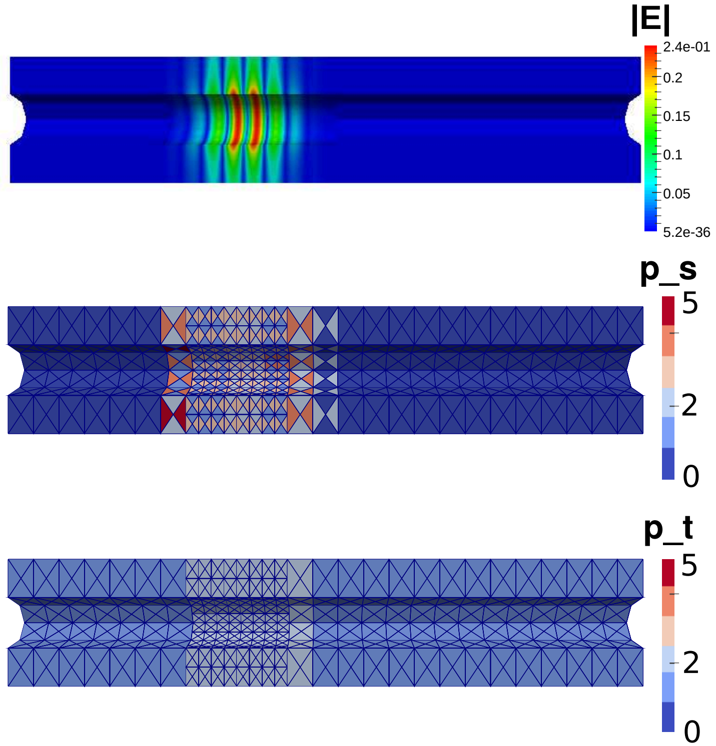

Figure 3.10: hp-adaptive simulation of a broadband pulse in a coaxial waveguide at time slab 73. From top to bottom: distribution of the electric field magnitude $|\mathbf{E}_h|$, the spatial polynomial degrees (p_x, p_y, p_z), and the temporal polynomial degree p_t.

tive error of the bi-static RCS for $0 \leq \theta_i \leq \pi$ measured in the 2-norm is $2.53 \cdot 10^{-2}$, i.e.

$$\frac{\left(\sum_{i=1}^{200} (\sigma(\theta_i) - \sigma_h(\theta_i))^2\right)^{\frac{1}{2}}}{\left(\sum_{i=1}^{200} \sigma(\theta_i)^2\right)^{\frac{1}{2}}} = 2.53 \cdot 10^{-2}.$$

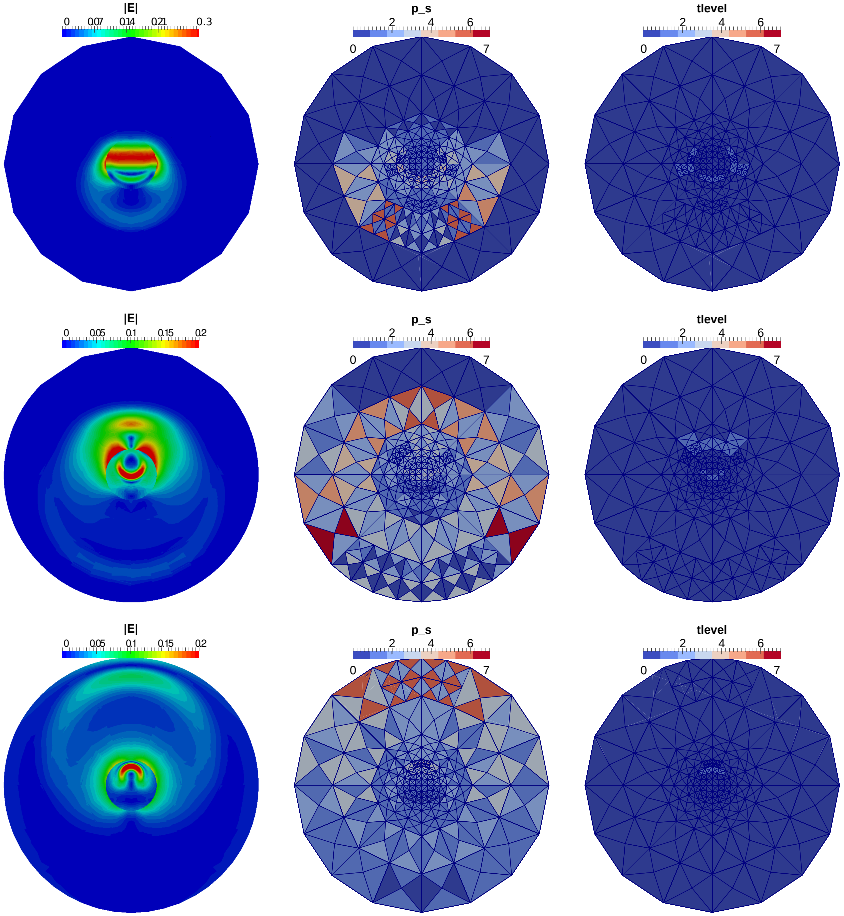

Figure 3.11: Scattered field from a dielectric sphere and the corresponding discretization, obtained with the hp-adaptive algorithm for timeslabs 34, 66, 125 (from top to bottom). From left to right: electric field magnitude $|\mathbf{E}_h|$, spatial polynomial degrees (p_x, p_y, p_z) and temporal refinement level.

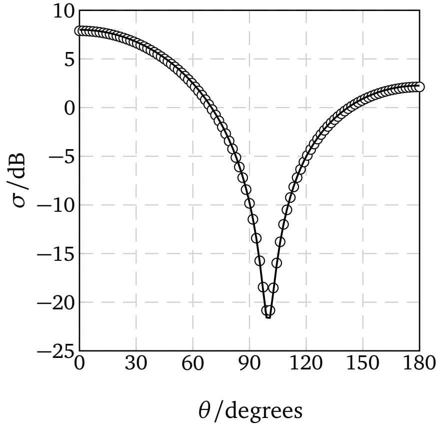

Figure 3.12: Bistatic RCS of a dielectric sphere with $\varepsilon = 4$ and ka=1. Here, k denotes the wavenumber and a the radius of the sphere. Discrete solution (black circles), Mie-series solution (black line).

3.5 Conclusions

We have presented a space-time Galerkin method which combines a discontinuous Galerkin approach in the spatial directions with a continuous Galerkin approach in the temporal direction. The resulting method naturally allows for local *hp*-refinement in space and in time. Furthermore, it can be demonstrated that the method is non-dissipative, provided a centered flux is chosen and the spatial discretization is not changed during the simulation. We have described how the arising linear systems of equations can be solved iteratively, without the need of assembling and storing global or local element matrices. Since an efficient residual evaluation is particularly important in order to cut down computation times in practice, we have demonstrated that the residual can be evaluated directly with complexities of $\mathcal{O}(p^4)$ for affine elements and $\mathcal{O}(p^5)$ operations for non affine elements. This was achieved by employing fast-summation techniques, which are an established tool for the implementation of high-order finite element methods [9, 13, 35, 42].

Furthermore, for discretizations not containing local refinement with respect to time, we have carried out the fully discrete *a priori* error analysis, being explicit in the spatial- and temporal mesh size as well as in the degrees of the approximating polynomials. The analysis extents results for an *h*-version HDG discretization for the wave equation [20] to the presented *hp*-discretization for Maxwell's equations. Under the same assumption, we have established a guaranteed *a posteriori* bound on the iteration error. For a test-problem, the estimate was shown to overestimate the actual error consistently by factors between 1.5 and 12. The obtained bound on the iteration error can be employed for the purpose of balancing iteration and discretization errors.

While the computational costs of the space-time Galerkin method are higher than those of explicit *hp*-DG methods such as [56, 57], it allows to apply *hp*-adaptivity also in time. Thus, it provides the possibility for controlling the discretization error in the entire space-time domain.

Future work should be directed towards the extension of the *a priori* error analysis to the general case of local refinement in time and the development of more efficient methods for the iterative solution of the linear systems.

4 Extension to Waveguide Problems

For many technical applications it is required to guide electromagnetic fields, e.g. in antenna feeding. As rectangular or circular waveguides are very commonly applied for this purpose, their numerical modeling is of high practical importance. For volume discretization schemes this amounts to the truncation of the computational domain at so called waveguide ports. On the one hand, waveguide ports have to absorb outgoing waves with as little reflection as possible, and on the other hand they have to allow guiding fields into the computational domain. The latter requires the two-dimensional field distribution at the waveguide port to fulfill Maxwell's equations, i.e. be a superposition of waveguide modes.

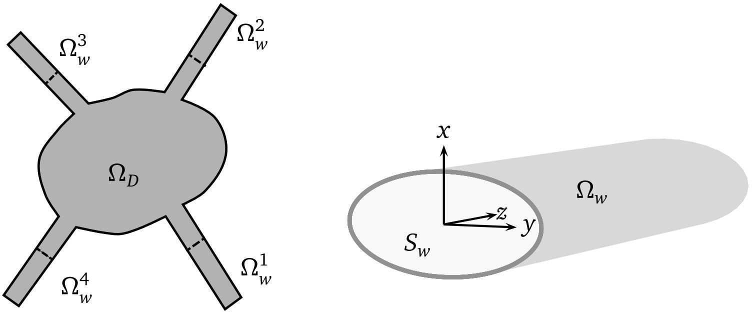

Figure 4.1: Left: Computational domain Ω consisting of Ω_D and 4 waveguide subdomains Ω_w^i, right: waveguide subdomain Ω_w^i

The absorption of outgoing waves can be achieved, e.g., by applying Silver-Mueller boundary conditions. Unfortunately, the application of first order Silver-Mueller boundary conditions can lead to significant reflection at waveguide boundaries, such that reflected waves propagate back into the computational domain and lead to a large modeling error. This is also the case when some perfectly matched layer (PML) formulations are employed to absorb outgoing waves containing modes with frequencies near the cut-off frequency.

One approach, which leads to an effective absorption of outgoing modes at all frequencies, is the application of an inhomogeneous boundary condition with analytical solutions [41]. Here the waveguide fields are decomposed in their temporal-longitudinal and transversal parts. The transversal parts can be computed either analytically or numerically from an eigenvalue problem on the cross-section. The remaining part is the solution to a time-dependent PDE in one dimensional space, which can be solved analytically. However, this approach makes it necessary to compute convolutions of the discrete solution with Bessel functions, in each time step.

Yet another approach presented in [50] instead employs discrete solutions to the 1D PDE , which are obtained with a DG method. This leads to a coupled 3D-1D problem with two additional 1D PDEs for each considered mode. However, no stability and convergence analysis is available for this method.

In this work, a similar approach to [50] is adopted. Instead of discretizing the coupled 3D-1D problem, the waveguide parts of the three-dimensional computational domain are extended, such that a PEC boundary condition can be applied at their ends. The solution is approximated by tensor-product basis functions, consisting of waveguide-modes in transversal directions and polynomials in longitudinal and time-directions. This approach is a natural extension of the space-time discontinuous Galerkin method presented in chapter 3, inheriting its arbitrary high order of accurracy in space and time. Further it allows for an extension of the *a priori* and *a posteriori* analysis presented in chapters 3 and 5. It is also noteworthy, that the additional computational effort associated with the waveguide parts corresponds to that of a single 1D problem for each waveguide subdomain and each considered mode.

4.1 Waveguide Solutions

We consider problems, where one or more subdomains of the computational domain Ω are homogeneous waveguides. The situation is depicted in Fig. 4.1. For simplicity, in the following section we consider the case of one waveguide subdomain i.e. $\Omega = \Omega_D \cup \Omega_w$. Here, $\Omega_w = S_w \times \mathcal{I}_w$ where S_w denotes the cross-section. We assume that $\mathcal{I}_w$ is aligned with the $\mathbf{e}_z$-axis. Solutions of Maxwell's equations in a homogeneous waveguide with non-varying cross-section can be represented as a series of transverse magnetic ($\nu = \mathrm{TM}$) and electric modes ($\nu' = \mathrm{TE}$) by employing a separation ansatz [37]

$$\begin{aligned}
\mathbf{E}(\mathbf{x},t) &= \sum_{n}^{\infty} \mathbf{e}_{n\nu'}(x,y) f_{n\nu'}(z,t) + \sum_{m}^{\infty} \left[\mathbf{e}_{m\nu}(x,y) g_{m\nu,t}(z,t) + v_m(x,y) h_{m\nu}(z,t) \mathbf{e}_z \right] \\
\mathbf{H}(\mathbf{x},t) &= \sum_{m}^{\infty} \mathbf{h}_{m\nu}(x,y) f_{m\nu}(z,t) + \sum_{n}^{\infty} \left[\mathbf{h}_{n\nu'}(x,y) g_{n\nu',t}(z,t) + w_n(x,y) h_{n\nu'}(z,t) \mathbf{e}_z \right].
\end{aligned} \tag{4.1}$$

For the transverse fields, denoting by $\nabla_T = \nabla - \partial_z$ and $\Delta_T = \Delta - \partial_{zz}$, there holds

$$\mathbf{e}_{m\nu}(x,y) = \nabla_T v_m(x,y) \qquad \mathbf{h}_{m\nu}(x,y) = \mathbf{e}_z \times \nabla_T v_m(x,y) \tag{4.2}$$

$$\mathbf{e}_{n\nu'}(x,y) = -\mathbf{e}_z \times \nabla_T w_n(x,y) \qquad \mathbf{h}_{n\nu'}(x,y) = \nabla_T w_n(x,y), \tag{4.3}$$

where $v_m(x,y), w_n(x,y)$ are solutions of the Dirichlet (TM) and Neumann (TE) eigenvalue problems

$$\begin{aligned}
&\Delta_T v_m + \lambda_{m\nu}^2 v_m = 0 \ \text{ in } S_w && \Delta_T w_n + \lambda_{n\nu'}^2 w_n = 0 \ \text{ in } S_w \\
&v_m = 0 \ \text{ on } \partial S_w && \mathbf{n} \cdot \nabla_T w_n = 0 \ \text{ on } \partial S_w.
\end{aligned} \tag{4.4}$$

Further, for $\lambda_{m\nu} > 0, \lambda_{m\nu'} > 0$, following [37], we normalize the eigenfunctions as

$$\int_{S_w} v_n \, v_m \, dS = \lambda_{n\nu}^{-2} \delta_{nm} \qquad \int_{S_w} w_n, w_m \, dS = \lambda_{n\nu'}^{-2} \delta_{nm}, \tag{4.5}$$

leading to

$$\int_{S_w} \mathbf{e}_{m\nu} \mathbf{e}_{n\nu} \, dS = \int_{S_w} \mathbf{e}_{m\nu'} \mathbf{e}_{n\nu'} \, dS = \int_{S_w} \mathbf{h}_{m\nu} \mathbf{h}_{n\nu} \, dS = \int_{S_w} \mathbf{h}_{m\nu'} \mathbf{h}_{n\nu'} \, dS = \delta_{nm}, \tag{4.6}$$

where δ_{nm} denotes the Kronecker symbol. In special cases, e.g. rectangular or circular cross-sections, exact solutions to the eigenvalue problems (4.4) are well known [33].

The functions with (z,t)-dependence in (4.1), fulfill

$$\begin{aligned}
&\mu f_{m\nu,t} + g_{m\nu,z} - \lambda_{m\nu}^2 h_{m\nu} = 0 && \varepsilon f_{n\nu',t} + g_{n\nu',z} - \lambda_{n\nu'}^2 h_{n\nu'} = 0 \\
&\varepsilon g_{m\nu,t} + f_{m\nu,z} = 0 && \mu g_{n\nu',t} + f_{n\nu',z} = 0 \\
&\varepsilon h_{m\nu,t} + f_{m\nu,z} = 0 && \mu h_{n\nu',t} + f_{n\nu',z} = 0.
\end{aligned} \tag{4.7}$$

It has to be noted, that when one considers the Fourier transform with respect to time of (4.7), it can be seen, that solutions decay exponentially for wavenumbers smaller than λ_m, λ_n. They correspond to the *cut off* frequencies (see e.g. [33]). Thus, away from inhomogeneities, for a given frequency range, depending on the geometry of S_w, only a limited number of eigenpairs needs to be considered in the ansatz (4.1). This allows for the reduction of Maxwell's equations to (4.7) and (4.4).

4.2 Spacetime hp-Galerkin Method for Problems with Waveguide Ports

By employing a discontinuous Galerkin discretization we can use different approximations in Ω_w and Ω_D, as depicted in 4.2: While for the part $\mathcal{I}_n \times \Omega_D$ we employ the discretization described in chapter 3, for the subdomain Ω_w, we will approximate the solution with functions mimicking the separation ansatz (4.1). To this end, the waveguide-subdomain Ω_w is partitioned in segments $K = \mathcal{J}_m \times S_w$ leading to a triangulation $\mathcal{T}_w$. Thus, proceeding with the temporal part exactly as in section 3.1.2, we obtain a partitioning of each time-slab $(t_n, t_{n+1}] \times \Omega$, consisting of space-time macro elements $Q = \mathcal{I}_n \times K$, where the spatial elements K are hexahedra in $\mathcal{T}_D$ and waveguide segments in $\mathcal{T}_w$. On the interface $\Gamma_w = \partial\Omega_w \cap \partial\Omega_D$, modeling the waveguide port, we do not impose any constraint on the irregularity of the triangulation. By $\mathcal{F}_w$, we denote the set of non-empty faces $f = K \cap K'$, where $K \in \mathcal{T}_w$ and $K' \in \mathcal{T}_D$.

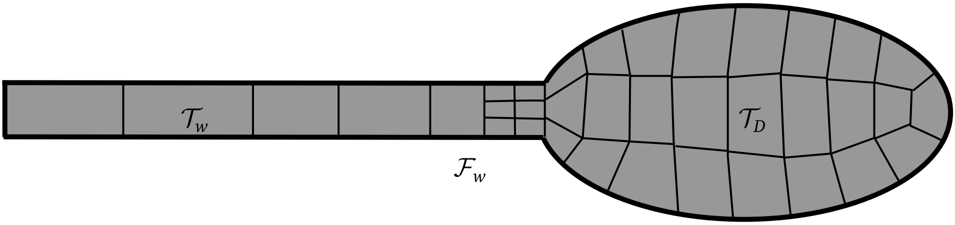

Figure 4.2: Left: Spatial triangulation of Ω consisting of $\mathcal{T}_D(\Omega_D)$ and a waveguide subdomain $\mathcal{T}_w(\Omega_w)$

4.2.1 Finite Element Spaces for Ω_w

For the transverse part we employ the functions satisfying (4.4)

$$V_\nu(S_w) = \text{span}\{v_n(x,y)\}_{n=1}^{N_\nu}, \qquad V_{\nu'}(S_w) = \text{span}\{w_n(x,y)\}_{n=1}^{N_{\nu'}},$$

where N_ν and $N_{\nu'}$ denote the number of TM and TE modes considered. For simplicity, we assume that $\mathcal{S}_w$ is such that an analytical solution is available for the eigenvalue problems (4.4). In general, however, the eigenvalue problems can be solved numerically, for example with an hp-discontinuous Galerkin method.

For the axial and temporal part we employ a tensor product construction analogously to (3.4)

$$V_{zt}(K;p_t,p_z) := S_K(\mathcal{I}_n)\otimes P_{p_z}(\mathcal{J}_m),\ W_{zt}(K;p_t,p_z) := T_K(\mathcal{I}_n)\otimes P_{p_z}(\mathcal{J}_m). \tag{4.8}$$

For the trial- and test-spaces we make use of the following tensor-product spaces

$$\begin{aligned}
V_{n\nu}(Q) &:= V_\nu(S_w)\otimes V_{zt}(\mathcal{I}_n\times\mathcal{I}_m;p_{t,Q},p_{z,Q}),\\
W_{n\nu}(Q) &:= V_\nu(S_w)\otimes W_{zt}(\mathcal{I}_n\times\mathcal{I}_m;p_{t,Q},p_{z,Q}),\\
V_{n\nu'}(Q) &:= V_{\nu'}(S_w)\otimes V_{zt}(\mathcal{I}_n\times\mathcal{I}_m;p_{t,Q},p_{z,Q})\\
W_{n\nu'}(Q) &:= V_{\nu'}(S_w)\otimes W_{zt}(\mathcal{I}_n\times\mathcal{I}_m;p_{t,Q},p_{z,Q})
\end{aligned}$$

The discrete solution is locally approximated in

$$\begin{aligned}
\mathbf{V}^E_\nu(Q) &:= \{\mathbf{v}=\mathbf{v}_T+\mathbf{v}_n : \mathbf{v}_T\in\nabla_T V_{n\nu}(Q),\mathbf{v}_n\in V_{n\nu}(Q)\},\\
\mathbf{V}^H_\nu(Q) &:= \{\mathbf{v}=\mathbf{e}_z\times\mathbf{v}_T : \mathbf{v}_T\in\nabla_T V_{n\nu}(Q)\},
\end{aligned} \tag{4.9}$$

in the TM case and in

$$\begin{aligned}
\mathbf{V}^E_{\nu'}(Q) &:= \{\mathbf{v}=-\mathbf{e}_z\times\mathbf{v}_T : \mathbf{v}_T\in\nabla_T V_{n\nu'}(Q)\},\\
\mathbf{V}^H_{\nu'}(Q) &:= \{\mathbf{v}=\mathbf{v}_T+\mathbf{v}_n : \mathbf{v}_T\in\nabla_T V_{n\nu'}(Q),\mathbf{v}_n\in V_{n\nu'}(Q)\},
\end{aligned} \tag{4.10}$$

in the TE case. The local test-spaces $\mathbf{W}^E_\nu$, $\mathbf{W}^H_{\nu'}$ and $\mathbf{W}^E_{\nu'}$, $\mathbf{W}^H_\nu$ are obtained by replacing $V_{n\nu}(Q)$ in with $W_{n\nu}(Q)$ in (4.9) and $V_{n\nu'}(Q)$ with $W_{n\nu'}(Q)$ in (4.10).

4.2.2 Finite Element Spaces for $\Omega_D\cup\Omega_w$

Recalling for $K\in\mathcal{T}_D$ the spaces $V_{h,\hat{K}},W_{h,\hat{K}}$ from (3.4), we define the trial- and test-spaces for a single time-slab $\mathcal{I}_n\times\Omega$ as

$$\begin{aligned}
V_h^{E,n} :=&\{\mathbf{v}(t,\mathbf{x})\in H^1(\mathcal{I}_n;\mathbf{L}^2(\Omega)) : DF^T\mathbf{v}\big|_K oF\in V_{h,\hat{K}},\ \forall K\in\mathcal{T}_D\\
&\mathbf{v}\big|_K=\mathbf{v}_\nu+\mathbf{v}_{\nu'},\mathbf{v}_\nu\in\mathbf{V}^E_\nu(Q),\mathbf{v}_{\nu'}\in\mathbf{V}^E_{\nu'}(Q)\ \forall Q\in\mathcal{T}_w\}\\
V_h^{H,n} :=&\{\mathbf{v}(t,\mathbf{x})\in H^1(\mathcal{I}_n;\mathbf{L}^2(\Omega)) : DF^T\mathbf{v}\big|_K oF\in V_{h,\hat{K}}\ \forall K\in\mathcal{T}_D,\\
&\mathbf{v}\big|_K=\mathbf{v}_\nu+\mathbf{v}_{\nu'},\mathbf{v}_\nu\in\mathbf{V}^H_\nu(Q),\mathbf{v}_{\nu'}\in\mathbf{V}^H_{\nu'}(Q)\ \forall Q\in\mathcal{T}_w\},\\
&\mathbf{V}_h^n=V_h^{E,n}\times V_h^{H,n}
\end{aligned} \tag{4.11}$$

and

$$\begin{aligned} W_h^{E,n} :=& \{\mathbf{w}(t,\mathbf{x}) \in L^2(\mathcal{I}_n; \mathbf{L}^2(\Omega)) : DF^T \mathbf{w}\Big|_K oF \in W_{h,\hat{K}} \ \forall K \in \mathcal{T}_D, \\ & \mathbf{w}\Big|_K = \mathbf{w}_\nu + \mathbf{w}_{\nu'}, \mathbf{w}_\nu \in \mathbf{W}_\nu^E(Q), \mathbf{w}_{\nu'} \in \mathbf{W}_{\nu'}^E(Q) \ \forall Q \in \mathcal{T}_w\}, \\ W_h^{H,n} :=& \{\mathbf{w}(t,\mathbf{x}) \in L^2(\mathcal{I}_n; \mathbf{L}^2(\Omega)) : DF^T \mathbf{w}\Big|_K oF \in W_{h,\hat{K}} \ \forall K \in \mathcal{T}_D, \\ & \mathbf{w}\Big|_K = \mathbf{w}_\nu + \mathbf{w}_{\nu'}, \mathbf{w}_\nu \in \mathbf{W}_\nu^H(Q), \mathbf{w}_{\nu'} \in \mathbf{W}_{\nu'}^H(Q) \ \forall Q \in \mathcal{T}_w\}. \\ & \mathbf{W}_h^n = W_h^{E,n} \times W_h^{H,n} \end{aligned} \tag{4.12}$$

Furthermore, we denote the global-in-time versions by $\mathbf{V}_h$ and $\mathbf{W}_h$.

4.2.3 Weak Formulation for Waveguide Problems

We apply the weak formulation (3.14) without modifications

$$\begin{aligned} & \text{Find } \mathbf{u}_h \in \mathbf{V}_h^n \\ & B_h(\mathbf{u}_h, \mathbf{w})^n = L_h^n(\mathbf{w}) \ \forall \ \mathbf{w} \ \in \mathbf{W}_h^n. \end{aligned}$$

The only difference lies in the fact, that in the waveguide-domain another set of basis functions is employed, which consists, of $3M\,(p_t+1)\,(p_z+1)$ basis functions for each space-time element in the waveguide-part of the triangulation. Here M denotes the number of propagating modes in the waveguide, which is application dependent and usually rather small. In many cases, the dimensions of the cross-section $\mathcal{S}_w$ are chosen such that only the fundamental mode, corresponding to the smallest eigenvalue in (4.4), can propagate. The evaluation of the local residuals can be carried out with $\mathcal{O}(M\,p^2)$ operations using the same techniques as in section 3.3. Thus, the computational effort for the waveguide part of the discretization corresponds to that of a one-dimensional time-dependent problem, which is often negligible, even if the waveguide domain is several hundred elements long.

It is noteworthy, that the stability analysis presented in chapter 3 is directly applicable, also for discretizations with local refinement in time. Under similar assumptions as in chapter 3 (no local refinement in time, affine elements), the *a priori* error analysis could be extended as well and would yield hp-convergence to the solution in the entire domain Ω.

Thus, provided the length of the waveguide domain Ω_w is chosen, such that no reflections from the end can enter Ω_D, the proposed method yields an arbitrarily accurate “termination” of Ω_D, regardless if evanescent modes are present near the interface Γ_w.

4.3 Modelling of Waveguide Excitation for S-Parameter Computations

S-parameters are frequency-dependent quantities of the form $S_{ij} = \frac{b_i(\omega)}{a_j(\omega)}$. Here, $a_j(\omega)$ and $b_i(\omega)$ denote the incoming and outgoing modal coefficients at the ports Γ_w^j and Γ_w^i respectively. They can be defined for a mode $\mathbf{h}_{n\widetilde{\nu}}$ ($\widetilde{\nu} = \text{TE}$ or $\widetilde{\nu} = \text{TM}$) in (4.1) as

$$a_i(\omega) = \int_0^T \int_{\Gamma_w^i} \mathbf{n} \times (\mathbf{n} \times \mathbf{H}_{inc}) \cdot \mathbf{h}_{n\widetilde{\nu}} e^{i\omega t} \, \mathrm{d}S \, \mathrm{d}t,$$

$$b_i(\omega) = \int_0^T \int_{\Gamma_w^i} \mathbf{n} \times (\mathbf{n} \times (\mathbf{H} - \mathbf{H}_{inc})) \cdot \mathbf{h}_{n\widetilde{\nu}} e^{i\omega t} \, \mathrm{d}S \, \mathrm{d}t. \tag{4.13}$$

In order to excite predefined electromagnetic waves $\mathbf{H}_{inc}$, propagating into Ω_D through the port surface Γ_w^j, we enforce the transmission condition

$$[\![\mathbf{H}]\!]_T = \mathbf{j}_S \ \text{ on } (0,T] \times \Gamma_w^j \quad \mathbf{j}_S = 2g(t)\, \mathbf{e}_{n\widetilde{\nu}}, \tag{4.14}$$

which excites an incident magnetic field with $\mathbf{n} \times (\mathbf{n} \times \mathbf{H}_{inc}) = g(t)\mathbf{h}_{n\widetilde{\nu}}$ on Γ_w^j. The function $g(t)$ is usually chosen, such that it contains a predefined frequency range $[f_1, f_2]$, centered at f_c. A possible choice is

$$g(t) = Re\left[e^{-2\pi t\left(c^2 \pi t - i f_c\right)}\right], \quad c = (f_2 - f_1)/(2\sqrt{2\ln(10)}). \tag{4.15}$$

The condition (4.14) is enforced weakly through the numerical flux, which is

$$\mathbf{E}^* = \{\mathbf{E}_h\} - \alpha_H \left([\![\mathbf{H}_h]\!]_T - \mathbf{j}_S\right), \quad \mathbf{H}^* = \{\mathbf{H}_h\} + \alpha_E [\![\mathbf{E}_h]\!]_T + \frac{1}{2}\mathbf{n} \times \mathbf{j}_S \ \forall f \in \mathcal{F}_w,$$

such that, for the model problem

$$\begin{aligned}
&\varepsilon \partial_t \mathbf{E} - \nabla \times \mathbf{H} = 0 \ \text{ in } \Omega \times (0,T] \\
&\mu \partial_t \mathbf{H} + \nabla \times \mathbf{E} = 0 \ \text{ in } \Omega \times (0,T] \\
&\mathbf{n} \times \mathbf{E} = 0 \ \text{ on } \partial\Omega \times (0,T] \\
&[\![\mathbf{H}]\!]_T = \mathbf{j}_S \ \text{ on } \Gamma_w^j \times (0,T] \\
&\mathbf{E} = 0, \ \ \mathbf{H} = 0 \text{ in } \Omega \times \{0\},
\end{aligned} \tag{4.16}$$

we obtain the discrete problem

$$
\begin{aligned}
&\text{Find } \mathbf{u}_h \in \mathbf{V}_h^n \\
&B_h(\mathbf{u}_h, \mathbf{w})^n = L_h^n(\mathbf{w}) \; \forall\, \mathbf{w} \; \in \mathbf{W}_h^n, \\
&L_h^n(\mathbf{V}) = -\int_{\mathcal{I}_n}\int_{\Omega} \mathbf{j}_S \cdot \{\mathbf{v}\} \,\mathrm{d}x\,\mathrm{d}t + \int_{\mathcal{I}_n}\int_{\Omega} \alpha_H \mathbf{j}_S \cdot [\![\mathbf{w}]\!]_T \,\mathrm{d}x\,\mathrm{d}t,
\end{aligned}
$$

with the spaces $\mathbf{V}_h^n, \mathbf{W}_h^n$ from (4.11) and (4.12).

4.4 Numerical Experiment

4.4.1 Waveguide Transmission

To evaluate the accuracy of the proposed method for realizing waveguide ports, we consider the propagation of a TE_{10}-mode in a rectangular waveguide with $\varepsilon = \mu = 1$. The computational domain is given by $\Omega_D = [0,2] \times [0,1] \times [0,24]$ and extended with two waveguide domains Ω_w^1, Ω_w^2 at both ends. The problem under consideration is (4.16) and excitation at the port with surface Γ_w^1, located at $z = 0$, is chosen as in (4.14), such that $\mathbf{H}_{inc} = g(t - t_o)\mathbf{e}_{1,\mathrm{TE}}$ with $g(t)$ from (4.15). The frequency range is $f_1 = 1.45 f_{cut,1}, f_2 = 0.95 f_{cut,2}$, where $f_{cut,1} = 1/4$ and $f_{cut,2}$ are the cut-off frequencies of the considered TE_{10}-mode and the modes TE11/TM11. The simulation duration corresponds to 150 periods at the center frequency $f_c = (f_1 + f_2)/2$ and the time offset t_o to 20 periods. The length of Ω_w^1 and Ω_w^2 is 100 wavelengths at the center frequency f_c, such that even for a simulation time corresponding to 150 periods at frequency f_c, reflections from the ends cannot enter Ω_D. The spatial mesh covering Ω_D consists of only $2 \times 1 \times 24$ hexahedral elements and each waveguide-domain is meshed with 240 segments. The polynomial degrees are isotropic in space and time ie. $p_t = p_x = p_y = p_z = p$.

In Fig. 4.3 we show the convergence of the magnitudes of the reflection and transmission parameters S_{11} and S_{21} under p-refinement for the energy conserving formulation as well as the formulation with the dissipative flux. The S-parameters converge exponentially for both formulations. The results of the stabilized formulation are more accurate for most of the considered frequency points, than those, obtained with the energy conserving, centered flux formulation. This is expected given the *a priori*-error analysis in chapter 3.

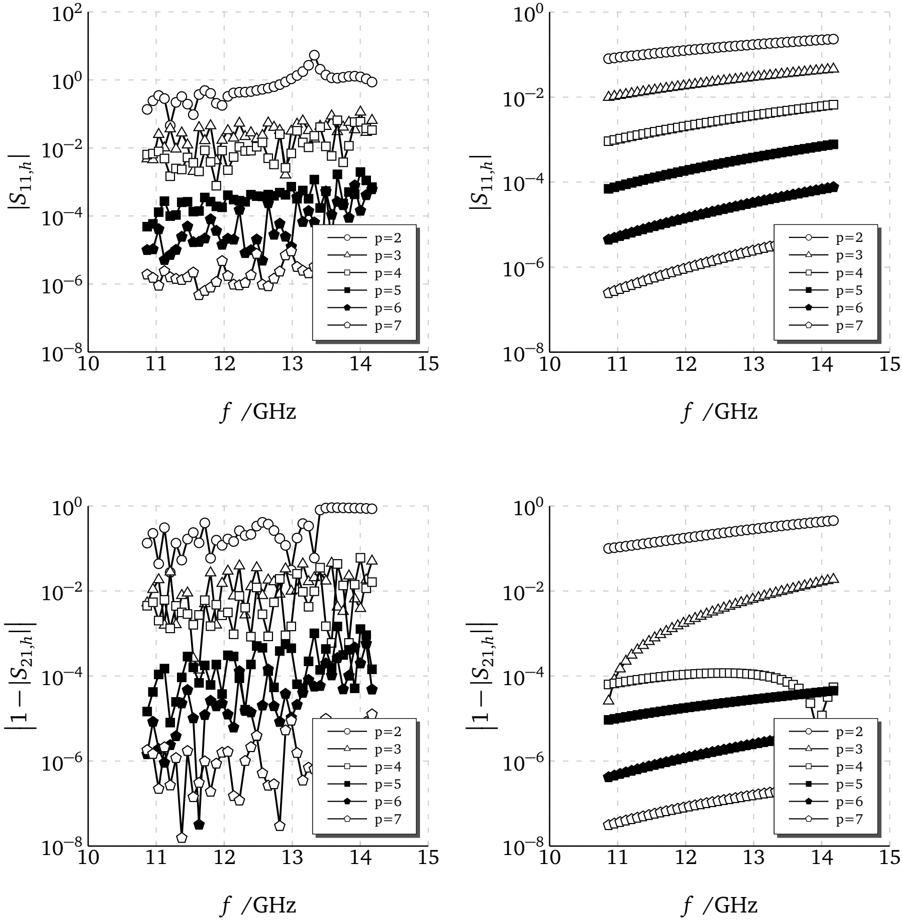

Figure 4.3: Convergence of S-parameters under p-refinement. Top row: Convergence of the magnitude of the reflection parameter $S_{11}(f)$. Bottom row: Convergence of the magnitude of the transmission parameter $S_{21}(f)$. Left: Results obtained, using the formulation with centered fluxes. Right: Results obtained, using the formulation with dissipative stabilization.

4.5 Conclusion

In this chapter, we have developed an extension of the space-time discontinuous Galerkin method, which allows to discretize waveguide structures in an efficient way. To this end, we have constructed basis functions consisting of waveguide modes in the transversal directions and tensor-product polynomials in the time- and axial directions. This reduces the number of degrees of freedom in parts of the computational domain with waveguide structure significantly. As the extension is consistent with the space-time formulation (3.14), the results of the *a priori* error analysis can be extended and exponential convergence for smooth solutions is observed in numerical tests.

5 Approximation of Quantity-of-Interest Functionals

For many practical applications derived quantities of the solution are more important than the actual field solution. Examples for such QOIs include antenna farfields or the RCS of objects, the specific absorption rate SAR of a tissue sample, or scattering parameters.

Mathematically, QOIs can be represented as a functional on the solution space $J : \mathbf{V} \to \mathbb{R}$. Performing mesh adaptation with the aim of computing a QOI with a given error tolerance rather than minimizing some global error norm of the field solution can lead to substantially different mesh refinements. In particular, significantly less computational resources can be required for reducing the error in a QOI to a given tolerance if goal-oriented adaptivity is performed.

The efficient and reliable computation of such QOIs within adaptive algorithms has been an active topic of research for the last 20 years. In particular, *a posteriori* error estimation for QOIs by adjoint techniques such as the dual-weighted-residual (DWR) method (see the review articles [8, 19]) received much attention. Adjoint-based error estimation is based on a general theoretical framework, which is applicable to a wide range of problems, including linear and nonlinear elliptic, parabolic and hyperbolic problems. Applications include elasticity, the Euler- and Navier-Stokes equations [24–26], scalar linear hyperbolic problems [6, 30], Maxwell's equations in the frequency domain [32], elliptic eigenvalue problems and optimal control problems [29]. The DWR method is applicable to discretization methods, which can be cast into a variational framework as it is the case for continuous and discontinuous Galerkin methods as well as some finite volume methods [17] and the FDTD and FIT methods [39].

The abstract *a priori*-error analysis for QOIs has been carried out for conforming finite element methods in [19]. For scalar hyperbolic equations discretized with DG, *hp* error bounds were presented in [30] and for PDEs with non-negative characteristic form in [22]. For smooth solutions such *a priori* estimates yield improved convergence rates of $\mathcal{O}(h^{2p})$ for QOIs, compared to estimates in the energy norm ($\mathcal{O}(h^p)$). However, these improved convergence rates can only be realized when also the associated dual solution is smooth, which in turn depends on the particular QOI functional [21].

First the model-problem under consideration and its adjoint problem for a volume-based QOI-functional are stated. Then, an outline of the adjoint-based *a posteriori* error estimate is given in an abstract setting. Finally, the necessary consistencies are verified and an adjoint-based error estimator for the discretization of Maxwell's equations presented in chapter 3 is derived. Furthermore, applying techniques similar to [22], an *hp*-*a priori* error analysis for linear QOI functionals is presented, confirming improved convergence rates in comparison to the norm-based error estimates from chapter 3. Finally the *a posteriori* and *a priori* error estimates are validated with numerical experiments.

5.1 A Dual Maxwell Problem

The dual problem and its boundary conditions depend on the primal problem, including the boundary conditions as well as the QOI functional. We consider as a model problem

$$\begin{aligned}
&\varepsilon\partial_t\mathbf{E}-\nabla\times\mathbf{H}=\mathbf{J}\ \text{ in }\Omega\times(0,T]\\
&\mu\partial_t\mathbf{H}+\nabla\times\mathbf{E}=0\ \text{ in }\Omega\times(0,T]\\
&\mathbf{n}\times\mathbf{E}=0\ \text{ on }\partial\Omega\times(0,T]\\
&\mathbf{E}=0,\ \ \mathbf{H}=0\text{ in }\Omega\times\{0\},
\end{aligned}\tag{5.1}$$

and the volume based QOI functional

$$J(\mathbf{u})=\int_0^T\int_\Omega \mathbf{J}_E\cdot\mathbf{E}\,\mathrm{d}x\,\mathrm{d}t+\int_0^T\int_\Omega \mathbf{J}_H\cdot\mathbf{H}\,\mathrm{d}x\,\mathrm{d}t,$$

where $\mathbf{J}_E:\Omega\times(0,T]\to\mathbb{R}$ and $\mathbf{J}_H:\Omega\times(0,T]\to\mathbb{R}$. We have

$$J(\mathbf{u})=\int_0^T\int_\Omega \mathbf{z}_E\cdot(\varepsilon\partial_t\mathbf{E}-\nabla\times\mathbf{H})\,\mathrm{d}x\,\mathrm{d}t+\int_0^T\int_\Omega \mathbf{z}_H\cdot(\mu\partial_t\mathbf{H}+\nabla\times\mathbf{E})\,\mathrm{d}x\,\mathrm{d}t,$$

and after an integration by parts with respect to space and time

$$\begin{aligned}
J(\mathbf{u}) = & \int_0^T \int_\Omega (-\varepsilon \partial_t \mathbf{z}_E + \nabla \times \mathbf{z}_H) \cdot \mathbf{E} \, \mathrm{d}x \, \mathrm{d}t \\
+ \left[\int_K \varepsilon \mathbf{z}_E \cdot \mathbf{E} \, \mathrm{d}x \right]_{t=0}^{t=T} + & \int_0^T \int_{\partial\Omega} \mathbf{n} \times \mathbf{E} \cdot \mathbf{z}_H \, \mathrm{d}S \, \mathrm{d}t \\
+ & \int_0^T \int_\Omega (-\mu \partial_t \mathbf{z}_H - \nabla \times \mathbf{z}_E) \cdot \mathbf{H} \, \mathrm{d}x \, \mathrm{d}t \\
+ \left[\int_K \mu \mathbf{z}_H \cdot \mathbf{H} \, \mathrm{d}x \right]_{t=0}^{t=T} - & \int_0^T \int_{\partial\Omega} \mathbf{n} \times \mathbf{H} \cdot \mathbf{z}_E \, \mathrm{d}S \, \mathrm{d}t.
\end{aligned}$$

Thus, taking into account the initial conditions for **E** and **H** as well as the boundary condition $\mathbf{n} \times \mathbf{E} = 0$ we obtain the dual problem

$$\begin{aligned}
& -\varepsilon \partial_t \mathbf{z}_E + \nabla \times \mathbf{z}_H = \mathbf{J}_E \\
& -\mu \partial_t \mathbf{z}_H - \nabla \times \mathbf{z}_E = \mathbf{J}_H \ \text{ in } \Omega \\
& \mathbf{n} \times \mathbf{z}_E = 0 \text{ on } \partial\Omega \\
& \mathbf{z}_E(T) = 0, \mathbf{z}(T) = 0 \ \text{ in } \Omega,
\end{aligned} \tag{5.2}$$

where the dual boundary condition $\mathbf{n} \times \mathbf{z}_E = 0$ and the terminal conditions $\mathbf{z}_E(T) = 0$, $\mathbf{z}(T) = 0$ have been obtained from the remaining (space-time) surface terms.

5.2 Adjoint Error Representation

Sufficiently smooth solutions $\mathbf{u} \in \mathbf{V}$ to system (5.1) fulfill the continuous variational equation

$$B(\mathbf{u}, \mathbf{w}) = L(\mathbf{w}) \ \forall \ \mathbf{w} \in \mathbf{W}, \tag{5.3}$$

where

$$
\begin{aligned}
B(\mathbf{u},\mathbf{w}) &:= \int_{\mathcal{I}_n}\int_{\Omega} \varepsilon\partial_t \mathbf{E}\cdot\mathbf{w}_E \,\mathrm{d}x\,\mathrm{d}t + \int_{\mathcal{I}_n}\int_{\Omega} \mu\partial_t \mathbf{H}\cdot\mathbf{w}_H \,\mathrm{d}x\,\mathrm{d}t \\
&- \int_{\mathcal{I}_n}\int_{\Omega} \nabla_h\times\mathbf{H}\cdot\mathbf{w}_E \,\mathrm{d}x\,\mathrm{d}t + \int_{\mathcal{I}_n}\int_{\Omega} \nabla_h\times\mathbf{E}\cdot\mathbf{w}_H \,\mathrm{d}x\,\mathrm{d}t, \\
L(\mathbf{w}) &:= \int_{\mathcal{I}_n}\int_{\Omega} \mathbf{J}\cdot\mathbf{w}_E \,\mathrm{d}x\,\mathrm{d}t,
\end{aligned}
$$

and $\mathbf{W}$ is a sufficiently smooth test-space. By using the tangential continuity of $\mathbf{u}$ as in the proof of (3.12) we can replace the forms B and L in (5.3) with B_h and L_h, such that also

$$B_h(\mathbf{u},\mathbf{w}) = L_h(\mathbf{w}) \;\forall\; \mathbf{w} \in \mathbf{W} \tag{5.4}$$

holds, where B_h, L_h are obtained by summing B_h^n, L_h^n over all time-slabs.
Further, the sufficiently smooth solution $\mathbf{z} = \{\mathbf{z}_E, \mathbf{z}_H\}$ to the adjoint problem (5.2) fulfills

$$B(\mathbf{v},\mathbf{z}) = J(\mathbf{v}) \;\forall\; \mathbf{v} \in \mathbf{V}.$$

Thus, provided B_h is adjoint-consistent, i.e.

$$B_h(\mathbf{v},\mathbf{z}) = J(\mathbf{v}) \;\forall\; \mathbf{v} \in \mathbf{V}_h \tag{5.5}$$

and further

$$B_h(\mathbf{v},\mathbf{z}) = J_h(\mathbf{v}) \;\forall\; \mathbf{v} \in \mathbf{V}, \tag{5.6}$$

we can obtain the error representation

$$
\begin{aligned}
J(\mathbf{u}) - J_h(\mathbf{u}_h) &= J_h(\mathbf{u}) - J_h(\mathbf{u}_h) && \text{consistency of } J_h \\
&= B_h(\mathbf{u},\mathbf{z}) - B_h(\mathbf{u}_h,\mathbf{z}) && \text{(5.5) and (5.6)} \\
&= B_h(\mathbf{u}-\mathbf{u}_h,\mathbf{z}) && \text{linearity} \\
&= B_h(\mathbf{u}-\mathbf{u}_h,\mathbf{z}-\widetilde{\mathbf{w}}_h) && \text{Galerkin orthogonality} \\
&= L_h(\mathbf{z}-\widetilde{\mathbf{w}}_h) - B_h(\mathbf{u}_h,\mathbf{z}-\widetilde{\mathbf{w}}_h) && \text{(5.3)} \qquad (5.7)
\end{aligned}
$$

where, in the second step, we have used primal Galerkin orthogonality (3.12) yielding $B_h(\mathbf{u}-\mathbf{u}_h,\widetilde{\mathbf{w}}) = 0$ for any $\widetilde{\mathbf{w}}_h \in \mathbf{W}_h$.
In the following section we show that the required consistency results (5.5) and (5.6) hold and state how the resulting error representation can be employed to obtain a computable *a posteriori* error estimate.

5.3 Goal Oriented *a posteriori* Error Estimate

Before we proceed with deriving the error representation, we verify the consistencies (5.5) and (5.6). We will also account for discretizations with local refinement in time, changing meshes and polynomial-degree distributions (see section 3.2.5).
Recalling the primal discrete problem for this case

$$\begin{aligned}&\text{Find } \mathbf{u}_h^n \in \mathbf{V}_h^n\\ &B_h^n(\mathbf{u}_h^n, \mathbf{w}) = L_h^n(\mathbf{w}) \;\forall\; \mathbf{w} \;\in\; \mathbf{W}_h^n\\ &\mathbf{u}_h^n(t_n) = \Pi_0^n \mathbf{u}_h^{n-1}(t_n),\end{aligned} \tag{5.8}$$

and denoting

$$B_h(\mathbf{u}, \mathbf{w}) := \sum_{n=1}^{N} B_h^n(\mathbf{u}^n, \mathbf{w}) + \sum_{n=2}^{N} \big(\mathbf{u}^n(t_n) - \mathbf{u}^{n-1}(t_n), \mathbf{w}(t_n)\big),$$

we have

Lemma 5.3.1. *For* $\mathbf{z} \in \mathbf{W}$*, sufficiently smooth, the solution* $\mathbf{z}$ *to the adjoint problem* (5.2) *fulfills*

$$B_h(\mathbf{v}, \mathbf{z}) = J(\mathbf{v}) + S_h(\mathbf{v}, \mathbf{z}) := J_h(\mathbf{v}) \;\forall\; \mathbf{v} \;\in \mathbf{V}_h \tag{5.9}$$

and further for sufficiently smooth $\mathbf{v}$

$$B_h(\mathbf{v}, \mathbf{z}) = J(\mathbf{v}) \;\forall\; \mathbf{v} \;\in \mathbf{V}. \tag{5.10}$$

Proof. There holds

$$
\begin{aligned}
B_h(\mathbf{v},\mathbf{z}) = \sum_{n=1}^{N} \Bigg[& \int_{\mathcal{I}_n}\int_{\Omega} \varepsilon \partial_t \mathbf{v}_E^n \cdot \mathbf{z}_E \,\mathrm{d}x\,\mathrm{d}t + \int_{\mathcal{I}_n}\int_{\Omega} \mu \partial_t \mathbf{v}_H^n \cdot \mathbf{z}_H \,\mathrm{d}x\,\mathrm{d}t \\
& - \int_{\mathcal{I}_n}\int_{\Omega} \mathbf{v}_H^n \cdot \nabla_h \times \mathbf{z}_E \,\mathrm{d}x\,\mathrm{d}t + \int_{\mathcal{I}_n}\int_{\Omega} \nabla_h \times \mathbf{v}_E^n \cdot \mathbf{z}_H \,\mathrm{d}x\,\mathrm{d}t \\
& + \int_{\mathcal{I}_n}\int_{\mathcal{F}} \{\mathbf{v}_H^n\} \cdot \llbracket \mathbf{z}_E \rrbracket_T \,\mathrm{d}S\,\mathrm{d}t - \int_{\mathcal{I}_n}\int_{\mathcal{F}} \llbracket \mathbf{v}_E^n \rrbracket_T \cdot \{\mathbf{z}_H\} \,\mathrm{d}S\,\mathrm{d}t \\
& + \int_{\mathcal{I}_n}\int_{\mathcal{F}} \alpha_E \llbracket \mathbf{v}_E^n \rrbracket_T \cdot \llbracket \mathbf{z}_E \rrbracket_T \,\mathrm{d}S\,\mathrm{d}t + \int_{\mathcal{I}_n}\int_{\mathcal{F}_0} \alpha_H \llbracket \mathbf{v}_H^n \rrbracket_T \cdot \llbracket \mathbf{z}_H \rrbracket_T \,\mathrm{d}S\,\mathrm{d}t \\
& + \sum_{n=2}^{N} \Bigg[\int_{\Omega} \big(\mathbf{v}_E^n(t_n) - \mathbf{v}_E^{n-1}(t_n)\big) \cdot \varepsilon \mathbf{z}_E \,\mathrm{d}x + \int_{\Omega} \big(\mathbf{v}_H^n(t_n) - \mathbf{v}_H^{n-1}(t_n)\big) \cdot \mu \mathbf{z}_H \,\mathrm{d}x \Bigg] \\
& = \int_0^T \int_{\Omega} \mathbf{J}_E \cdot \mathbf{v}_E \,\mathrm{d}x\,\mathrm{d}t + \int_0^T \int_{\Omega} \mathbf{J}_H \cdot \mathbf{v}_H \,\mathrm{d}x\,\mathrm{d}t + \sum_{n=1}^{N} S_h^n(\mathbf{v}^n,\mathbf{z}). \qquad (5.11)
\end{aligned}
$$

Integrating all time-derivative terms in (5.11) interval-wise by parts with respect to time, integrating element-wise by parts the fourth term in (5.11) with respect to the spatial variables, we can use the tangential continuity of $\mathbf{z}$ and continuity in time of $\mathbf{z}$ to see that the dual solution $\mathbf{z}$ to (5.2) fulfills (5.9) and (5.10).
Note that, that the stabilization term $S_h(\mathbf{v},\mathbf{z})$ vanishes always by tangential continuity of $\mathbf{z}$ and $\mathbf{v}$ for (5.10). For $\mathbf{v} \in \mathbf{V}_h$ and local refinement in time this is however not the case. Thus, we consider in this case the modified functional $J_h(\mathbf{v}) := J(\mathbf{v}) + S_h(\mathbf{v},\mathbf{z})$, as a consistent approximation to $J(\mathbf{v})$, see also the discussion at the end of section 3.1.6. ☐

Having verified the consistencies (5.9) and (5.10), we can proceed with deriving the error representation. Within the error-representation, we will make the particular choice of the function $\widetilde{\mathbf{w}}_h$ as the L^2-projection of $\mathbf{z}$ onto the discrete test-space $\mathbf{W}_h$. To this end, we denote $\Pi^* = \Pi_0\pi_0$, where π_0 and Π_0 are the L^2-projection operators onto the temporal and spatial parts of the discrete test-space $\mathbf{W}_h$, respectively.

Theorem 5.3.1. *Under the assumptions of lemma 5.3.1, the error can be represented by the temporal-, spatial- and iteration-error residuals:*

$$
J(\mathbf{u}) - J_h(\mathbf{u}_h) = \sum_{n=1}^{N} \big[R_h^n(\mathbf{u}_h;\boldsymbol{\eta}_t^*) + R_h^n(\mathbf{u}_h;\boldsymbol{\eta}_s^*) + R_h^n(\mathbf{u}_h;\Pi^*\mathbf{z}) \big] \qquad (5.12)
$$

where

$$
\begin{aligned}
R_h^n(\mathbf{u}_h^n;\mathbf{w}) &:= L_h^n(\mathbf{w}) - B_h^n(\mathbf{u}_h^n,\mathbf{w})\\
&+\int_\Omega \left(\mathbf{E}_h^n(t_n)-\mathbf{E}_h^{n-1}(t_n)\right)\cdot \varepsilon \mathbf{w}_E \,\mathrm{d}x + \int_\Omega \left(\mathbf{H}_h^n(t_n)-\mathbf{H}_h^{n-1}(t_n)\right)\cdot \mu \mathbf{w}_H \,\mathrm{d}x,\\
\boldsymbol{\eta}_t^* &= \mathbf{z}-\pi_0\mathbf{z}, \quad \boldsymbol{\eta}_s^* = \pi_0\mathbf{z}-\Pi_0\pi_0\mathbf{z}.
\end{aligned}
$$

Proof. Using the obtained adjoint consistencies (5.10) and (5.9) with $\mathbf{v}=\mathbf{u}$ and $\mathbf{v}=\mathbf{u}_h$, and further , we obtain

$$
\begin{aligned}
J(\mathbf{u})-J_h(\mathbf{u}_h) &= J_h(\mathbf{u})-J_h(\mathbf{u}_h) = B_h(\mathbf{u},\mathbf{z})-B_h(\mathbf{u}_h,\mathbf{z}) = B_h(\mathbf{u}-\mathbf{u}_h,\mathbf{z})\\
&= B_h(\mathbf{u}-\mathbf{u}_h,\mathbf{z}-\widetilde{\mathbf{w}}_h)+B_h(\mathbf{u}-\mathbf{u}_h,\widetilde{\mathbf{w}}_h) = R_h(\mathbf{u}_h;\mathbf{z}-\widetilde{\mathbf{w}}_h)+R_h(\mathbf{u}_h;\widetilde{\mathbf{w}}_h).
\end{aligned}
$$

Choosing $\widetilde{\mathbf{w}}_h = \Pi^*\mathbf{z}$, we have

$$
J(\mathbf{u})-J_h(\mathbf{u}_h) = R_h(\mathbf{u}_h;\mathbf{z}-\Pi^*\mathbf{z})+R_h(\mathbf{u}_h;\Pi^*\mathbf{z}).
$$

Note that in the case of exact solution of the linear systems, due to Galerkin orthogonality (3.12), there holds $R_h(\mathbf{u}_h;\Pi^*\mathbf{z})=0$, such that we can associate $R_h(\mathbf{u}_h;\Pi^*\mathbf{z})$ with the error due to inexact solution.
Introducing the splitting of the projection error

$$
\mathbf{z}-\Pi^*\mathbf{z} = \mathbf{z}-\pi_0\mathbf{z}+\pi_0\mathbf{z}-\Pi_0\pi_1\mathbf{z} =: \boldsymbol{\eta}_t^*+\boldsymbol{\eta}_s^*, \tag{5.13}
$$

we obtain the result

$$
J(\mathbf{u})-J_h(\mathbf{u}_h) = \sum_{n=1}^{N}\left[R_h^n(\mathbf{u}_h;\boldsymbol{\eta}_t^*)+R_h^n(\mathbf{u}_h;\boldsymbol{\eta}_s^*)+R_h^n(\mathbf{u}_h;\Pi^*\mathbf{z})\right].
$$

□

Assuming $\mathbf{z}$ is known, the error representation from theorem 5.3.1 can be employed as a stopping criterion within an adaptive algorithm. In order to obtain error indicators for the purpose of local refinement, a localized version of (5.12) is needed:

$$
\begin{aligned}
|J_E(\mathbf{E}-\mathbf{E}_h)+J_H(\mathbf{H}-\mathbf{H}_h)| &\le \sum_{n=1}^{N}\left[\mathcal{E}_t^n+\mathcal{E}_{it}^n\right]+\sum_{n=1}^{N}\sum_{\mathcal{I}_n\times K\in\mathcal{S}_n}\mathcal{E}_{s,K}^n,\\
\mathcal{E}_t^n := \left|R_h^n(\mathbf{u}_h;\boldsymbol{\eta}_t^*)\right|,\quad \mathcal{E}_{it}^n &:= \left|R_h^n(\mathbf{u}_h;\Pi^*\mathbf{z})\right|,\quad \mathcal{E}_{s,K}^n := \left|R_{h,K}^n(\mathbf{u}_h;\boldsymbol{\eta}_s^*)\right|
\end{aligned} \tag{5.14}
$$

where $R^n_{h,K}$ denotes the restriction of the residual to the space-time (macro) element $\mathcal{I}_n \times K$. Thanks to the splitting of the dual projection error $\boldsymbol{\eta}^*$, we obtain the temporal and spatial error indicators $\mathcal{E}^n_t$ and spatial $\mathcal{E}^n_{s,K}$, respectively. Furthermore, for anisotropic spatial refinement on hexahedral meshes, we split

$$\begin{aligned}
&\boldsymbol{\eta}^* = \boldsymbol{\eta_t}{}^* + \boldsymbol{\eta}^*_x + \boldsymbol{\eta}^*_y + \boldsymbol{\eta}^*_z,\\
&\boldsymbol{\eta}^*_x = \pi_0\mathbf{z} - \widehat{\Pi}_x\pi_0\mathbf{z}, \qquad \boldsymbol{\eta}^*_y = \widehat{\Pi}_x\pi_0\mathbf{z} - \widehat{\Pi}_y\widehat{\Pi}_x\pi_0\mathbf{z},\ \boldsymbol{\eta}^*_z = \widehat{\Pi}_y\widehat{\Pi}_x\pi_0\mathbf{z} - \widehat{\Pi}_z\widehat{\Pi}_y\widehat{\Pi}_x\pi_0\mathbf{z},
\end{aligned}$$

where to projections $\widehat{\Pi}_x$, $\widehat{\Pi}_y$, $\widehat{\Pi}_z$ are carried out on the spatial reference element $\widehat{K}$. Thus, in the anisotropic case we obtain

$$\begin{aligned}
&|J_E(\mathbf{E}-\mathbf{E}_h) + J_H(\mathbf{H}-\mathbf{H}_h)| \leq \sum_{n=1}^{N}\left[\mathcal{E}^n_t + \mathcal{E}^n_{it}\right] + \sum_{n=1}^{N}\sum_{\mathcal{I}_n\times K\in\mathcal{S}_n}\left[\mathcal{E}^n_{x,K} + \mathcal{E}^n_{y,K} + \mathcal{E}^n_{z,K}\right],\\
&\mathcal{E}^n_{x,K} := \left|R^n_{h,K}(\mathbf{u}_h;\boldsymbol{\eta}^*_x)\right|, \qquad \mathcal{E}^n_{y,K} := \left|R^n_{h,K}(\mathbf{u}_h;\boldsymbol{\eta}^*_y)\right|, \qquad \mathcal{E}^n_{z,K} := \left|R^n_{h,K}(\mathbf{u}_h;\boldsymbol{\eta}^*_z)\right|
\end{aligned} \tag{5.15}$$

Please note, that the error bounds (5.14) and (5.15), should only be used for the purpose of local refinement indicators. Summing up the absolute values of the local contributions in (5.14) can lead to estimates being orders of magnitude larger than (5.12), see for a detailed discussion e.g. [8].

5.3.1 Evaluation of the *a posteriori* Error Estimator

Since the error representation formula from theorem 5.3.1 contains the in general unknown solution $\mathbf{z}$ to the continuous adjoint problem (5.2), we will replace it by an approximation $\widetilde{\mathbf{z}}_h$ in a larger space $\widetilde{\mathbf{V}}_h$. It should be noted, that due to Galerkin-orthogonality, we cannot choose $\widetilde{\mathbf{z}}_h$ in $\mathbf{W}_h$, since this would yield an error equal to zero.

One might raise the question, why then one should not directly approximate $\mathbf{u}$ by $\widetilde{\mathbf{u}}_h$ in a larger space and simply evaluate the approximate error $J(\widetilde{\mathbf{u}}_h) - J(\mathbf{u}_h)$. However, while this approach delivers information about the size of the error in the QOI, it delivers no information for guiding adaptive refinement with the goal of reducing the QOI-error. This information is contained in the residuals weighted by the dual solution.

In the literature, one can find several approaches for obtaining an improved approximation to $\mathbf{z}$. The conceptually simplest, but from the computational point of view probably also most expensive approach, consists of solving the dual problem directly in a larger space as proposed in [31]. A different approach is to solve the dual problem in the same space as the primal problem and using techniques, which rely on superconvergence properties of finite element approximations such as patch-wise higher order interpolation (see e.g. [5, 8]). Which approach is more suitable, depends on the accuracy demands for the error bound and on the problem at hand. If not stated differently, we will, employ an approach similar to the one proposed in [31]. However, instead of solving the problem directly in the larger space $\widetilde{\mathbf{V}}_h$, we solve the dual problem in the same space as the primal one, extend the solution to a globally p-refined space $\widetilde{\mathbf{V}}_h$ and do only a few linear-solver iterations in the larger space. Numerical experiments suggest, that the approximate dual solution obtained with this approach leads to a sufficiently accurate approximation of the dual weight $\mathbf{z}-\Pi^*\mathbf{z}$, yielding accurate estimates of the error.

In many cases the obtained approximate error representation is accurate enough, to obtain an improved approximation to the value of the QOI by adding the approximate error representation to the functional value. In the literature, this conceptually simple technique is sometimes referred to as adjoint postprocessing (see [19]).

5.4 *a priori* Error Analysis: Linear Functionals

In this section we give *a priori*-estimates for linear quantity-of-interest functionals of the solution. To this end we will apply an approach, similar to the one in [22].

For the analysis we require, that no local refinement with respect to time is present in the discretization, the spatial elements are affine and their polynomial degrees are isotropic $p_x = p_y = p_z = p$. Further, we require exact integration and exact solution of the linear systems. Note, that we again set $q := p_t$ for better readability. Denoting $\boldsymbol{\eta}^* = \mathbf{z}-\Pi^*\mathbf{z}$, we have by Galerkin orthogonality (3.12)

$$\begin{aligned} |J_E(\mathbf{E}-\mathbf{E}_h)+J_H(\mathbf{H}-\mathbf{H}_h)| &= |B_h(\mathbf{u}-\mathbf{u}_h,\boldsymbol{\eta}^*)| \\ &\leq |B_h(\boldsymbol{\eta},\boldsymbol{\eta}^*)|+|B_h(\boldsymbol{\xi},\boldsymbol{\eta}^*)|. \end{aligned} \tag{5.16}$$

The first term in (5.16) can be estimated as

Lemma 5.4.1. *Let assumptions 3.1.1, 3.1.2 and 3.1.3 hold. For* $\mathbf{E},\mathbf{H}\in H^l(\mathcal{I}_n;\mathbf{L}^2(\Omega))$, $\mathbf{z}_E,\mathbf{z}_H \in H^{l^*}(\mathcal{I}_n;\mathbf{H}^{k^*}(\Omega))$ $l,k,l^*,k^* \geq 1$ *with* $\nabla\times\mathbf{E},\nabla\times\mathbf{H}\in H^l(\mathcal{I}_n,\mathbf{L}^2(\Omega)$, $\nabla\times\mathbf{z}_\mathbf{E},\nabla\times\mathbf{z}_\mathbf{H} \in H^{l^*}(\mathcal{I}_n,\mathbf{L}^2(\Omega)$, $\sigma_K^* = \min(p_K+1,k_K^*)$, $\tau^* = \min(q,l^*)$ *there holds with* C *and* C_K *independent of* $\Delta t,h_K,q,p_K$ *and* C_K *depending in general on the maximal number* *of faces per element, shape-regularity and for* (3.43) *on the stabilization parameters* α_E, α_H

$$
\begin{aligned}
|B_h^n(\boldsymbol{\eta}, \boldsymbol{\eta}^*)| \leq{}& C \frac{\Delta t^{2\tau-2}}{q^{2l-2}} \left(\|\varepsilon \mathbf{E}\|^2_{H^l(\mathcal{I}_n;\mathbf{L}^2(\Omega))} + \|\varepsilon \mathbf{H}\|^2_{H^l(\mathcal{I}_n;\mathbf{L}^2(\Omega))} \right) \\
&+ C {\frac{\Delta t^{2\tau^*}}{(q-1)^{2l^*}}}^{2} \Big(\|\mathbf{z}_E\|^2_{H^{l^*}(\mathcal{I}_n;\mathbf{L}^2(\Omega))} + \|\nabla \times \mathbf{z}_E\|^2_{H^{l^*}(\mathcal{I}_n;\mathbf{L}^2(\Omega))} \\
&\qquad \|\mathbf{z}_H\|^2_{H^{l^*}(\mathcal{I}_n;\mathbf{L}^2(\Omega))} + \|\nabla \times \mathbf{z}_H\|^2_{H^{l^*}(\mathcal{I}_n;\mathbf{L}^2(\Omega))} \Big) \\
&+ \sum_K C_K \frac{h_K^{2\sigma_K - 1}}{p_K^{2k_K - 1}} \left(\|\mathbf{E}\|_{L^2(\mathcal{I}_n;\mathbf{H}^{k_K}(\Omega))} + \|\mathbf{H}\|_{L^2(\mathcal{I}_n;\mathbf{H}^{k_K}(\Omega))} \right) \\
&+ \sum_K C_K \frac{h_K^{2\sigma_K^* - 1}}{p_K^{2k_K^* - 1}} \left(\|\mathbf{z}_E\|_{L^2(\mathcal{I}_n;\mathbf{H}^{k_K^*}(\Omega))} + \|\mathbf{z}_H\|_{L^2(\mathcal{I}_n;\mathbf{H}^{k_K^*}(\Omega))} \right)
\end{aligned}
\tag{5.17}
$$

Proof. Using the splittings (3.42) and (5.13) of the primal and dual projection errors respectively we obtain

$$
|B_h^n(\boldsymbol{\eta}, \boldsymbol{\eta}^*)| \leq |B_h^n(\boldsymbol{\eta}_t, \boldsymbol{\eta}_t^*)| + |B_h^n(\boldsymbol{\eta}_t, \boldsymbol{\eta}_s^*)| + |B_h^n(\boldsymbol{\eta}_s, \boldsymbol{\eta}_t^*)| + |B_h^n(\boldsymbol{\eta}_s, \boldsymbol{\eta}_s^*)|. \tag{5.18}
$$

We begin by estimating $|B_h^n(\boldsymbol{\eta}_t, \boldsymbol{\eta}_t^*)|$. Note that we will only consider the terms arising due to the electric equation, the terms arising due to the magnetic equation can be treated analogously.
Applying the Cauchy-Schwarz inequality, the interpolation error estimate (3.2.4) to the primal projection error and a 1D version of (3.37) to the dual projection error, we obtain

$$
\begin{aligned}
&\left| \int_{\mathcal{I}_n} \int_\Omega \varepsilon \partial_t (\mathbf{E} - \pi_1 \mathbf{E}) \cdot (\mathbf{z}_E - \pi_0 \mathbf{z}_E) \, \mathrm{d}x \, \mathrm{d}t \right| \\
&\leq C \frac{\Delta t_n^{\tau-1}}{q^{l-1}} \|\varepsilon \mathbf{E}\|_{H^l(\mathcal{I}_n;\mathbf{L}^2(\Omega))} \frac{\Delta t_n^{\tau^*}}{(q-1)^{l^*}} \|\mathbf{z}_E\|_{H^{l^*}(\mathcal{I}_n;\mathbf{L}^2(\Omega))}.
\end{aligned}
$$

Analogously, we obtain for the curl term:

$$
\begin{aligned}
&\left| \int_{\mathcal{I}_n} \int_\Omega (\mathbf{H} - \pi_1 \mathbf{H}) \cdot \nabla_h \times (\mathbf{z}_E - \pi_0 \mathbf{z}_E) \, \mathrm{d}x \, \mathrm{d}t \right| \\
&\leq C \frac{\Delta t_n^{\tau}}{q^{l}} \|\mathbf{H}\|_{H^l(\mathcal{I}_n;\mathbf{L}^2(\Omega))} \frac{\Delta t_n^{\tau^*}}{(q-1)^{l^*}} \|\nabla_h \times \mathbf{z}_E\|_{H^{l^*}(\mathcal{I}_n;\mathbf{L}^2(\Omega))}.
\end{aligned}
$$

Finally we turn to the mesh dependent terms. For $\mathbf{z}$ the tangential jump vanishes. This yields

$$\begin{aligned}\int_{\mathcal{I}_n}\int_{\mathcal{F}} \{\mathbf{H}-\pi_1\mathbf{H}\}\cdot\llbracket \mathbf{z}_E-\pi_0\mathbf{z}_E\rrbracket_T \,\mathrm{d}S\,\mathrm{d}t &= 0,\\ \int_{\mathcal{I}_n}\int_{\mathcal{F}} \alpha_E\llbracket \mathbf{E}-\pi_1\mathbf{E}\rrbracket_T\cdot\llbracket \mathbf{z}_E-\pi_0\mathbf{z}_E\rrbracket_T \,\mathrm{d}S\,\mathrm{d}t &= 0. \qquad (5.19)\end{aligned}$$

We continue with $|B_h^n(\boldsymbol{\eta}_t,\boldsymbol{\eta}_s^*)|$:
Since, with respect to time, $(\pi_0\mathbf{z}_E-\Pi_0\pi_0\mathbf{z}_E)$ is a polynomial of degree $q-1$, there holds with (3.2.4)

$$\int_{\mathcal{I}_n}\int_{\Omega} \varepsilon\partial_t(\mathbf{E}-\pi_1\mathbf{E})\cdot(\pi_0\mathbf{z}_E-\Pi_0\pi_0\mathbf{z}_E)\,\mathrm{d}x\,\mathrm{d}t = 0$$

Further, we have by element-wise integration by parts

$$\begin{aligned}&\int_{\mathcal{I}_n}\int_{\Omega}(\mathbf{H}-\pi_1\mathbf{H})\cdot\nabla_h\times(\pi_0\mathbf{z}_E-\Pi_0\pi_0\mathbf{z}_E)\,\mathrm{d}x\,\mathrm{d}t\\ &\qquad+\int_{\mathcal{I}_n}\int_{\mathcal{F}}\{\mathbf{H}-\pi_1\mathbf{H}\}\cdot\llbracket \mathbf{z}_E-\Pi_0\pi_0\mathbf{z}_E\rrbracket_T\,\mathrm{d}S\,\mathrm{d}t\\ =&\int_{\mathcal{I}_n}\int_{\Omega}\nabla_h\times(\mathbf{H}-\pi_1\mathbf{H})\cdot(\pi_0\mathbf{z}_E-\Pi_0\pi_0\mathbf{z}_E)\,\mathrm{d}x\,\mathrm{d}t\\ &\qquad+\int_{\mathcal{I}_n}\int_{\mathcal{F}_0}\llbracket \mathbf{H}-\pi_1\mathbf{H}\rrbracket_T\cdot\{\mathbf{z}_E-\Pi_0\pi_0\mathbf{z}_E\}\,\mathrm{d}S\,\mathrm{d}t.\end{aligned}$$

First we note that by tangential continuity of $\mathbf{H}$ and $\pi_0\mathbf{H}$ the second term on the right-hand side vanishes such that after an application of the Cauchy-Schwarz inequality, it remains to estimate the first term using (3.2.4) for the primal interpolation error, and (3.2.3) for the dual interpolation error

$$\begin{aligned}&\left|\int_{\mathcal{I}_n}\int_{\Omega}\nabla_h\times(\mathbf{H}-\pi_1\mathbf{H})\cdot(\pi_0\mathbf{z}_E-\Pi_0\pi_0\mathbf{z}_E)\,\mathrm{d}x\,\mathrm{d}t\right|\\ \leq&\sum_K C_K\frac{\Delta t^\tau}{q^l}\|\nabla\times\mathbf{H}\|_{H^l(\mathcal{I}_n;\mathbf{L}^2(\Omega))}\frac{h^{\sigma_K^*}}{p_K^{k_K^*}}\|\mathbf{z}_E\|_{L^2(\mathcal{I}_n;\mathbf{H}^{k_K^*}(K))}\end{aligned}$$

Once more by tangential continuity of $\mathbf{E}$ and $\pi_1\mathbf{E}$, we have

$$\int_{\mathcal{I}_n}\int_{\mathcal{F}} \alpha_E [\![\mathbf{E}-\pi_1\mathbf{E}]\!]_T \cdot [\![\mathbf{z}_E - \Pi_0\pi_0\mathbf{z}_E]\!]_T \,\mathrm{d}S\,\mathrm{d}t = 0.$$

For the term $|B_h^n(\boldsymbol{\eta}_s, \boldsymbol{\eta}_t^*)|$ we have after applying the Cauchy-Schwarz inequality, (3.37) to the primal approximation error and the 1D-version of (3.37) to the dual one

$$\begin{aligned}&\left|\int_{\mathcal{I}_n}\int_{\Omega} \varepsilon\partial_t(\pi_1\mathbf{E}-\Pi_0\pi_1\mathbf{E})\cdot(\mathbf{z}_E-\pi_0\mathbf{z}_E)\,\mathrm{d}x\,\mathrm{d}t\right|\\ &\le \sum_K C_K \frac{\Delta t^{l^*}}{(q-1)^{l^*}}\|\mathbf{z}_E\|_{H^{l^*}(\mathcal{I}_n;\mathbf{L}^2(\Omega))}\frac{h^{\sigma_K}}{p^{k_K}}\|\mathbf{E}\|_{L^2(\mathcal{I}_n;\mathbf{H}^{k_K}(K))}\end{aligned}$$

similarly, we obtain

$$\begin{aligned}&\left|\int_{\mathcal{I}_n}\int_{\Omega} (\pi_1\mathbf{H}-\Pi_0\pi_1\mathbf{H})\cdot\nabla_h\times(\mathbf{z}_E-\pi_0\mathbf{z}_E)\,\mathrm{d}x\,\mathrm{d}t\right|\\ &\le \sum_K C_K \frac{\Delta t^{l^*}}{(q-1)^{l^*}}\|\nabla\times\mathbf{z}_E\|_{H^{l^*}(\mathcal{I}_n;\mathbf{L}^2(\Omega))}\frac{h^{\sigma_K}}{p^{k_K}}\|\mathbf{H}\|_{L^2(\mathcal{I}_n;\mathbf{H}^{k_K}(K))}.\end{aligned}$$

The mesh dependent terms vanish for the same reason as in (5.22).
Regarding the term $|B_h^n(\boldsymbol{\eta}_s, \boldsymbol{\eta}_s^*)|$ we have, $\boldsymbol{\eta}_s^*$ being a polynomial of degree $q-1$ with respect to time, by (3.2.4)

$$\int_{\mathcal{I}_n}\int_{\Omega} \varepsilon\partial_t(\pi_1\mathbf{E}-\Pi_0\pi_1\mathbf{E})\cdot(\pi_0\mathbf{z}_E-\Pi_0\pi_0\mathbf{z}_E)\,\mathrm{d}x\,\mathrm{d}t = 0.$$

For the curl term we have

$$\begin{aligned}&\int_{\mathcal{I}_n}\int_{\Omega}(\pi_1\mathbf{H}-\Pi_0\pi_1\mathbf{H})\cdot\nabla_h\times(\pi_0\mathbf{z}_E-\Pi_0\pi_0\mathbf{z}_E)\,\mathrm{d}x\,\mathrm{d}t\\ &=\int_{\mathcal{I}_n}\int_{\Omega}(\pi_1\mathbf{H}-\Pi_0\pi_1\mathbf{H})\cdot\nabla_h\times(\pi_0\mathbf{z}_E-\Pi_1\pi_0\mathbf{z}_E)\,\mathrm{d}x\,\mathrm{d}t\\ &+\int_{\mathcal{I}_n}\int_{\Omega}(\pi_1\mathbf{H}-\Pi_0\pi_1\mathbf{H})\cdot\nabla_h\times(\Pi_1\pi_0\mathbf{z}_E-\Pi_0\pi_0\mathbf{z}_E)\,\mathrm{d}x\,\mathrm{d}t,\end{aligned}$$

where the second term on the right hand side vanishes by orthogonality of the L^2-projection. Applying (3.37) for the primal interpolation error and Lemma 3.2.3 for the dual interpolation error

$$\left|\int_{\mathcal{I}_n}\int_{\Omega}(\pi_1\mathbf{H}-\Pi_0\pi_1\mathbf{H})\cdot\nabla_h\times(\pi_0\mathbf{z}_E-\Pi_1\pi_0\mathbf{z}_E)\,\mathrm{d}x\,\mathrm{d}t\right|$$
$$\leq\sum_K C_K\frac{h^{\sigma_K+\sigma_K^*-1}}{p^{k_K+k_K^*-1}}\|\mathbf{z}_E\|_{L^2(\mathcal{I}_n;\mathbf{H}^{k_K^*}(K))}\|\mathbf{H}\|_{L^2(\mathcal{I}_n;\mathbf{H}^{k_K}(K))}.$$

The mesh dependent terms can be estimated as

$$\int_{\mathcal{I}_n}\int_{\mathcal{F}}\{\pi_1\mathbf{H}-\Pi_0\pi_1\mathbf{H}\}\cdot[\![\pi_0\mathbf{z}_E-\Pi_0\pi_0\mathbf{z}_E]\!]_T\,\mathrm{d}S\,\mathrm{d}t$$
$$+\int_{\mathcal{I}_n}\int_{\mathcal{F}}\alpha_E[\![\pi_1\mathbf{E}-\Pi_0\mathbf{E}]\!]_T\cdot[\![\pi_0\mathbf{z}_E-\Pi_0\pi_0\mathbf{z}_E]\!]_T\,\mathrm{d}S\,\mathrm{d}t$$
$$\leq\left(\sum_K C_K\frac{h_K^{2\sigma_K-1}}{p_K^{2k_K-1}}\|\mathbf{H}\|^2_{L^2(\mathcal{I}_n;\mathbf{H}^{k_K}(K))}\right)^{\frac{1}{2}}\times\left(\sum_K C_K\frac{h_K^{2\sigma_K^*-1}}{p_K^{2k_K^*-1}}\|\mathbf{z}_E\|^2_{L^2(\mathcal{I}_n;\mathbf{H}^{k^*}(K))}\right)^{\frac{1}{2}},$$

where we have used the Cauchy-Schwarz inequality and then applied for each face the approximation result (3.38) for the primal and dual approximation errors respectively. Note that the constants also depend on the number of neighbors.

□

For estimating the term $|B_h^n(\xi,\boldsymbol{\eta}^*)|$, we can proceed essentially along the lines of the proof of theorem 3.2.5.

Lemma 5.4.2. *Let assumptions 3.1.1, 3.1.2 and 3.1.3 hold. For* $\mathbf{z}_E,\mathbf{z}_H\in H^{l^*}(\mathcal{I}_n;\mathbf{H}^{k^*}(\Omega)), l^*,k^*\geq 1$ *with* $\nabla\times\mathbf{z_E},\nabla\times\mathbf{z_H}\in H^{l^*}(\mathcal{I}_n,\mathbf{L}^2(\Omega)$, $\sigma_K^*=\min(p_K+1,k_K^*)$, $\tau^*=\min(q,l^*)$ *there holds with* C *and* C_K *independent of* $\Delta t,h_K,q,p_K$ *and* C_K *depending in general on the maximal number of faces per element, shape-regularity and for* (3.43) *on the stabilization parameters* α_E,α_H
for the centered flux formulation ($\alpha_E=\alpha_H=0$)

$$|B_h^n(\xi,\boldsymbol{\eta}^*)|\leq c_H\|\xi_E\|^2_{L^2(\mathcal{I}_n,\mathbf{L}^2(\Omega))}+c_E\|\xi_H\|^2_{L^2(\mathcal{I}_n,\mathbf{L}^2(\Omega))}$$
$$+C\frac{\Delta t_n^{2\tau^*}}{(q-1)^{2l^*}}\left(c_E^{-1}\|\nabla\times\mathbf{z}_E\|^2_{H^{l*}(\mathcal{I}_n;\mathbf{L}^2(\Omega))}+c_H^{-1}\|\nabla\times\mathbf{z}_H\|^2_{H^{l*}(\mathcal{I}_n;\mathbf{L}^2(\Omega))}\right)$$
$$\sum_K C_K\frac{h_K^{2\sigma_K^*-2}}{p_K^{2k_K^*-3}}\left(c_E^{-1}\|\mathbf{z}_E\|^2_{L^2(\mathcal{I}_n;\mathbf{H}^{k_K^*}(K))}+c_H^{-1}\|\mathbf{z}_H\|^2_{L^2(\mathcal{I}_n;\mathbf{H}^{k_K^*}(K))}\right),\tag{5.20}$$

and for the dissipative formulation ($\alpha_E > 0, \alpha_H > 0$)

$$\begin{aligned} |B_h^n(\xi, \boldsymbol{\eta}^*)| \leq c_H \|\xi_E\|^2_{L^2(\mathcal{I}_n, \mathbf{L}^2(\Omega))} + c_E \|\xi_h\|^2_{L^2(\mathcal{I}_n, \mathbf{L}^2(\Omega))} \\ + c_{f,H} \| [\![\xi_E]\!]_T \|^2_{L^2(\mathcal{I}_n, \mathbf{L}^2(\mathcal{F}))} + c_{f,E} \| [\![\xi_H]\!]_T \|^2_{L^2(\mathcal{I}_n, \mathbf{L}^2(\mathcal{F}_0))} \\ + C \frac{\Delta t_n^{2\tau^*}}{(q-1)^{2l^*}} \left(c_E^{-1} \|\nabla \times \mathbf{z}_E\|^2_{H^{l^*}(\mathcal{I}_n; \mathbf{L}^2(\Omega))} + c_H^{-1} \|\nabla \times \mathbf{z}_H\|^2_{H^{l^*}(\mathcal{I}_n; \mathbf{L}^2(\Omega))} \right) \\ \sum_K C_K \frac{h_K^{2\sigma_K^* - 1}}{p_K^{2k_K^* - 1}} \left(c_{f,E}^{-1} \|\mathbf{z}_E\|^2_{L^2(\mathcal{I}_n; \mathbf{H}^{k_K^*}(K))} + c_{f,H}^{-1} \|\mathbf{z}_H\|^2_{L^2(\mathcal{I}_n; \mathbf{H}^{k_K^*}(K))} \right). \end{aligned} \tag{5.21}$$

Proof. Writing

$$|B_h^n(\xi, \boldsymbol{\eta}^*)| \leq |B_h^n(\xi, \boldsymbol{\eta}_t^*)| + |B_h^n(\xi, \boldsymbol{\eta}_s^*)|,$$

we proceed with $|B_h^n(\xi, \boldsymbol{\eta}_t^*)|$. Since $\partial_t \xi$ is a polynomial of degree $q-1$, we have by orthogonality

$$\int_{\mathcal{I}_n} \int_\Omega \varepsilon \partial_t \xi_E \cdot (\mathbf{z}_E - \pi_0 \mathbf{z}_E) \, \mathrm{d}x \, \mathrm{d}t = 0.$$

For the curl terms we have

$$\begin{aligned} &\left| \int_{\mathcal{I}_n} \int_\Omega \xi_H \cdot \nabla_h \times (\mathbf{z}_E - \pi_0 \mathbf{z}_E) \, \mathrm{d}x \, \mathrm{d}t \right| \\ &\leq C \|\xi\|_{L^2(\mathcal{I}_n; \mathbf{L}^2(\Omega))} \frac{\Delta t^{\tau^*}}{(q-1)^{l^*}} \|\nabla_h \times \mathbf{z}_E\|_{H^{l^*}(\mathcal{I}_n; \mathbf{L}^2(\Omega))}. \end{aligned}$$

Similarly to (5.22), for the mesh dependent terms holds

$$\begin{aligned} \int_{\mathcal{I}_n} \int_{\mathcal{F}} \{\xi_H\} \cdot [\![\mathbf{z}_E - \pi_0 \mathbf{z}_E]\!]_T \, \mathrm{d}S \, \mathrm{d}t = 0, \\ \int_{\mathcal{I}_n} \int_{\mathcal{F}} \alpha_E [\![\xi_E]\!]_T \cdot [\![\mathbf{z}_E - \pi_0 \mathbf{z}_E]\!]_T \, \mathrm{d}S \, \mathrm{d}t = 0. \end{aligned} \tag{5.22}$$

For the term $|(\xi, \boldsymbol{\eta}_s^*)|$, we have by L^2-orthogonality

$$\int_{\mathcal{I}_n} \int_\Omega \varepsilon \partial_t \xi_E \cdot (\pi_0 \mathbf{z}_E - \Pi_0 \pi_0 \mathbf{z}_E) \, \mathrm{d}x \, \mathrm{d}t = 0$$

By integration by parts we obtain we obtain

$$\begin{aligned}
&\int_{\mathcal{I}_n}\int_{\Omega} \xi_H \cdot \nabla_h \times (\pi_0 \mathbf{z}_E - \Pi_0 \pi_0 \mathbf{z}_E)\,\mathrm{d}x\,\mathrm{d}t \\
&\quad + \int_{\mathcal{I}_n}\int_{\mathcal{F}} \{\xi_H\} \cdot [\![\pi_0 \mathbf{z}_E - \Pi_1 \pi_0 \mathbf{z}_E]\!]_T\,\mathrm{d}S\,\mathrm{d}t \\
&= \int_{\mathcal{I}_n}\int_{\Omega} \nabla_h \times \xi_H \cdot (\pi_0 \mathbf{z}_E - \Pi_0 \pi_0 \mathbf{z}_E)\,\mathrm{d}x\,\mathrm{d}t \\
&\quad + \int_{\mathcal{I}_n}\int_{\mathcal{F}} \{\pi_0 \mathbf{z}_E - \Pi_1 \pi_0 \mathbf{z}_E\} \cdot [\![\xi_H]\!]_T\,\mathrm{d}S\,\mathrm{d}t,
\end{aligned}$$

where the first term vanishes by orthogonality. Thus it remains to estimate the mesh dependent terms. For the *dissipative* formulation we have (see the proof of Theorem 3.2.5, (3.47) and (3.49))

$$\begin{aligned}
&\int_{\mathcal{I}_n}\int_{\mathcal{F}} \{\pi_0 \mathbf{z}_E - \Pi_1 \pi_0 \mathbf{z}_E\} \cdot [\![\xi_H]\!]_T\,\mathrm{d}S\,\mathrm{d}t + \int_{\mathcal{I}_n}\int_{\mathcal{F}} \alpha_E [\![\xi_E]\!]_T \cdot [\![\pi_0 \mathbf{z}_E - \Pi_0 \pi_0 \mathbf{z}_E]\!]_T\,\mathrm{d}S\,\mathrm{d}t \\
&\leq \left(\sum_K C \frac{h_K^{2\sigma_K^*-1}}{p_K^{2k_K^*-1}} \|\mathbf{z}_{\mathbf{E}}\|^2_{L^2(\mathcal{I}_n;\mathbf{H}^{k_K^*}(K))} \right)^{1/2} \left(\|[\![\xi_H]\!]_T\|_{L^2(\mathcal{I}_n;\mathbf{L}^2(\mathcal{F}))} + \|[\![\xi_E]\!]_T\|_{L^2(\mathcal{I}_n;\mathbf{L}^2(\mathcal{F}))} \right)
\end{aligned}$$

For the *centered* formulation, recalling (3.50), there holds

$$\begin{aligned}
&\left| \int_{\mathcal{I}_n}\int_{\mathcal{F}} \{\pi_0 \mathbf{z}_E - \Pi_1 \pi_0 \mathbf{z}_E\} \cdot [\![\xi_H]\!]_T\,\mathrm{d}S\,\mathrm{d}t \right| \\
&\leq c_H^{-1} \sum_K C_K \frac{h^{2\sigma_K^*-2}}{p_K^{2k_K^*-3}} \|\mathbf{z}_E\|^2_{L^2(\mathcal{I}_n;\mathbf{H}^{k_K^*}(K)]^3)} + c_H \|\xi_H\|^2_{L^2(\mathcal{I}_n;\mathbf{L}^2(K))}
\end{aligned}$$

☐

Recalling (5.16), we can now sum up the contributions for each time-slab from the bounds for $|B_h^n(\boldsymbol{\eta}, \boldsymbol{\eta}^*)|$ and $|B_h^n(\xi, \boldsymbol{\eta}^*)|$ from lemmas 5.4.1 and 5.4.2, respectively. Then, the estimate from lemma 3.2.6 is employed to bound the consistency error ξ in (5.20). This is yields theorem 5.4.1.

In the case of global polynomial degrees in space and in time and quasiuniform meshes, for sufficiently smooth primal and dual solutions, the *a priori* estimate yields convergence orders of h^{2p}/p^{2k-3} with respect to space and of $\Delta t^{2q}/q^{*2l^*}$

with respect to time. For QOIs we thus obtain twice the convergence rate of the energy-norm estimate, when considering the spatial part of the discretization. For the temporal part, we only obtain a convergence rate of $2q$ due to the approximation properties of the discrete test-space, consisting of polynomials with degree $q^* = q - 1$.

Theorem 5.4.1. *Under the assumptions of lemmas 3.2.6, 5.4.1 and 5.4.2, there holds for the centered formulation*

$$
\begin{aligned}
|J(\mathbf{u} - J(\mathbf{u}_h))| \leq T^2 \sum_{n=1}^{N} C \frac{\Delta t_n^{2\tau}}{q_n^{2l}} \left(\underline{\varepsilon}^{-1} \|\nabla \times \mathbf{H}\|^2_{H^l(\mathcal{I}_n;\mathbf{L}^2(\Omega))} + \underline{\mu}^{-1} \|\nabla \times \mathbf{E}\|^2_{H^l(\mathcal{I}_n;\mathbf{L}^2(\Omega))} \right) \\
+ T^2 \sum_{n=1}^{N} \sum_{K} C_K \frac{h_K^{2\sigma-2}}{p_K^{2k-3}} \left(\underline{\mu}^{-1} \|\mathbf{E}\|^2_{L^2(\mathcal{I}_n;\mathbf{H}^k(K))} + \underline{\varepsilon}^{-1} \|\mathbf{H}\|^2_{L^2(\mathcal{I}_n;\mathbf{H}^k(K))} \right) \\
+ \sum_{n=1}^{N} C \frac{\Delta t_n^{2\tau^*}}{(q-1)^{2l^*}} \left(c_E^{-1} \|\nabla \times \mathbf{z}_E\|^2_{H^{l^*}(\mathcal{I}_n;\mathbf{L}^2(\Omega))} + c_H^{-1} \|\nabla \times \mathbf{z}_H\|^2_{H^{l^*}(\mathcal{I}_n;\mathbf{L}^2(\Omega))} \right) \\
\sum_{n=1}^{N} \sum_{K} C_K \frac{h_K^{2\sigma_K^*-2}}{p_K^{2k_K^*-3}} \left(c_E^{-1} \|\mathbf{z}_E\|^2_{L^2(\mathcal{I}_n;\mathbf{H}^{k_K^*}(K))} + c_H^{-1} \|\mathbf{z}_H\|^2_{L^2(\mathcal{I}_n;\mathbf{H}^{k_K^*}(K))} \right).
\end{aligned}
\tag{5.23}
$$

The case of the dissipative formulation is subject of ongoing work. Here an improved convergence rate of h^{2p+1}/p^{2k-1} compared to the centered formulation is expected.

5.5 Numerical Experiments

5.5.1 Rectangular Waveguide

In order to validate the obtained error estimate for QOIs from theorem 5.23, we consider the propagation of a time-harmonic TE_{mn}-mode of angular frequency ω in a rectangular waveguide. The waveguide has a cross section $\mathcal{S}_w = [0, a] \times [0, b]$, with normal $\mathbf{n} = \mathbf{e}_z$, and the mode is propagating in $\mathbf{e}_z$ direction. The exact solution is given by

$$
\begin{aligned}
&\mathbf{E}_{\mathrm{TE}} = \mathbf{e}_{2,\mathrm{TE}} \cos(\omega t - k_z z), \quad \mathbf{e}_{2,\mathrm{TE}} = -k_y \cos(k_x x) \sin(k_y y) \mathbf{e}_x + k_x \sin(k_x x) \cos(k_y y) \mathbf{e}_y \\
&\mathbf{H}_{\mathrm{TE}} = \mathbf{h}_{2,\mathrm{TE}} \cos(\omega t - k_z z) + v_{2,\mathrm{TE}} \sin(\omega t - k_z z) \mathbf{e}_z \quad v_{2,\mathrm{TE}} = \frac{k_x^2 + k_y^2}{\omega \mu} \cos(k_x x) \cos(k_y y) \\
&k_x = m\pi/a, \;\; k_y = n\pi/b, \;\; k_z = (\varepsilon \mu \omega^2 - (k_x^2 + k_y^2))^{1/2}.
\end{aligned}
\tag{5.24}
$$

We choose $m = n = a = b = \varepsilon = \mu = 1$, $k_z = \pi/2$ and the length of the waveguide as $L = 10$. The problem under consideration is (5.1) with the boundary condition

$$\mathbf{n} \times \mathbf{E} = \mathbf{n} \times \mathbf{E}_{\mathrm{TE}}. \tag{5.25}$$

We consider the QOI-functional

$$J_H(\mathbf{H}) = \int_0^{2\pi/\omega} \int_{\mathcal{S}^+} \mathbf{h}_{2,\mathrm{TE}} \cdot \mathbf{H} \cos(\omega t - \pi/2) dx dt, \tag{5.26}$$

which could be used for S-parameter evaluation. $\mathcal{S}^+$ denotes the cross-sectional (outflow) surface at the end ($z = 10$) of the waveguide. Proceeding as in (5.1), we obtain for the QOI in (5.26) the dual problem

$$\begin{aligned}
&-\varepsilon \partial_t \mathbf{z}_E + \nabla \times \mathbf{z}_H = 0 \\
&-\mu \partial_t \mathbf{z}_H - \nabla \times \mathbf{z}_E = 0 \ \text{ in } \Omega \\
&\mathbf{n} \times \mathbf{z}_E = \mathbf{n} \times \mathbf{e}_{2,\mathrm{TE}} \cos(\omega t - \pi/2) \text{ on } \mathcal{S}_w^+ \\
&\mathbf{n} \times \mathbf{z}_E = 0 \text{ on } \partial\Omega \backslash \mathcal{S}_w^+ \\
&\mathbf{z}_E(t = T) = 0, \mathbf{z}(t = T) = 0 \ \text{ in } \Omega,
\end{aligned} \tag{5.27}$$

where we have used $\mathbf{h}_{2,\mathrm{TE}} = \mathbf{e}_z \times \mathbf{h}_{2,\mathrm{TE}}$. One can observe that the QOI functional translates to an inhomogeneous boundary condition for $\mathbf{n} \times \mathbf{z}_E$ yielding a smooth dual solution, which is depicted in figure 5.1.

Centered flux - J_H			
	$p = 1$	$p = 2$	$p = 3$
e_{J_H}	1.77	5.89	5.69
$\mathcal{E}_s$	1.85	6.14	5.71
$\mathcal{E}_t$	1.90	3.98	5.97

Dissipative flux - J_H			
	$p = 1$	$p = 2$	$p = 3$
e_{J_H}	2.72	4.88	6.90
$\mathcal{E}_s$	2.90	4.84	6.94
$\mathcal{E}_t$	1.89	3.98	5.96

Table 5.1: Left: Experimentally obtained convergence rates of the errors $e_{J_H} := |J_H(\mathbf{H}) - J_H(\mathbf{H}_h)|$, the spatial and temporal parts $\mathcal{E}_s$ and $\mathcal{E}_t$ of the error estimate (5.12) for the non-dissipative formulation. Right: The corresponding data, obtained with the dissipative formulation.

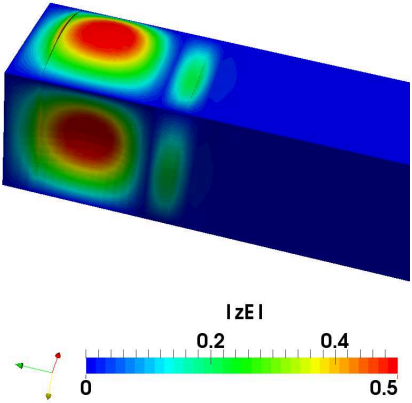

Figure 5.1: Left: Magnitude of the approximate dual solution $\mathbf{z}_E$ for the QOI $J_H(\mathbf{H})$

Centered flux - J_H			
h	$p=1$	$p=2$	$p=3$
$5 \cdot 10^{-2}$	1.17	0.98	1.05
$2.5 \cdot 10^{-2}$	1.02	0.98	1.01
$1.25 \cdot 10^{-2}$	1.00	0.97	1.00
$6.25 \cdot 10^{-3}$	1.00	0.99	1.00

Dissipative flux - J_H			
h	$p=1$	$p=2$	$p=3$
$5 \cdot 10^{-2}$	1.07	0.91	1.06
$2.5 \cdot 10^{-2}$	1.02	0.97	1.01
$1.25 \cdot 10^{-2}$	1.00	0.99	1.00
$6.25 \cdot 10^{-3}$	1.00	1.00	1.00

Table 5.2: Efficiency indices for the estimated error for the non-dissipative (left) and dissipative (right) formulations.

The relative errors, for h-refinement in space and time, measured in the QOI J_H are shown in Fig. 5.2 for the centered formulation and the dissipative formulation. Additionally, the convergence rates, are shown in table 5.1. One can observe convergence rates of h^{2p} and h^{2p+1} for the centered and dissipative formulations, respectively. Note, that for even polynomial degrees some superconvergence phenomenon occurs in case of the centered formulation. This is also known to occur for the error measured in the L^2-norm (see [28]). For the centered flux case, the rate is in agreement with the *a priori* estimate (5.23). The convergence rates from

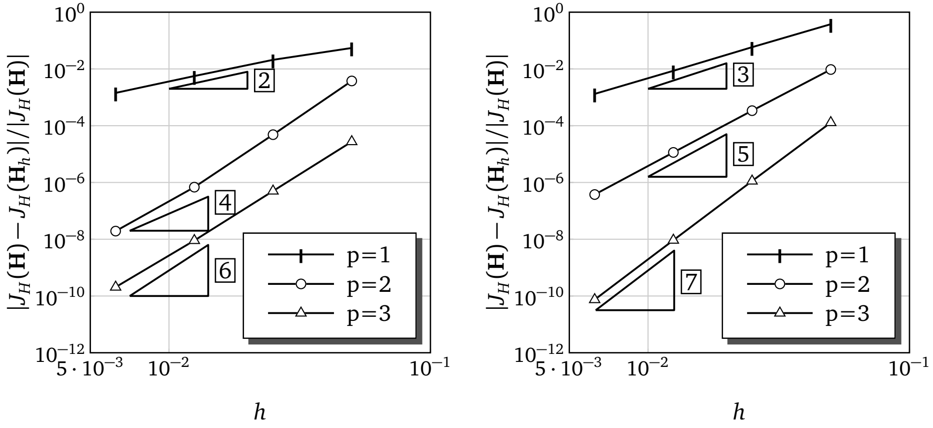

Figure 5.2: Relative error measured in the QOI functional J_H for the non-dissipative centered flux formulation (left) and for the dissipative formulation (right), for simultaneous refinement of the spatial- and temporal stepsizes.

(5.23) are reflected also in the convergence-rates of the spatial- and temporal parts $\mathcal{E}_s$ and $\mathcal{E}_t$ in the error representation (5.12). Their convergence rates are also displayed in table 5.1. The spatial indicators converge with rates of h^{2p+1} and h^{2p} for the dissipative and centered formulations, respectively. In contrast, the temporal indicators converge with a rate of Δt^{2p} for both formulations.
In order to demonstrate the efficiency of the *a posteriori* error estimate (5.12), efficiency indices $I_{eff} = \mathcal{E}/|J_H(\mathbf{H}) - J_H(\mathbf{H}_h)|$ are displayed in table 5.2. All efficiency indices are close to one, which is expected, given the simplicity of the considered problem.

5.5.2 Examples with Goal-Oriented Space-Time hp-Adaptivity

In order to demonstrate the effectiveness of the proposed error estimator in the context of goal-oriented space-time hp-adaptivity, we have extented the adaptive algorithm from [5].

Adaptive Algorithm

In section 3.4.2 we have employed an adaptive algorithm, where the adaptation procedure SOLVE - ESTIMATE - MARK - REFINE has been applied locally for each time-slab $\mathcal{I}_n \times \Omega$. This raises however difficulties with the adjoint error estimator from (5.14). For evaluation of the error indicators in time-slab n, an approximation to the dual solution $\mathbf{z}$ is needed. Recalling, that the dual-problem is running backwards in time, in order to obtain $\mathbf{z}$, the dual problem needs to be solved from time $t = T$ to $t = t_n$. To this end, we will instead use a global algorithm, which has been successfully employed in the context of error-controlled h-adaptivity with the DWR method for time-dependent problems, for example for the wave equation in [7] and [5].

Given a discretization of the entire space-time domain at iteration m, consisting of a global space-time triangulation $\mathcal{S}^m = \left\{\mathcal{S}_n^m(\mathcal{I} \times \Omega)\right\}_{n=1}^{N_m}$ and a set of polynomial degree vectors $\mathbf{p} = \{\mathbf{p}^m\}_{n=1}^{N_m}$:

- SOLVE PRIMAL: Solve the entire time-dependent problem on the current discretization and save the solution for each time-slab.
- ESTIMATE - MARK - REFINE: Solve the entire time-dependent dual problem using the same discretization:
  For each time-slab $\mathcal{I}_n \times \Omega$ $n = N_m, \dots, 1$:
  - SOLVE DUAL: Solve the dual problem using $\mathcal{S}_n^m(\mathcal{I} \times \Omega), \widetilde{\mathbf{p}}_n = \mathbf{p}_n + 1$.
  - ESTIMATE: Load the saved solution $\mathbf{u}_h^n$ and evaluate the contribution $\mathcal{E}_n$ to the error representation (5.12) and the error indicators in (5.14) (isotropic refinement with respect to space), or (5.15) (anisotropic refinement in space).
  - MARK (*global refinement in time*): Apply the strategy described in [5], which aims to achieve an equal distribution of error. Within this strategy, the goal is to obtain

    $$\beta_s \frac{\mathrm{TOL}\Delta t_n}{N_K T} \leq \mathcal{E}_{s,K}^n \leq \alpha_s \frac{\mathrm{TOL}\Delta t_n}{N_K T}, \quad \beta_t \frac{\mathrm{TOL}}{N_m} \leq \mathcal{E}_t^n \leq \alpha_t \frac{\mathrm{TOL}}{N_m}, \tag{5.28}$$

    where N_K denotes the number of elements in the spatial triangulation. To this end, for the purpose of spatial refinement, all space-time elements $\mathcal{I}_n \times K$ which do not fulfill the upper or lower bound (5.28) are chosen for refinement or derefinement, respectively. Analogously, the current time-slab is marked for temporal refinement or coarsening if it does not fulfill (5.28). In this work we have not applied coarsening and chosen $\alpha_s = \alpha_t = 1/2$ and $\beta_s = \beta_t = 0$.

- MARK (*local refinement in time*): In this case, we do not distinguish between spatial and temporal refinement. The goal is to obtain

  $$\beta\frac{\mathrm{TOL}\Delta t_n}{N_K T} \leq \mathcal{E}_K^n \leq \alpha\frac{\mathrm{TOL}\Delta t_n}{N_K T} \quad \mathcal{E}_K^n := \left|R_{h,K}(\mathbf{u}_h, \boldsymbol{\eta}^*)\right|,$$

  were we chose $\alpha = 1$ and $\beta = 0$.

- REFINE (*global refinement in time*): If the space-time element is marked for spatial refinement, we carry out spatial p-refinement, if the solution is assumed to be smooth with respect to space: In order to account for anisotropy in the solution, we enrich the polynomial degree p_d in direction $d \in D = \{\widehat{x}, \widehat{y}, \widehat{z}\}$ by one, provided

  $$\mathcal{E}_{K,d} > \gamma\left(\sum_{d' \in D, d' \neq d} \mathcal{E}_{K,d'}\right), \tag{5.29}$$

  holds true. It turned out, that a reasonable choice for γ is 0.2. If the solution is assumed to be non-smooth with respect to space, we employ isotropic h-refinement by splitting the hexahedron in each direction. Furthermore if the time-slab is marked for temporal refinement, we raise the temporal polynomial degree by one, if the solution is assumed to be smooth. Otherwise we split the time-interval $\mathcal{I}_n$, where the spatial part of the discretization is identical for both of the newly created time-slabs.

- REFINE (*local refinement in time*): Given a space-time element marked for refinement, we employ local temporal refinement, if the temporal part of the error-indicator fulfills the anisotropy criterion (5.29) with $d = t$ where $D = \{t, \widehat{x}, \widehat{y}, \widehat{z}\}$. If the solution is supposed to be smooth with respect to time, we perform p-refinement, and otherwise h-refinement. The spatial part of the discretization is treated as in the case of global refinement in time.

Now, the discretization for the next iteration has been obtained $\mathcal{S}^m$. If $\left|\sum_{n=1}^{N_m} \mathcal{E}_n\right| > \mathrm{TOL}$, goto SOLVE.

For the waveguide-parts of the computational domain, we employ essentially a one dimensional variant of the described algorithm. Furthermore in the waveguide domain, we generally employ p-refinement with regard to space and time, since the solution is expected to be smooth there in the temporal and axial directions.

Waveguide Transmission - Adaptive

We consider the propagation of a broadband TE$_{10}$-mode in a long homogeneous rectangular waveguide ($\varepsilon = \mu = 1$) with cross-section $\mathcal{S}_w := [0, 20] \times [0, 10]$. The computational domain is choosen as $\Omega_D := \mathcal{S}_w \times [0, 2400]$, where the all lengths are given in units of mm. The computational domain Ω_D is discretized with hexahedral elements of edge length 10mm. For realizing the two waveguide ports Γ_w^1 at $z = 0$ and Γ_w^2 at $z = 2400$, Ω_D is extended at the ports with two waveguide domains Ω_w^1 and Ω_w^2, which are choosen to be sufficiently long for a reflection free realization of the ports, using the method proposed in chapter 4. The problem under consideration is (4.16) and the excitation is choosen at the waveguide-port Γ_w^1 as the function $g(t - t_o)$ from (4.15). The frequency range is determined by $f_1 = 10.86$ GHz and $f_2 = 14.24$ GHz. Further, the time-offset t_o corresponds to 20 periods at the center-frequency $(f_1 + f_2)/2$.
The QOI is the magnitude of the (complex) S_{21}-parameter $S_{21} = b_2/a_1$ at $f = 13.6978$ GHz. The magnitude of the incoming modal-coefficient $|a_1|$ can be computed exactly using the excitation (see (4.13)). Thus, for the purpose of error estimation, we choose the linearization of the functional

$$J(\mathbf{H}) = \left| \int_0^T \int_{\Gamma_w^i} \mathbf{n} \times (\mathbf{n} \times \mathbf{H}) \cdot \mathbf{h}_{1\mathrm{TE}} e^{i\omega t} \, \mathrm{d}S \, \mathrm{d}t \right|$$

around the discrete solution $\mathbf{H}_h$, which we denote by $J'(\mathbf{H}_h; \mathbf{H})$. The dual problem is in this case

$$\begin{aligned}
&-\varepsilon \partial_t \mathbf{z}_E + \nabla \times \mathbf{z}_H = 0 \\
&-\mu \partial_t \mathbf{z}_H - \nabla \times \mathbf{z}_E = 0 \ \text{ in } \Omega \\
&\mathbf{n} \times \mathbf{z}_E = 0 \text{ on } \partial\Omega \\
&[\![\mathbf{z}_E]\!]_T = \mathbf{j}_H \ \text{ on } \Gamma_w^2 \\
&\mathbf{z}_E(t = T) = 0, \mathbf{z}(t = T) = 0 \ \text{ in } \Omega,
\end{aligned} \tag{5.30}$$

where

$$J'(\mathbf{H}_h;\mathbf{H}) = \int_0^T \int_{\Gamma_w^2} \mathbf{j}_H \cdot \mathbf{H} \, \mathrm{d}x \, \mathrm{d}t. \tag{5.31}$$

In Fig. 5.3, we depict the convergence of the exact errors of the QOI, the estimated

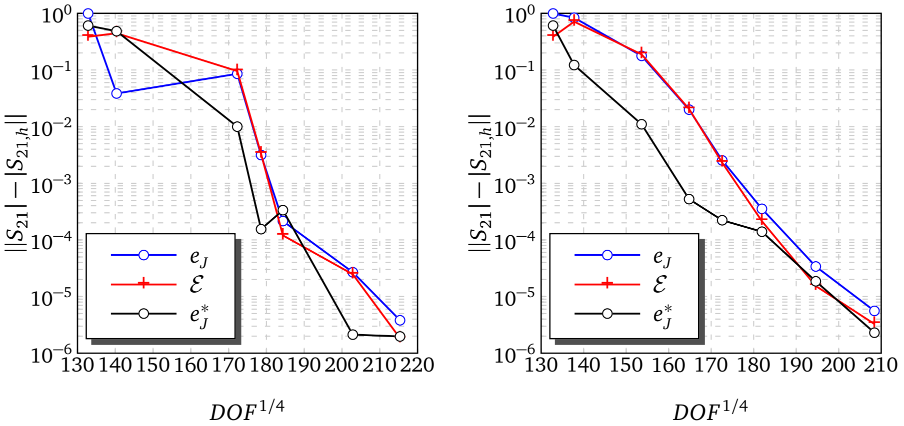

Figure 5.3: Left: Convergence of the exact, estimated and postprocessed errors e_J, $\mathcal{E}$ and e_J^* of $|S_{21}|$ for p-adaptive refinement with global refinement with respect to time. Right: Convergence of the same quantities with local refinement in time.

error and the error of the postprocessed QOI, which is obtained by adding the error estimate to the functional value. The data shown on the left has been obtained by applying the p-adaptive version of the adaptive algorithm of section 5.5.2, employing global refinement with respect to time. The data on the right in contrast has been obtained by applying local refinement with respect to time. In both cases we have employed the dissipative formulation. Both algorithms yield exponential convergence of the errors with respect to the number of degrees of freedom, where the algorithm with local refinement in time converges only slightly faster than the global refinement variant, which is surprising given the structure of the

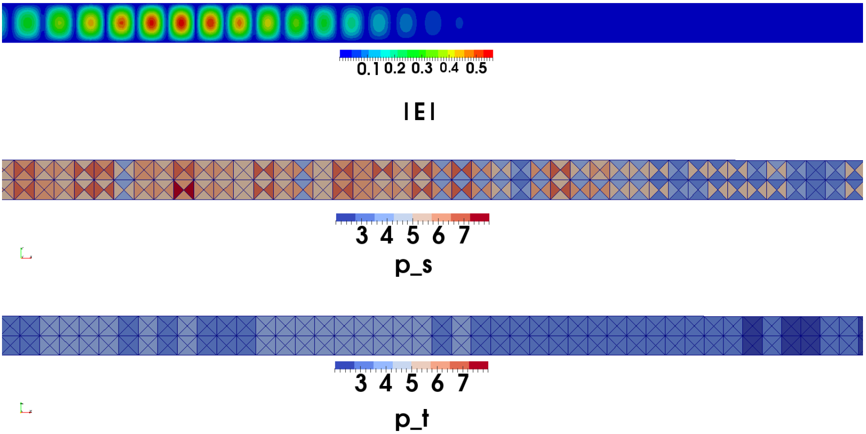

Figure 5.4: From top to bottom: Magnitude of the electric field, spatial polynomial degrees and temporal polynomial degrees at time $t = 5.24$ ns.

problem. However, for the local-in-time refinement algorithm, the error decreases in a smoother way in comparison to the global-in-time refinement. In figure 5.4 we depict the solution $\mathbf{E}$, the spatial polynomial degree distribution and the temporal polynomial degree distribution at time $t = 5.24$ ns, obtained with the algorithm allowing local refinement with respect to time. One can observe, that spatial and temporal refinement are concentrated in the area of the pulse. Furthermore spatial refinement is stronger in axial direction than in the transversal directions, which indicates that the criterion for anisotropic refinement (5.29) based on the anisotropic error indicators (5.15) is effective in this case.

Scattering by a PEC Cube

We consider the scattering of a plane wave $\mathbf{E}_{inc} = g(\mathbf{e}_x \cdot \mathbf{x} - t - 3.5)\mathbf{e}_y$ from an axis aligned PEC cube with edge length 1. The computational domain is chosen as $\Omega = [-21/2, 21/2]^3 \backslash [-1/2, 1/2]^3$ and the function g is given by (4.15), containing the frequency range determined by $f_1 = 1/2$ and $f_2 = 3/2$. We choose $\varepsilon = \mu = 1$ and solve the scattered field problem (2.11) using the dissipative formulation until $T = 12$, once employing the adaptive algorithm of section 5.5.2 without and once with local-in-time refinement. The initial discretization consists of 11472 elements in space, using basis functions constant in the spatial directions and linear in time-direction. The spatial mesh size of the elements is about $h = 1/4$ at the boundary of the scatterer.

As QOI we choose the backscattering-RCS (direction $\mathbf{x} = -\mathbf{e}_x$) at $\omega = 2\pi$, given by

$$\sigma(\phi,\theta;\omega) = \lim_{r\to\infty} 4\pi r^2 \frac{|\underline{\mathbf{E}}^{\mathrm{scfar}}(r,\phi,\theta;\omega)|^2}{|\underline{\mathbf{E}}^{\mathrm{inc}}(r,\phi,\theta;\omega)|^2}.$$

Since the incident field is known, its amplitude $|\underline{\mathbf{E}}^{\mathrm{inc}}(r,\phi,\theta;\omega)|^2$ can be computed exactly by employing the Fourier transform with respect to time. Thus, we consider the nonlinear QOI-functional

$$J(\mathbf{u}) = \frac{1}{4\pi}\left|\int_0^T \int_S [\mathbf{x}\times(\mathbf{x}\times(\mathbf{n}\times\mathbf{H})) + \mathbf{x}\times(\mathbf{E}\times\mathbf{n})]\, e^{i\kappa\mathbf{x}\cdot\mathbf{y}+i\omega t}\,\mathrm{d}S(\mathbf{y})\,\mathrm{d}t\right|^2. \quad (5.32)$$

Since the surface integral in (5.32) yields the same value for any surface S enclosing the scatterer, it can be reformulated as a volume integral, by averaging it over a family of parametrized surfaces $S(a)$, $a \in [0,1]$ (see for a detailed discussion [13], section 11.5.3), such that we obtain

$$J(\mathbf{u}) = \frac{1}{4\pi}\left|\int_0^T \int_0^1 w(a)\,\mathrm{d}a \int_{S(a)} [\mathbf{x}\times(\mathbf{x}\times(\mathbf{n}\times\mathbf{H})) + \mathbf{x}\times(\mathbf{E}\times\mathbf{n})]\, e^{i\kappa\mathbf{x}\cdot\mathbf{y}+i\omega t}\,\mathrm{d}S(\mathbf{y})\,\mathrm{d}t\right|^2. \quad (5.33)$$

We choose $S(a)$ as spherical surfaces with radius $(\sqrt{3}+1)/2 \le R \le (\sqrt{3}+1)/2 + \delta$ where $\delta = 0.4$. The weight function $w(a)$ is choosen as a smooth cut-off function with width equal to δ. For the pupose of error estimation, we choose the linearization $J'(\mathbf{u}_h;\mathbf{u})$ of the volume based functional $J(\mathbf{u})$ from (5.33). Then, the dual problem is of the form

$$\begin{aligned}
&-\varepsilon\partial_t \mathbf{z}_E + \nabla\times\mathbf{z}_H = \mathbf{J}_E\\
&-\mu\partial_t \mathbf{z}_H - \nabla\times\mathbf{z}_E = \mathbf{J}_H \ \text{ in } \Omega\\
&\mathbf{n}\times\mathbf{z}_E = 0 \text{ on } \Gamma_{\mathrm{PEC}}\\
&\mathbf{n}\times\mathbf{z}_E - \sqrt{\mu/\varepsilon}\,\mathbf{n}\times(\mathbf{n}\times\mathbf{z}_H^{sc}) = 0 \text{ on } \Gamma_0\\
&\mathbf{z}_E(t=T) = 0, \mathbf{z}(t=T) = 0 \ \text{ in } \Omega,
\end{aligned} \quad (5.34)$$

where Γ_{PEC} is the boundary of the scatterer and Γ_0 the exterior boundary.

Since an analytical solution is not available for this problem, we take as a reference solution the RCS σ_{BEM} obtained with a boundary element method. The surface mesh of the PEC cube, used for obtaining the reference solution consists of 40 triangles per wavelength using third order basis functions. In Fig. 5.5 we depict the relative error $|\sigma_{BEM} - \sigma_h|/\sigma_{BEM}$, the relative estimated error $\mathcal{E}/\sigma_{BEM}$ and the relative error of the postprocessed QOI $|\sigma_{BEM} - \sigma_h + \mathcal{E}|/\sigma_{BEM}$ in logarithmic scale versus the number of degrees of freedom in an algebraic scale. One can observe exponential convergence of the error for the considered *hp*-adaptive algorithms. Clearly, the algorithm allowing local-in-time refinement is significantly more economical in terms of degrees of freedom. For the first iteration, the primal and dual solutions where likely under-resolved. In this preasymptotic regime the error estimator is not expected to work well as the numerical solution fails to represent signicicant features of the true solution. For the subsequent iterations the error is estimated quite well with efficiency-indices between 0.7 and 1.5.

The magnitude of the discrete solution $\mathbf{E}_h$ and the approximate dual solution $\mathbf{z}_E$ as

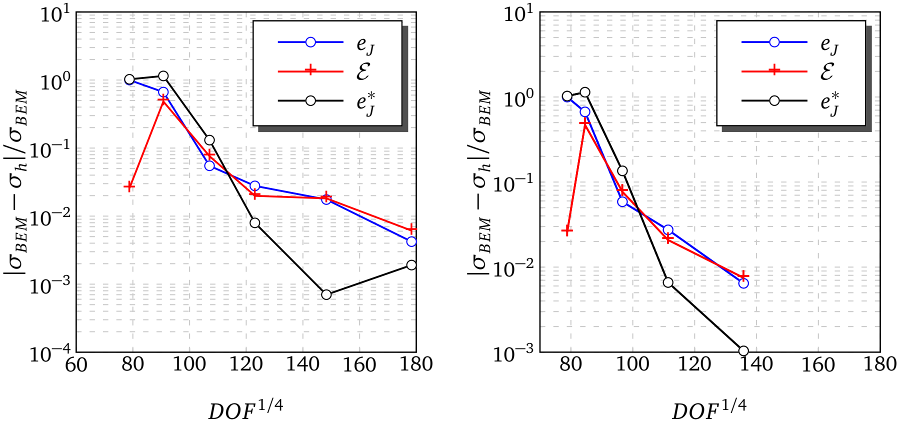

Figure 5.5: Relative error e_J, relative error estimate $\mathcal{E}/\sigma_{BEM}$ and relative error of the postprocessed solution e_J^*/σ_{BEM} in the backscattering RCS, obtained with the global refinement in time (left) and local refinement in time (right) adaptive algorithms.

well as the spatial and temporal discretizations are depicted for two time instants in figure 5.6.

First one can observe (Fig. 5.6, top row, left), that the solution features singularities at the edges of the cube. The refinement algorithm applies spatial h-refinement at the singular edges (third row). Away from the singularities, p-refinement is applied, which is more pronounced in direction of propagation of the solution. Furthermore, the magnitude of the dual-solution is particularly large in the region enclosed by the support of the QOI-functional (in sperical coordinates (R, θ, ϕ): $0 \leq R \leq (\sqrt{3}+1)/2$, $0 \leq \theta \leq \pi$, $0 \leq \phi < 2\pi$). Recalling the structure of the *a posteriori*-error estimator (5.12), the dual solution acts as a weight on the residual, which leads to the concentration of refinement in this region. This also holds for refinement with respect to time (see figure 5.6, bottom row). The role of the dual-solution as a weight on the residual is also illustrated by the significantly under-resolved field (5.6, top right) outside the region enclosed by the support of the RCS functional. Clearly, if the objective was to reduce a global error norm, then the adapted mesh at time $t = 7$ ns would look very different. This is in line with the comment made at the beginning of this chapter on how goal-oriented adaptivity can reduce computational resources for the accurate computation of QOI. Finally it is noted, that the spatial part of the discretization, obtained with the algorithm featuring global refinement in time is similar. However, most time-slabs were refined to polynomial degree $p_t = 2$ in time, which leads to larger number of degrees of freedom compared to the algorithm allowing local refinement in time.

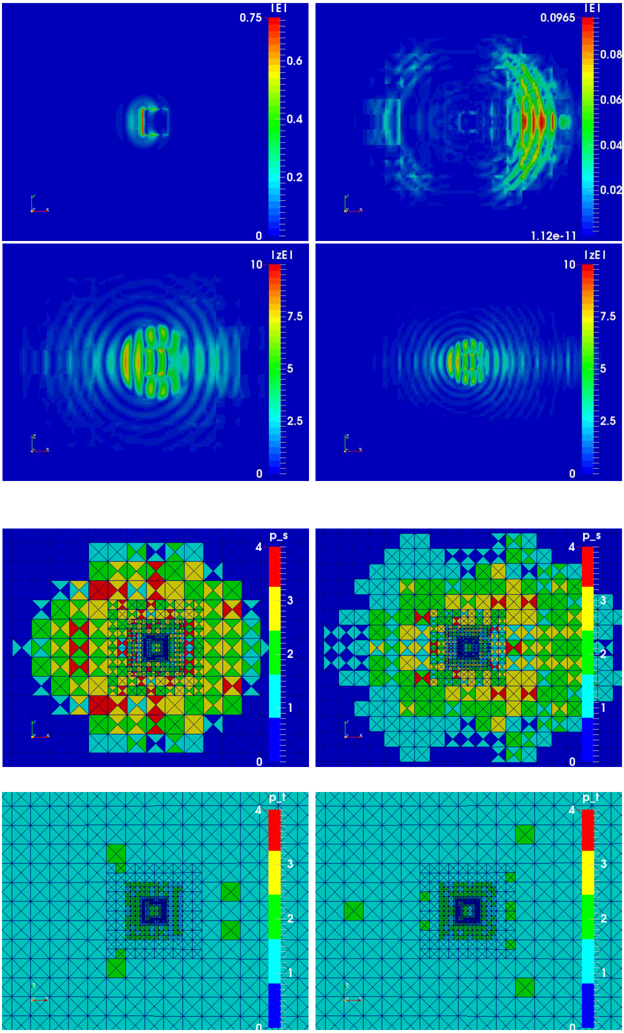

Figure 5.6: From top to bottom row, left column $t = 1.5$, right column $t = 7$: Magnitude of the discrete solution $|\mathbf{E}_h|$, magnitude of the discrete dual solution $|\mathbf{z}_E|$, spatial polynomial degrees visualized using the tensor product visualization from Fig. 3.9, temporal polynomial degrees.

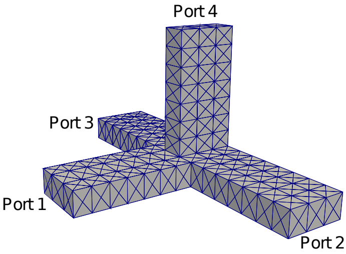

Figure 5.7: Magic-T splitter with initial mesh, dividing incoming waves at port 1 into two waves of equal amplitude at ports 2 and 3.

This numerical experiment deals with the simulation of a so called magic-T waveguide splitter, depicted in Fig. 5.7. It has the purpose to split the incoming TE_{10}-wave at port 1 into two waves of equal amplitude at ports 2 and 3. The waveguide cross-section S_w has dimensions 50mm x 20mm. At the four ports, the computational domain is extended with sufficiently long waveguide domains for reflection free realization of the waveguide ports. At port 1 with port surface Γ_w^1, we apply an excitation using (4.14) with the excitation function $g(t - t_o)$ from (4.15). The frequency range is chosen according to $f_1 = 3.4$ GHz and $f_2 = 5.9$ GHz. The time-offset t_o corresponds to 10 periods at $f_c = (f_1 + f_2)/2$. The QOI is the magnitude of the transmission parameter $S_{21} = b_2(f^*)/a_1(f^*)$ at frequency $f^* = 5.501$GHz. Proceeding analogously as in section 5.5.2, the dual problem is given by (5.30).

As an initial discretization, we employ the mesh shown in Fig. 5.7, which consists of 93 hexahedra with polynomial degrees $p_t = 1$, $p_y = p_y = p_z = 2$. The simulation time is $T = 7$ ns and the initial time-step size is $\Delta t = 1/40(f_1 + f_2)$. We have employed the adaptive algorithm of section 5.5.2 using the dissipative formulation with global and local refinement in time. The algorithm was provided with the edges featuring singularities and carried out spatial h-refinement for elements, located at singular edges and p-refinement in all other parts of the computational domain. With respect to time, p-refinement is applied.

We have obtained a reference solution with the commercial FIT code CST MICROWAVE STUDIO® for the QOI $|S_{21}|$, using a mesh with 200 cells per wavelength. In Fig. 5.8 we show convergence of the relative error $e_J = ||S_{21}| - |S_{21,h}||/|S_{21}|$, the relative estimated error $|\mathcal{E}|/|S_{21}|$ and the relative error in the postprocessed QOI $||S_{21h}| + \mathcal{E} - |S_{21}||/|S_{21}|$ for the algorithms with global and local refinement in time. For both algorithms, we observe exponential convergence with respect to the number of degrees of freedom. Furthermore, the *a posteriori* error estimates are very accurate. This leads to significant gains in terms of accuracy by postprocessing.

For this example, there are essentially no savings in terms of degrees of freedom for the algorithm employing local refinement in time. We attribute this to the small size of the computational domain in terms of wavelength. In addition, the primal and dual solutions occupy almost the entire computational domain as depicted in figure 5.10 for time $t = 2.25$ ns. This leads to refinements (in space and time) which are not localized as it is for example the case for the scattering problem in section 5.5.2, where local in time refinement led to a significantly lower number of degrees of freedom.

In Fig. 5.9, we depict the convergence of the magnitude of the S-parameters $|S_{11}|$ and $|S_{21}|$ as a function of frequency for all adaptation cycles. Even though, the discretization was adapted towards the QOI-functional $|S_{21}(f^* = 5.501\text{GHz})|$, one can observe errors below the estimated error, at least for $f \leq f^*$. The results for scattering parameter S_{11} are reasonably accurate as well. However, it can be observed from Fig. 5.9 that convergence for the error in $|S_{11}|$ is not as smooth as for $|S_{21}|$. This is expected as $|S_{11}|$ is not included in the QOI functional.

5.6 Conclusions

We have derived an *a posteriori*-error estimator for QOI functionals. The error estimator fits into the established mathematical framework of adjoint based error estimates [8, 19]. The methodology has been applied to a wide range of problems and types of discretizations, including the wave equation [5, 7] and the time-harmonic Maxwell's equations [32]. The application to the time-dependent Maxwell's equations has however not been reported to date.

Furthermore, we have carried out the *a priori* error analysis, explicit in h and p, for QOIs approximated by the space-time discontinuous Galerkin method introduced in chapter 3. The analysis yielded improved convergence rates like $\mathcal{O}(h^{2p})$ for QOIs, compared to estimates in the energy norm ($\mathcal{O}(h^p)$). This is a well known phenomenon and *a priori* error estimates can be found in the literature already for other types of problems (see e.g. [19], [22], [30]), but not for Maxwell's equations and the considered discretization.

We have validated the *a priori* estimate in a simple numerical test-case. Further we have applied the derived error estimator in the context of goal-oriented hp-adaptivity in space and time. The derived error estimator provided accurate

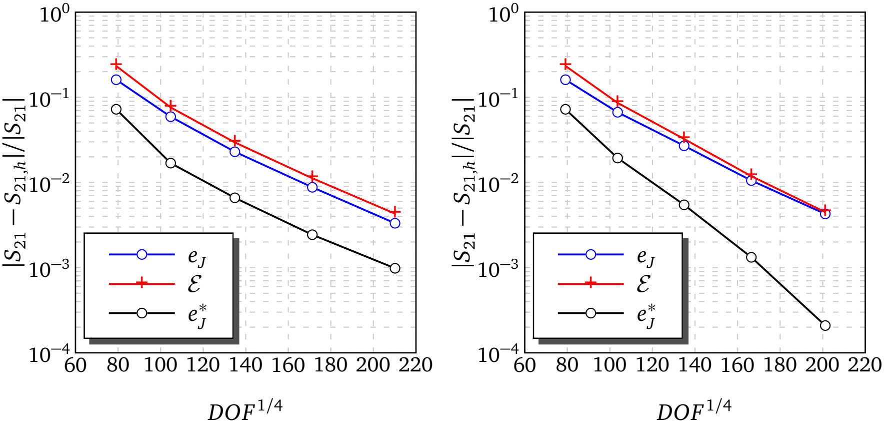

Figure 5.8: Left: Convergence of the exact, estimated and postprocessed errors of the QOI $|S_{21}(f^*)|, f* = 5.501$ GHz for hp-adaptive refinement with global refinement with respect to time. Right: Convergence of the same quantities with local refinement in time.

estimates of the error. For the test cases considered, we obtained exponential convergence rates with respect to degrees of freedom.

The adaptive algorithm algorithm is an extension of the algorithm used for goal-oriented adaptivity in [5]. However, it was supplied with information of geometry induced singularities. The algorithm based the decision, if h- or p-refinement should be carried out, on this information. Thus, the development of a fully automatic hp-adaptive algorithm for goal-oriented adaptivity should be addressed in future work. Another topic, which should be addressed is the extension of goal-oriented adaptivity to multiple QOIs. To this end, the approach reported in [23] should be applicable. Furthermore, the implementation should be extended to allow anisotropic h-refinement, which could also be controlled by the anisotropic error indicators from (5.15).

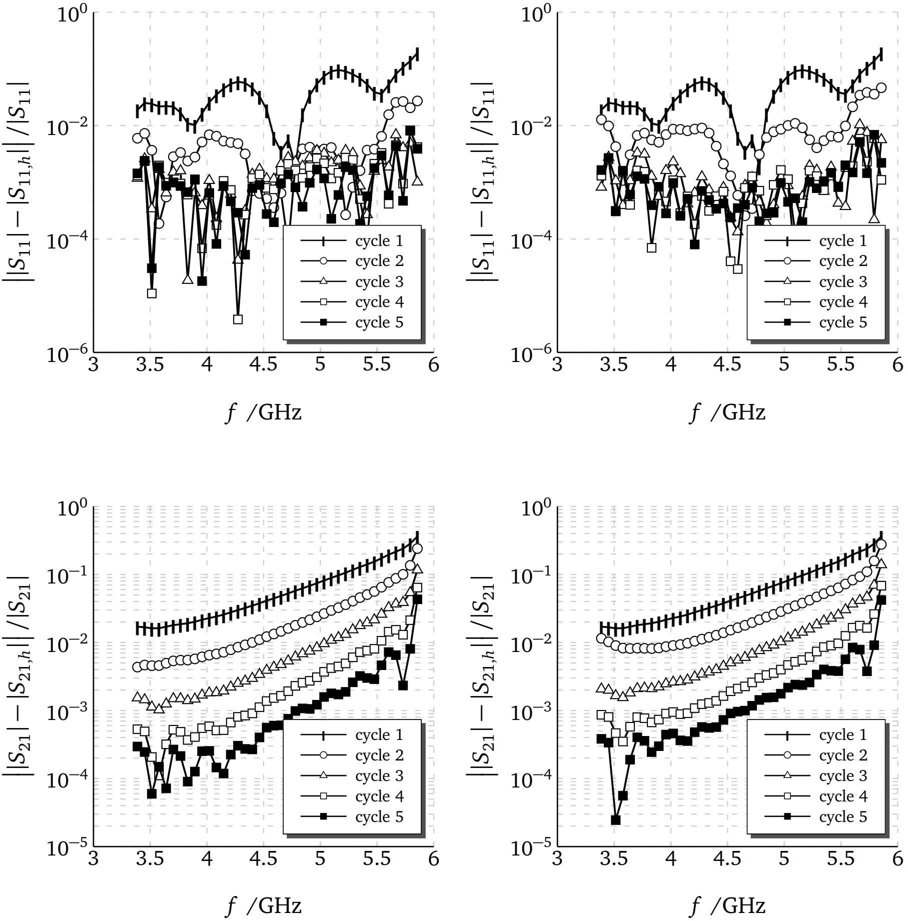

Figure 5.9: Left: Convergence of the errors in $|S_{11}|$ (top) and $|S_{21}|$ (bottom) as a function of frequency for hp-adaptive refinement with global refinement with respect to time. Right: Convergence of the same quantities with local refinement in time.

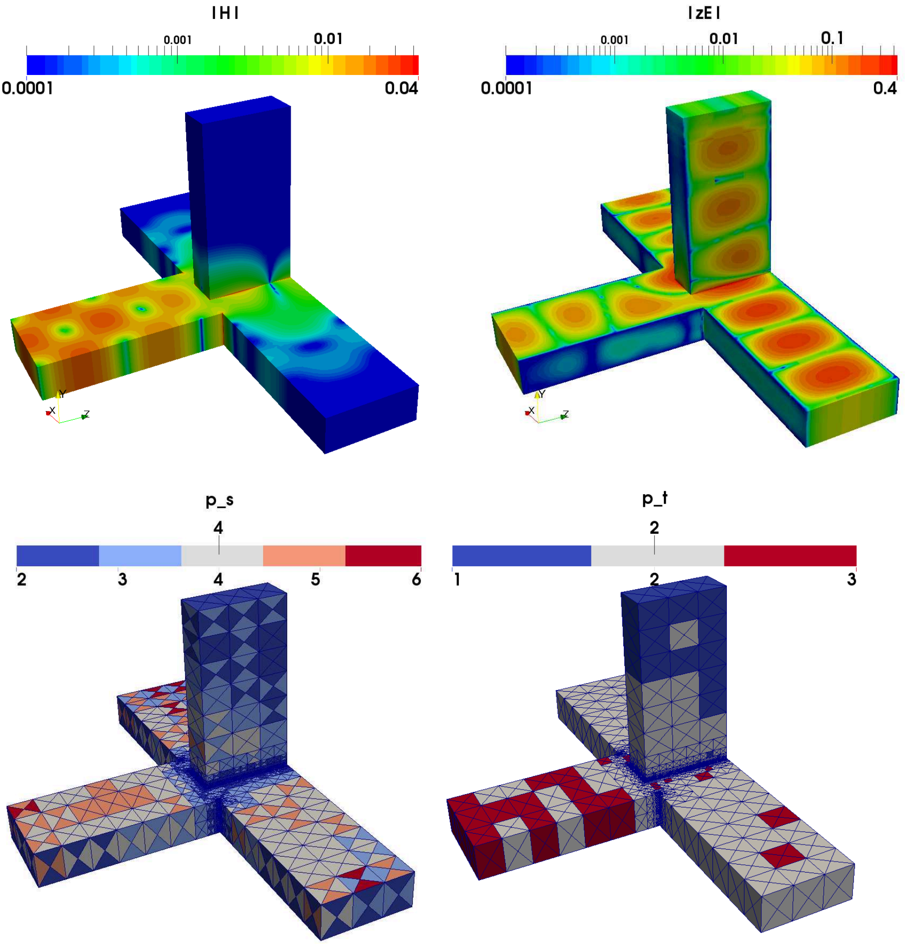

Figure 5.10: Magnitude of the magnetic field $\mathbf{H}_h$ and the approximate dual solution $\mathbf{z}_E$, spatial and temporal polynomial degrees at time $t = 2.25$ ns. Top left: Magnetic field in logarithmic scale. Top right: Dual solution in logarithmic scale. Bottom left: Spatial polynomial degrees using the tensor product visualization of Fig. 3.9. Bottom right: Temporal polynomial degrees.

6 Conclusions

In this thesis, an adaptive error controlled high-order discretization method for Maxwell's equations has been established

In chapter 2, the physical setting was introduced and the governing Maxwell's equations were stated.

In chapter 3 a space-time discontinuous Galerkin method was devised. It allows for local adaptation of the spatial and temporal mesh-size and the degrees of the approximating polynomials. It was shown that the method is unconditionally stable and energy conserving, as long as the spatial part of the discretization is not changed between time-slabs. Furthermore, it was shown, that the method can be implemented in a matrix-free way, such that the complexity of the evaluation of the residual within an iterative solution method can be done with $\mathcal{O}(p^4)$ and $\mathcal{O}(p^5)$ operations for affine and non-affine elements, respectively. To this end, sum-factorization techniques [42] were applied for evaluating integrals of tensor product basis functions.
Under the restriction that no local refinement in time is present in the discretization, the full *hp*-error analysis was carried out. The analysis extends techniques introduced in [20] and [11] to the context of the developed space-time *hp*-discontinuous Galerkin method.
Also under the assumption of no local refinement in time, a guaranteed *a posteriori* error bound on the iteration error was devised. It allows for controlling the iteration error. Thus, the linear systems, arising due to the implicit discretization, can be solved inexactly, without compromising the overall accuracy. Provided that an error bound on the discretization error is available, discretization and iteration errors can be balanced.

For the efficient discretization of waveguide structures, the developed space-time Galerkin method was complemented with a set of specific basis functions. They consist of waveguide-modes in transversal- and polynomials in the axial- and temporal directions. By construction this approach is a natural extension of the presented method and inherits in particular its stability and high-order accuracy properties. Since waveguide ports are modeled as 1D structures essentially, the introduction of the waveguide mode basis leads to a greatly reduced number of

$3M(p+1)^2$ degrees of freedom per element compared to $6(p+1)^4$ in case of the classical tensor product polynomial basis on hexahedra. This allows to simply extent the computational domain at waveguide ports, in order to model an open boundary. The idea of extending the computational domain with a 1D model is not original, and has also been applied in [50]. However, there the authors consider a coupled 3D-1D problem, which is conceptually different and in contrast to the approach presented in chapter 4 more difficult to analyze in terms of stability and accuracy.

Chapter 5 dealed with the error controlled hp-adaptive approximation of quantities-of-interest. Prominent examples are S-parameters or farfield quantities like the radar cross section. For the purpose of error control, an *a posteriori* error estimator for quantity-of-interest functionals was derived. The error estimator fits into the mathematical framework of adjoint-based error estimators [8, 19]. In order to be able to steer anisotropic refinements, a splitting of the error indicators was proposed. It relies on the tensor-product structure of the approximating polynomials. While the splitting is conceptually simple, it allows for a reliable detection of anisotropy in the error.
Furthermore, it was shown, that an improved *a priori* error bound of rate $\mathcal{O}(h^{2p})$ holds for the convergence of QOIs. To this end, techniques were employed, which extend those from [22] to the developed discretization of the Maxwell problem. The analysis showed, that for obtaining the improved convergence rates, not only the solution to Maxwell's equations is required to be sufficiently smooth, but also the solution of the respective dual problem. Since the QOI enters the dual problem in the shape of a source term, its smoothness is also affected by the particular choice of QOI. This leads to the conclusion, that QOIs should be carefully selected, in order to obtain the best possible rate of convergence.
The effectiveness of the developed error estimator for QOIs in the context of the space-time Galerkin method was demonstrated by its application to a series of test problems. Thereby, exponential convergence rates were obtained for the QOIs under consideration. Furthermore, the error estimator yielded accurate estimates of the error in the QOIs.

6.1 Outlook

Several aspects could be adressed in future research.

One important aspect concerning the applicability of the presented method to large scale problems is the solution of the linear systems. While the proposed

preconditioner (3.73) consisting of the time-derivative terms in the bilinear-form showed to be quite effective for small time-steps, the number of iterations increases drastically with the size of the time-step.
From a practical point of view, this prohibits the application of larger time-steps, which otherwise the unconditional stability and high-order accuracy of the proposed method allows for. Thus, the question of preconditioning should be addressed. One possible approach could be the use of an explicit time-stepping method as a preconditioner [34] or smoother within a multilevel algorithm [62, 63]. This would still allow for a computationally efficient matrix-free implementation of the method.
Another aspect regarding the discretization method, is the extension of the *a priori* error analysis to the general case of discretizations with local-hp-refinement in time. To this end, lemma 3.2.2 needs to be extended, which is an open problem. The remaining part of the error analysis is expected to pose no major problems.

Regarding adaptivity, the implementation of a fully automatic *hp*-refinement algorithm, would certainly be useful, also for goal-oriented adaptivity. In the context of this work, a strategy based on smoothness estimation was already implemented. The strategy is computationally very efficient, and it can be straight-forwardly generalized to anisotropic smoothness estimation. However, experience shows that smoothness estimation does not yet exhibit the robustness, that is required for driving mesh adaptation for arbitrary application problems. Further research into this direction is necessary.
A promising alternative is to extend the *hp*-strategy from [57] to goal-oriented refinement. This strategy builds on the concept of reference solutions [13, 59], which is known to deliver robust refinements.

Bibliography

[1] M. Abramowitz and I. A. Stegun. *Handbook of mathematical functions: with formulas, graphs, and mathematical tables*. Number 55. Courier Dover Publications, 1972.

[2] G. Akrivis, C. Makridakis, and R. H. Nochetto. Galerkin and Runge–Kutta methods: unified formulation, a posteriori error estimates and nodal superconvergence. *Numerische Mathematik*, 118(3):429—456, 2011.

[3] I. Babuska and M. Suri. The hp version of the finite element method with quasiuniform meshes. *Modélisation mathématique et analyse numérique*, 21(2):199–238, 1987.

[4] I. Babuška and M. Suri. The p and h-p versions of the finite element method, basic principles and properties. *SIAM review*, 36(4):578–632, 1994.

[5] W. Bangerth, M. Geiger, and R. Rannacher. Adaptive galerkin finite element methods for the wave equation. *Comput. Methods Appl. Math.*, 10(1):3–48, 2010.

[6] W. Bangerth and R. Rannacher. Adaptive finite element techniques for the acoustic wave equation. *Journal of Computational Acoustics*, 9(02):575–591, 2001.

[7] W. Bangerth and R. Rannacher. Adaptive finite element techniques for the acoustic wave equation. *Journal of Computational Acoustics*, 9(02):575–591, 2001.

[8] R. Becker and R. Rannacher. An optimal control approach to a posteriori error estimation in finite element methods. *Acta numerica*, 10(1):1–102, 2001.

[9] S. Beuchler, V. Pillwein, J. Schöberl, and S. Zaglmayr. *Sparsity optimized high order finite element functions on simplices*. Springer, 2012.

[10] S. Brenner and R. Scott. *The mathematical theory of finite element methods*, volume 15. Springer, 2007.

[11] T. Bui-Thanh and O. Ghattas. Analysis of an hp-nonconforming discontinuous galerkin spectral element method for wave propagation. *SIAM Journal on Numerical Analysis*, 50(3):1801–1826, 2012.

[12] G. Cohen, X. Ferrieres, and S. Pernet. A spatial high-order hexahedral discontinuous galerkin method to solve maxwell's equations in time domain. *Journal of Computational Physics*, 217(2):340–363, Sept. 2006.

[13] L. Demkowicz, J. Kurtz, D. Pardo, M. Paszenski, W. Rachowicz, and A. Zdunek. *Computing with hp-ADAPTIVE FINITE ELEMENTS: Volume II Frontiers: Three Dimensional Elliptic and Maxwell Problems with Applications*, volume 2. Chapman & Hall/CRC, 2007.

[14] S. Descombes, S. Lanteri, and L. Moya. Locally implicit time integration strategies in a discontinuous galerkin method for maxwell's equations. *Journal of Scientific Computing*, pages 1–29, 2012.

[15] V. Dolean, H. Fahs, L. Fezoui, and S. Lanteri. Locally implicit discontinuous galerkin method for time domain electromagnetics. *Journal of Computational Physics*, 229(2):512–526, Jan. 2010.

[16] W. Dörfler. A convergent adaptive algorithm for poisson's equation. *SIAM Journal on Numerical Analysis*, 33(3):1106—-1124, 1996.

[17] D. Estep, M. Pernice, D. Pham, S. Tavener, and H. Wang. A posteriori error analysis of a cell-centered finite volume method for semilinear elliptic problems. *Journal of computational and applied mathematics*, 233(2):459–472, 2009.

[18] L. Fezoui, S. Lanteri, S. Lohrengel, and S. Piperno. Convergence and stability of a discontinuous galerkin time-domain method for the 3D heterogeneous maxwell equations on unstructured meshes. *ESAIM: Mathematical Modelling and Numerical Analysis*, 39(6):1149–1176, Nov. 2005.

[19] M. B. Giles and E. Süli. Adjoint methods for PDEs: a posteriori error analysis and postprocessing by duality. *Acta Numerica*, 11:145–236, 2002.

[20] R. Griesmaier and P. Monk. Discretization of the wave equation using continuous elements in time and a hybridizable discontinuous galerkin method in space. *Journal of Scientific Computing*, pages 1–27, 2013.

[21] K. Harriman, D. Gavaghan, and E. Suli. The importance of adjoint consistency in the approximation of linear functionals using the discontinuous galerkin finite element method. 2004.

[22] K. Harriman, P. Houston, B. Senior, and E. Suli. hp-version discontinuous galerkin methods with interior penalty for partial differential equations with nonnegative characteristic form. *Contemporary Mathematics*, 330:89–120, 2003.

[23] R. Hartmann. Multitarget error estimation and adaptivity in aerodynamic flow simulations. *SIAM Journal on Scientific Computing*, 31(1):708–731, 2008.

[24] R. Hartmann and P. Houston. Adaptive discontinuous galerkin finite element methods for the compressible euler equations. *Journal of Computational Physics*, 183(2):508–532, 2002.

[25] R. Hartmann and P. Houston. Adaptive discontinuous galerkin finite element methods for nonlinear hyperbolic conservation laws. *SIAM Journal on Scientific Computing*, 24(3):979–1004, 2003.

[26] R. Hartmann and P. Houston. Symmetric interior penalty dg methods for the compressible navier-stokes equations ii: Goal–oriented a posteriori error estimation. 2005.

[27] J. Hesthaven and T. Warburton. Nodal high-order methods on unstructured grids. *Journal of Computational Physics*, 181(1):186–221, Sept. 2002.

[28] J. S. Hesthaven and T. Warburton. *Nodal discontinuous Galerkin methods: algorithms, analysis, and applications*, volume 54. Springer, 2007.

[29] M. Hintermüller and R. H. Hoppe. Goal-oriented adaptivity in control constrained optimal control of partial differential equations. *SIAM Journal on Control and Optimization*, 47(4):1721–1743, 2008.

[30] P. Houston, C. Schwab, and E. Süli. Discontinuous hp-finite element methods for advection-diffusion-reaction problems. *SIAM Journal on Numerical Analysis*, 39(6):2133–2163, 2002.

[31] P. Houston and E. Süli. hp-adaptive discontinuous galerkin finite element methods for first-order hyperbolic problems. *SIAM Journal on Scientific Computing*, 23(4):1226–1252, 2001.

[32] P. Ingelström and A. Bondeson. Goal-oriented error estimation and h-adaptivity for maxwell's equations. *Computer methods in applied mechanics and engineering*, 192(22):2597–2616, 2003.

[33] J. Jackson. Classical electrodynamics. *Classical Electrodynamics, 3rd Edition, by John David Jackson, pp. 832. ISBN 0-471-30932-X. Wiley-VCH, July 1998.*, 1, 1998.

[34] C. Klaij, J. Van Der Vegt, and H. Van der Ven. Pseudo-time stepping methods for space–time discontinuous galerkin discretizations of the compressible Navier–Stokes equations. *Journal of Computational Physics*, 219(2):622–643, 2006.

[35] C. Koutschan, C. Lehrenfeld, and J. Schöberl. Computer algebra meets finite elements: An efficient implementation for maxwell's equations. *Numerical and Symbolic Scientific Computing: Progress and Prospects*, 1:105, 2011.

[36] F. Kretzschmar, S. M. Schnepp, I. Tsukerman, and T. Weiland. Discontinuous galerkin methods with trefftz approximations. *Journal of Computational and Applied Mathematics*, 270:211–222, 2014.

[37] G. Kristensson. Transient electromagnetic wave propagation in waveguides. *Journal of Electromagnetic Waves and Applications*, 9(5-6):645–671, 1995.

[38] R. J. LeVeque. *Finite volume methods for hyperbolic problems*, volume 31. Cambridge university press, 2002.

[39] M. Lilienthal, U. Römer, and T. Weiland. A posteriori error analysis of the fdtd method, 2014.

[40] M. Lilienthal, S. M. Schnepp, and T. Weiland. Non-dissipative space–time hp-discontinuous galerkin method for the time-dependent maxwell equations. *Journal of Computational Physics*, 275(0):589 – 607, 2014.

[41] Z. Lou and J.-M. Jin. An accurate waveguide port boundary condition for the time-domain finite-element method. *Microwave Theory and Techniques, IEEE Transactions on*, 53(9):3014–3023, 2005.

[42] J. Melenk, K. Gerdes, and C. Schwab. Fully discrete *hp*-finite elements: fast quadrature. *Computer methods in applied mechanics and engineering*, 190(32):4339—-4364, 2001.

[43] J. Melenk and T. Wurzer. On the stability of the boundary trace of the polynomial l2-projection on triangles and tetrahedra. *Computers & Mathematics with Applications*, 2014.

[44] E. Montseny, S. Pernet, X. Ferriéres, and G. Cohen. Dissipative terms and local time-stepping improvements in a spatial high order discontinuous galerkin scheme for the time-domain maxwell's equations. *Journal of Computational Physics*, 227(14):6795–6820, July 2008.

[45] J. Nédélec. Mixed finite elements in $\mathbb{R}^3$. *Numerische Mathematik*, 35(3):315–341, 1980.

[46] J. Nédélec. A new family of mixed finite elements in $\mathbb{R}^3$. *Numerische Mathematik*, 50(1):57–81, 1986.

[47] D. Pardo, L. Demkowicz, C. Torres-Verdin, and M. Paszynski. Two-dimensional high-accuracy simulation of resistivity log ging-while-drilling (LWD) measurements using a self-adaptiv e goal-oriented hp finite element method. *SIAM Journal on Applied Mathematics*, 66(6):2085–2106, 2006.

[48] S. Pernet and X. Ferrieres. HP a-priori error estimates for a non-dissipative spectral discontinuous galerkin method to solve the maxwell equations in the time domain. *Mathematics of Computation*, 76(260):1801–1832, 2007.

[49] S. Piperno. Symplectic local time-stepping in non-dissipative DGTD methods applied to wave propagation problems. *ESAIM: Mathematical Modelling and Numerical Analysis*, 40(05):815—-841, 2006.

[50] C. Potratz, H. Glock, and U. van Rienen. Time-domain field and scattering parameter computation in waveguide structures by GPU-accelerated discontinuous-galerkin method. *Microwave Theory and Techniques, IEEE Transactions on*, 59(11):2788–2797, 2011.

[51] M. Remaki. *Méthodes numériques pour les équations de Maxwell instationnaires en milieu hétérogène*. PhD thesis, Ecole des Ponts ParisTech, 1999.

[52] R. Rieben, G. Rodrigue, and D. White. A high order mixed vector finite element method for solving the time dependent maxwell equations on unstructured grids. *Journal of Computational Physics*, 204(2):490–519, 2005.

[53] G. Rodrigue and D. White. A vector finite element time-domain method for solving maxwell's equations on unstructured hexahedral grids. *SIAM Journal on Scientific Computing*, 23(3):683–706, 2001.

[54] S. Schnepp. *Space-Time Adaptive Methods for Beam Dynamics Simulations*. PhD thesis, TU Darmstadt, 2009.

[55] S. Schnepp, M. Lilienthal, and T. Weiland. Discontinuous galerkin methods with transient hp-adaptation. In *Electromagnetic Theory (EMTS), 2010 URSI International Symposium on*, pages 985–988. IEEE, 2010.

[56] S. Schnepp and T. Weiland. Efficient large scale electromagnetic simulations using dynamically adapted meshes with the discontinuous galerkin method. *Journal of Computational and Applied Mathematics*, pages 4909—-4924, 2012.

[57] S. M. Schnepp. Error-driven dynamical hp-meshes for the discontinuous galerkin method in time-domain. *Journal of Computational and Applied Mathematics*, 270:353–368, 2014.

[58] C. Schwab. *p-and hp-Finite Element Methods: Theory and Applications to Solid and Fluid Mechanics*. Oxford University Press, USA, 1999.

[59] P. Solin, K. Segeth, and I. Dolezel. *Higher-order finite element methods*, volume 41. Chapman and Hall/CRC, 2003.

[60] D. Sármány, M. Botchev, and J. J. van der Vegt. Dispersion and dissipation error in high-order runge-kutta discontinuous galerkin discretisations of the maxwell equations. *Journal of Scientific Computing*, 33(1):47–74, 2007.

[61] A. Taube, M. Dumbser, C.-D. Munz, and R. Schneider. A high-order discontinuous galerkin method with time-accurate local time stepping for the maxwell equations. *International Journal of Numerical Modelling: Electronic Networks, Devices and Fields*, 22(1):77–103, 2009.

[62] J. van der Vegt and S. Rhebergen. hp-multigrid as smoother algorithm for higher order discontinuous galerkin discretizations of advection dominated flows: Part i. multilevel analysis. *Journal of Computational Physics*, 231(22):7537–7563, Sept. 2012.

[63] J. van der Vegt and S. Rhebergen. HP-multigrid as smoother algorithm for higher order discontinuous galerkin discretizations of advection dominated flows. part II: Optimization of the runge–kutta smoother. *Journal of Computational Physics*, 231(22):7564–7583, Sept. 2012.

[64] J. Van der Vegt and H. Van der Ven. Space–time discontinuous galerkin finite element method with dynamic grid motion for inviscid compressible flows: I. general formulation. *Journal of Computational Physics*, 182(2):546–585, 2002.

[65] J. G. Verwer. Composition methods, maxwell's equations, and source terms. *SIAM Journal on Numerical Analysis*, 50(2):439–457, Jan. 2012.

[66] T. Warburton. *Topics in Numerical Differential Equations, CAAM 652*. Lecture Notes, Rice University, Houston, TX, 2011.

[67] T. Weiland. A discretization model for the solution of maxwell's equations for six-component fields. *Archiv Elektronik und Uebertragungstechnik*, 31:116–120, 1977.

[68] T. P. Wihler. An a priori error analysis of the hp-version of the continuous galerkin FEM for nonlinear initial value problems. *Journal of Scientific Computing*, 25(3):523–549, 2005.

[69] K. Yee. Numerical solution of initial boundary value problems involving maxwell's equations in isotropic media. *Antennas and Propagation, IEEE Transactions on*, 14(3):302–307, 1966.

[70] A. Zdunek and W. Rachowicz. A goal-oriented hp-adaptive finite element approach to radar scattering problems. *Computer methods in applied mechanics and engineering*, 194(2):657–674, 2005.

Acronyms

CFL	Courant Friedrichs Levy number.
DG	Discontinuous Galerkin.
DOF	degree of freedom.
FDTD	Finit-Difference Time-Domain method.
FEM	finite element method.
FIT	Finit Integration Technique.
HDG	Hybrid discontinuous Galerkin.
PDE	partial differential equation.
PEC	perfect electrical conductor.
QOI	quantity of interest.
RCS	Radar Cross Section.
SAR	Specific Absorption Rate.

General

$\mathrm{d}S$	surface differential.
$\mathrm{d}x$	volume differential.
Ω	computational domain.
$\partial\Omega$	boundary of Ω.
T	final time.
t	temporal variable.

Electrodynamics

B magnetic flux density measured in the units Vs/m^2.

D electric displacement current measured in the units As/m^2.

E electric field measured in the units V/m.

ε electric permittivity measured in the units As/Vm.

H magnetic field measured in the units A/m.

J current density measured in the units A/m^2.

μ magnetic permeability measured in the units Vs/Am.

ρ charge density measured in the units C/m^2.

σ conductivity measured in the units S/m.

Function Spaces

$\mathbf{H}(curl, \Omega)$ space of $\mathbf{L}^2(\Omega)$ functions with square-integrable curl.

$\mathbf{H}_0(curl, \Omega)$ space of $\mathbf{L}^2(\Omega)$ functions with square-integrable curl and zero tangential trace on $\partial\Omega$.

$\mathbf{L}^2(D)$ vector valued space of square-integrable functions on D.

Discretization and Analysis

$B_h^n(\mathbf{u}_h, \mathbf{w})$ form $C_h^n(\mathbf{u}_h, \mathbf{w}) + S_h^n(\mathbf{u}_h, \mathbf{w}) + D_h^n(\mathbf{u}_h, \mathbf{w})$, for time-slab n.

$\mathbf{z}$ continuous solution to an adjoint problem.

$\mathbf{z}_E$ continuous solution to an adjoint problem, dual to electric field.

$\mathbf{z}_H$ continuous solution to an adjoint problem, dual to magnetic field.

$C_h^n(\mathbf{u}_h, \mathbf{w})$ form for the non-dissipative formulation for problems without local hp-refinement in time, for time-slab n.

$D_h^n(\mathbf{u}_h, \mathbf{w})$ stabilization form of the dissipative formulation for time-slab n.

$\mathbf{E}_h$ discrete solution: electric field.

$\mathbf{H}_h$ discrete solution: magnetic field.

$\mathcal{I}_n \times K$ space-time (macro) element $\mathcal{I}_n = \bigcup_{k=1}^{N_K} I_k^K \times K$.

$\mathcal{I}_k^K \times K$ k-th space-time element for spatial element K.

$\mathcal{I}_n \times \Omega$ n-th time-slab.

$J(\mathbf{v})$ QOI functional.

K spatial element.

$L_h^n(\mathbf{w})$ linear-form for time-slab n, containing source terms (current and data for inhomogeneous boundary condition).

N_K number of space-time elements (or local time-steps) for the spatial element K.

$S_h^n(\mathbf{u}_h, \mathbf{w})$ stabilization-form of the non-dissipative formulation for the general case with local hp-refinement in time, for time-slab n.

$S_K(\mathcal{I}_n)$ temporal part of the local trial-space for the space-time (macro) element $\mathcal{I}_n \times K$.

$T_K(\mathcal{I}_n)$ temporal part of the local test-space for the space-time (macro) element $\mathcal{I}_n \times K$.

$\mathcal{T}_n(\Omega)$ spatial triangulation of Ω for time-slab n.

$\mathcal{S}_n(\mathcal{I}_n \times \Omega)$ space-time triangulation of time-slab n.

$\mathbf{u}_h$ discrete solution: electric and magnetic field.

$\mathbf{V}_h^n$ trial-space for time-slab n $\mathcal{I}_n \times K$.

$V_{h,K}$ local trial-space for the space-time (macro) element $\mathcal{I}_n \times K$.

$\mathbf{W}_h^n$ test-space for time-slab n $\mathcal{I}_n \times K$.

$\mathcal{W}_h$ discrete electromagnetic energy.

$V_{h,K}$ local test-space for the space-time (macro) element $\mathcal{I}_n \times K$.

List of Figures

List of Tables

Danksagung

Meine Zeit als Doktorand an der Graduate School of Computational Engineering (GSC CE) und am Institut Theorie Elektromagnetischer Felder (TEMF) hat mir viel Freude bereitet.
Herzlich danken möchte ich:

- Prof. Dr.-Ing. Thomas Weiland für die Annahme als Doktorand und die sehr guten Arbeitsbedingungen.
- Dr.-Ing. Sascha Schnepp für die herausragende fachliche Betreuung, sein außerordentlich hohes Engament sowie die sprachlichen und inhaltlichen Korrekturen an dieser Arbeit.
- Prof. Dr. techn. Herbert Egger für das große Interesse an meiner Arbeit und die damit verbundenen Diskussionen sowie die freundliche Übernnahme des Korreferats.
- Meinen Kollegen an der GSC CE sowie am TEMF für die sehr gute interdisziplinäre Zusammenarbeit[1].
- Carina Schuster, Christian Schmitt und Markus Lazanowski für die Unterstützung in organisatorischen Fragen sowie die Bereitstellung einer exzellenten Arbeitsumgebung an der GSC CE.
- Meiner Familie für ihre Unterstützung und den Rückhalt.
- Meiner geliebten Frau Nathalie für ihre Geduld, ihren Humor und die uneingeschränkte Unterstützung in allen Bereichen des täglichen Lebens!

Nicht zuletzt danke ich der DFG für die finanzielle Unterstützung (GSC 233/2, WE 1239/27-2.).

---

[1] Viel wichtiger ist jedoch, dass wir eine tolle Zeit mit vielen kurzweiligen ausseruniversitären Unternehmungen hatten und viele von euch gute Freunde geworden sind!

Wissenschaftlicher Werdegang

12.2010 – 3.2015	Doktorand Graduate School of Excellence Computational Engineering Technische Universität Darmstadt
12.2010 – 5.2014	Wissenschaftlicher Mitarbeiter Institut Theorie Elektromagnetischer Felder (TEMF) Technische Universität Darmstadt
2.2010 – 11.2010	Stipendiat Graduate School of Excellence Computational Engineering Technische Universität Darmstadt
8.2009 – 12.2009	Auslandssemester UBC Vancouver, Kanada
2008 – 2010	Studium Computational Engineering, Master Vertiefung Strömung und Verbrennung Technische Universität Darmstadt
2004 – 2007	Studium Computational Engineering, Bachelor Vertiefung Angewandte Mathematik und Mechanik Technische Universität Darmstadt
2003 – 2004	Studium Maschinenbau Technische Universität Darmstadt
2002	Abitur Bachgauschule, Babenhausen, Deutschland